UNDERSTANDING THE SCALE INTERACTION OF ATMOSPHERIC TRANSIENT DISTURBANCES AND ITS COUPLING WITH THE HYDROLOGICAL CYCLE OVER THE PACIFIC-NORTH AMERICAN REGIONS

A Dissertation
Presented to
The Academic Faculty

by

Tianyu Jiang

In Partial Fulfillment
of the Requirements for the Degree
Doctor of Philosophy in the
School of Earth and Atmospheric Sciences

Georgia Institute of Technology
August 2013

UNDERSTANDING THE SCALE INTERACTION OF ATMOSPHERIC TRANSIENT DISTURBANCES AND ITS COUPLING WITH THE HYDROLOGICAL CYCLE OVER THE PACIFIC-NORTH AMERICAN REGIONS

Approved by:

Dr. Yi Deng, Advisor
School of Earth and Atmospheric
Sciences
Georgia Institute of Technology

Dr. Robert Black
School of Earth and Atmospheric
Sciences
Georgia Institute of Technology

Dr. Jingfeng Wang
School of Civil and Environmental
Engineering
Georgia Institute of Technology

Dr. Josef Dufek
School of Earth and Atmospheric
Sciences
Georgia Institute of Technology

Dr. Katherine Evans
Climate Change Science Institute
Oak Ridge National Laboratory

Date Approved: June 10,   2013

To my parents,

for their love and support

ACKNOWLEDGEMENTS

Foremost, I would like to express my sincere gratitude to my advisor, Prof. Yi Deng, for his continual support, motivation, and collegiality throughout my Ph.D. studies. His passion for research and his guidance are admirable traits that were instrumental to the completion of this dissertation.

I would also like to thank the other members of my thesis committee, Prof. Robert Black, Prof. Josef Dufek, and Prof. Jingfeng Wang, for their valuable scientific advice during my time at Georgia Tech. My heartfelt appreciation also goes to Dr. Katherine Evans for her leadership and collaboration during my summer internship at Oak Ridge National Laboratory. I'd also like to thank my collaborators, Dr. Xiquan Dong, Dr. Wenhong Li, Dr. Yuhang Wang, and Ja-Ho Koo.

I am appreciative of my fellow research group members: Dr. Tae-Won Park, Dr. Yun-Young Lee, Brad Hegyi, Rebecca Westby, John Trostel and Jia He; and former group members: David Gray, Kelli Hornberger, Tina Colbert, Xin Chen and Dr. Renjun Zhou for their helpful scientific discussions.. Likewise, I would like to thank Dr. James Hack, Dr. Salil Mahajan, and Benjamin Mayer at ORNL for their respective scientific expertise.

I am indebted to Dr. Hao Luo for his warmhearted assistance as I transitioned to graduate school in the United States. Lastly, I am extremely grateful to Eric Parker and other friends in Atlanta for their meaningful companionship and the time we have shared.

TABLE OF CONTENTS

LIST OF TABLES

LIST OF FIGURES

SUMMARY

Large-scale atmospheric disturbances play important roles in determining the general circulation of the atmosphere during the North Pacific boreal winter. A number of scientific questions have been raised due to these disturbances' spatial and temporal complexity as well as the hydrological implication associated with them. In this dissertation, the principal goal is to further improve our understanding of the atmospheric high frequency (HF) and intermediate frequency (IF) disturbances active over the North Pacific. The study focuses on their energetics, intraseasonal and interannual variability, and the resulting hydrological impact over the eastern North Pacific and Western U.S. including extreme events.

To delineate the characteristics of HF and IF disturbances in the troposphere, we first derive a new set of equations governing the local eddy kinetic energy (EKE), and assess the critical processes maintaining local budgets of the HF and IF EKE. The diagnosis assesses the 3-D patterns of energy flux convergence (EFC), barotropic conversion (BT), baroclinic conversion (BC), and cross-frequency eddy-eddy interaction (CFEI). The local EKE budget analysis is followed by an investigation of the modulation of HF and IF eddy activity by different modes of low frequency climate variability. On interannual timescales, the response of various local energetic processes to El Niño-Southern Oscillation (ENSO) determines the HF and IF EKE anomalies and the

role of CFEI process is important in producing these anomalies. Also on interannual timescales, winter precipitation deficits associated with suppressed cyclonic activity, i.e., negative HF EKE anomalies, are linked to severe droughts over the U.S. Southern Great Plain (SGP) region. The suppressed cyclonic activity is, in turn, tied to phase changes in the West Pacific (WP) teleconnection pattern.

On intraseasonal timescales, variations in HF disturbances (a.k.a. storm tracks) over the North Pacific are closely coupled with tropical convection anomalies induced by the Madden-Julian Oscillation (MJO), and partly drive larger scale intraseasonal flow anomalies in this region through eddy-eddy interactions. Anomalous HF eddy activity induces subseasonal transitions between "wet" and "dry" regimes over the west coast of North America. Also on intraseasonal timescales, the East Asian cold surge (EACS) is found to provide a remote forcing of the winter precipitation anomalies in the western U.S. This modulation is achieved through "atmospheric rivers" (ARs), which are narrow channels of concentrated moisture transport in the atmosphere and are responsible for over 70% of the extreme precipitation events in the western U.S.. EACS effectively modulates the IF disturbance activity over the North Pacific, and the anomalous IF disturbances lead to the formation of an AR over the eastern North Pacific that ultimately induces precipitation anomalies in the western U.S. Analyses of the simulations from the NCAR Community Climate System Model version 4 (CCSM4) demonstrate that the connections among the EACS, AR and western U.S. precipitation are better captured by a

model with higher spatial resolutions. The improved simulation of these connections is achieved mainly through a better representation of the IF disturbances, and the associated scale-interaction processes in the higher resolution model.

CHAPTER 1

INTRODUCTION

1.1. Atmospheric Disturbances

Atmospheric disturbances are periodic fluctuations resulting from the action of restoring forces on air parcels that have been displaced from their equilibrium positions [*Holton*, 2004]. The mechanism for the restoring force may be compressibility, gravity, rotation or electromagnetic effects. Different from the meanders of air flow in the atmosphere, atmospheric disturbances can transport momentum and energy without the material transport of air parcels. Therefore, atmospheric disturbances and associated motions comprise a vital portion of atmospheric circulation and dynamics. The most common and simplest atmospheric disturbance is the acoustic wave, which is a longitudinal wave type with a temporal scale of several minutes. However, for meteorological interest, transverse disturbances such as internal gravity (buoyancy) waves, inertia waves, and Rossby waves are more critical.

Different climate and weather phenomena occupy different characteristic scales; in other words, atmospheric disturbances in different temporal scales correspond to different meteorological processes, on which the footstone of various frequency decomposition analysis is set. In a marvelous work by *Blackmon et al.* [1984a], atmospheric disturbances on 500 hPa are partitioned and grouped into high frequency (HF, 2.5 - 6 day period),

intermediate frequency (IF, 10-30 day period) and low frequency (LF, 30 days and above). It is shown that distinctions among the structures of HF, IF and LF disturbances as well as their time variation are dynamically important [*Blackmon et al.*, 1984b].

1.1.1. Atmospheric High Frequency Disturbances

High frequency components of atmospheric disturbances are typically referred to timescales shorter than 10 days (synoptic-scale), and they have been long appreciated because of their synoptic and physical importance [e.g. developing baroclinic disturbances, *Hartmann*, 1974; *Pratt and Wallace*, 1976] to human being. For example, by applying an "11-day running mean" filter to 500 hPa height from 1961 to 1963, *Sawyer* [1970] found the HF variability maximum over the North Atlantic is all along a belt of high cyclonic activity in the same domain. In an early work by *Blackmon et al.* [1977], the term "storm tracks" is used to refer to regions of large HF variance.

In the northern hemisphere winter, two major storm tracks are always found on HF variance maps — that is North Pacific storm tracks and North Atlantic storm tracks. These two storm tracks have been extensively studied in the past four decades in order to investigate the physical processes that bring about and maintain storm tracks, as well as the variability of storm tracks in multiple time scales. In subseasonal timescales, the two major storm tracks exhibit distinctly different features. While the intensity of the Atlantic storm track normally peaks in mid-winter (January-February), Pacific storm track activity

is at a relative low level, although the seasonal cycle of the local baroclinicity and jet stream are strongest in both domains [e.g., *Chang*, 2003; *Nakamura*, 1992]. Considerable efforts have been made to explain the cause of the so-called "mid-winter suppression" of the Pacific storm tracks. These explanations include, for example, the effects of diabatic heating [*Chang*, 2001; *Chang and Song*, 2006; *Chang and Zurita-Gotor*, 2007], reduced linear growth in the narrower jet stream [*Harnik and Chang*, 2004], barotropic shear acting to suppress eddy growth during mid-winter [*Deng and Mak*, 2005], wave trapping by the strong subtropical jet [*Nakamura and Sampe*, 2002], fast advection through the strong baroclinic zone because of the strong jet [*Nakamura*, 1992], suppressed upstream seeding [*S Penny et al.*, 2010; 2011] and suppressed upstream Rossby wave behavior [*Robinson and Black*, 2006]. However, there is not any single mechanism which can overwhelm the others, suggesting that the "mid-winter suppression" is led by a combined effect of several mechanisms. On interannual timescales, the El Niño-Southern Oscillation (ENSO) largely modulates the shifts in storm track structure in response to changes in the subtropical jet associated with anomalous tropical heating [*Straus and Shukla*, 1997; *Trenberth and Hurrell*, 1994]. The interdecadal variation of the Pacific storm track is modulated by the Pacific Decadal Oscillation (PDO), and inversely linked to the strength of the East Asian winter monsoon [*Chang and Fu*, 2002; *Nakamura et al.*, 2002]. As a result of this variability, the "mid-winter suppression" changed from being very pronounced in the early to mid-1980s to almost nonexistent in the following decade

[*Nakamura et al.*, 2002].

The interaction between synoptic eddies and a corresponding "mean" flow (or in a more generalized term, "cross-frequency coupling") often proves to be critical in producing and maintaining the mean flow and storm track anomalies. Through composite and Empirical Orthogonal Function (EOF) analysis, *Lau* [1988] showed that variations in the winter monthly storm track field are closely coupled to prominent atmospheric low frequency modes [a.k.a. teleconnections, *Wallace and Gutzler*, 1981]. For example, changes in the intensity of the Pacific storm track are often accompanied by a dipole structure in the upper tropospheric geopotential height over the western Pacific, resembling the Western Pacific (WP) pattern [e.g., *Wallace and Gutzler*, 1981], while the meridional displacement of the storm track seems to be associated with the Pacific/North American (PNA) pattern. With a dissipative atmospheric model driven by a zonally symmetric forcing, *Cai and Mak* [1990a] demonstrated that there exists a symbiotic relationship between the synoptic-scale and the low frequency, planetary-scale waves. The synoptic waves supply part of the energy they extract from the instantaneous zonal flow to the planetary waves through upscale energy cascade process, while the planetary waves create regions with strong baroclinicity where synoptic waves preferentially intensify.

Because North Pacific is neighbored by the largest tropical warmpool and also the Inter-Tropical Convergence Zone (ITCZ), make it inevitable to the influence of tropical fluctuations. Interannual oscillation of tropical sea surface temperature (SST) as a source

of extratropical variability has been extensively studied due to the prominence of the ENSO signal [e.g., *Horel and Wallace*, 1981; *Mo and Livezey*, 1986; *Straus and Shukla*, 2002]. The synoptic eddy forcing, in particular, the transient vorticity forcing associated with the storm track anomalies plays an essential role in setting up the extratropical response to ENSO, since the direct stationary wave response to ENSO in the extratropics is relatively weak [*Held et al.*, 1989; *Hoerling and Ting*, 1994]. It is important to note that synoptic-scale transients (eddies) coming out of a storm track are non-stationary and their equatorward propagations are not strictly constrained by the presence of an easterly "barrier" or a westerly "duct" [*Yang and Hoskins*, 1996]. In addition, given the observed storm track variability across multiple timescales and the interaction between synoptic eddies and a large number of extratropical LF modes, understanding the coupling between storm tracks and tropical intraseasonal oscillation becomes crucial.

1.1.2. Atmospheric Intermediate Frequency Disturbances

Atmospheric waves with timescales of 10 - 30 days are termed intermediate frequency disturbances. The nomenclature of this timescale indicates the fact that it lies in the between high and low frequency disturbances [*Blackmon et al.*, 1984a]. Although the filtering algorithms and cut off frequency differ among the studies, the results appear robust. Going back to 1950s, investigations have demonstrated that periods ranging from 15 to 30 days make a significant contribution to the overall variance [*Craddock*, 1957;

Landsberg et al., 1959]. *Blackmon et al.* [1984b] documented IF disturbances as mobile, zonally oriented wavetrains within well-defined waveguides originating in the jet entrance regions. By making use of empirical orthogonal functions, *Branstator* [1987] reported that the downstream dispersion over the North Pacific is often associated with westward-traveling patterns with a characteristic period on the order of about 3 to 4 weeks in the 500 hPa height field. In another independent study, *Kushnir* [1987] examined the retrograding (westward-moving) disturbances with a typical life cycle of about 3 weeks, and suggested that both baroclinic and barotropic conversions contribute to the growth of the disturbance energy. Based on results from both NCEP-NCAR National Centers for Environmental Prediction–National Center for Atmospheric Research (NCEP–NCAR) reanalysis and model simulation, *Lau and Nath* [1999] suggest these retrograding, 20~40 days disturbances in the Pacific sector can be explained on the basis of Rossby wave dynamics.

Compared with LF disturbances, IF disturbances are not geographically fixed, and the planetary scale teleconnection patterns are only evident in the LF field as reported by *Blackmon et al.* [1984a]. *Schubert* [1986] analyzed the leading hemispheric EOFs of the time-filtered 500-hPa streamfunction, and found the familiar hemispheric teleconnection patterns are clearly apparent only in the low frequency (45 day and above) band; there are hints of these patterns on shorter time scales, but the spatial patterns of the leading EOFs appear to lose their hemispheric-scale integrity quickly as the dominant timescale

becomes shorter. In a related study *Kushnir and Wallace* [1989] reported that well-defined hemispheric teleconnection patterns emerge as leading rotated EOFs of the interannual variability but not in the frequency bands corresponding to the intraseasonal variability.

A good example of the IF disturbances is the "blocking" or "persistent anomalies" [*Black*, 1997; *Dole and Gordon*, 1983; *Dole and Black*, 1990; *Trenberth*, 1986]. In the early study of blocking, investigators noted that during the life cycle of blocking events, the high-pressure disturbances that form over these regions tend to have retrograding movement over the $50^o - 70^oN$ latitude belt, with duration over a period of up to a month [e.g., *Berggren et al.*, 1949; *Namias and Clapp*, 1949]. *Sawyer* [1970] found that variance of 20-60 day timescales exhibited maxima in regions characterized by frequent blocking activity. *Mak* [1991] diagnosed an individual "blocking" event, and found the synoptic eddy-straining mechanism is particularly large in this case. *Holton* [2004] also pointed out that the forcing of large-scale anomalies by potential vorticity fluxes of high-frequency transient waves as well as internal nonlinear atmospheric dynamics can be important in the maintenance of "blocking" patterns. In another cross frequency analysis, *Matthews and Kiladis* [1999] discussed the mutual feedback between extratropical high frequency transients (6-25 days) and tropical intraseasonal oscillation. However, it must be pointed out that the high frequency transients defined in the study were to eliminate a large portion of disturbances which traditionally included in the

synoptic-scale band (shorter than 6 days) as well as the intraseasonal band, but keep most of the IF disturbances. Therefore, this work actually discussed the cross frequency interaction between the IF and LF disturbances.

1.1.3. *Energetics of Atmospheric Disturbances*

Atmospheric energetic is an important aspect of the atmospheric general circulation. As a fundamental physical property of the atmosphere, the form and transfer of the atmosphere internal energy has long been appreciated. One of the pioneer works is given by *Lorenz* [1955], when he proposed the concept of available potential energy (APE); in this work, Lorenz also developed a set of kinetic energies (KE) and APE by separating the eddy from the zonal mean, based on these, he described and quantified the energy flow between zonal mean state and departure eddies as well as APE and KE into a highly summarized diagram, which is known as Lorenz energy cycle. Within this energy cycle, we want to highlight the following facts: 1) APE is about ten times the total KE, but less than 1% of the total PE. 2) Increases in APE are usually accompanied by increases in KE and therefore involve diabatic effects. 3) Zonal mean APE converts to eddy APE and to EKE, and to zonal EKE.

Inspired by this work, extensively studies were conducted to examine the energetic role in the atmosphere [*Oort*, 1964; *Plumb*, 1983; *Wiin-Nielsen*, 1962]. Specifically, to make the energetic analysis more applicable to difference meteorological disturbances,

Saltsman [1957] decomposed the KE and APE into a spectrum of spatial scales by Fourier analyses along latitude circles. By use of the cross-spectral technique, *Hayashi* [1980] derived the spectral formula and computed the nonlinear energy transfer spectra. Using three-dimensional normal mode expansions, *Tanaka et al.* [1986] analyzed the energetics characteristics of the observed and simulated general circulation. The above works, although reveal the general energy cycle from a global view, did not give a spatial structure due to various limitations at that time.

Sheng and Hayashi [1990a; b] combined the wavenumber-frequency spectra analysis with the temporal frequency spectra analysis and examined the energy cycle with observation as well as the GCM data. *Sheng and Derome* [1991], by utilizing the same approach, depicted the energy transfer between transient eddies and mean flow. In these studies, they delineated the energy cycle, as well as the spatial structure of eddy-mean flow interaction, but due to the method and equation they used, the meanings of different terms are not quite intuitive.

It is possible to further break down the energetic analysis in terms of temporal scales, while keep the local features as well, which is so called local energetic analysis. In this case, the energy conversion or the energy flow terms become extremely difficult to handle, because the conversion terms can have different local expressions or forms, make the explanation much more complicated and ambiguous.

Despite of the doubts and criticism [e.g., *Plumb*, 1983] as well as the competition

from other diagnostic tools (e.g. 3D wave activity flux), the local energetic analysis is still widely used and developed by the community because it is free from the quasi-geostrphic (QG) framework. For example, *Mak and Cai* [1989] analyze the modal and nonmodal instability of a barotropical jet streak, they applied the local energetics analysis to compare the energy generation rate in different types of instability. Study of the dynamics of regional cyclogenesis in a two-layer channel model [*Cai and Mak*, 1990b] suggests the major processes in the local energetic budget are comparable and greatly counteract one another, the net result is a downstream development of the perturbation energy. Local energetic analysis is also employed to interpret the life cycle of southern hemisphere cyclone wave [*Orlanski and Katzfey*, 1991], which reveals the significant role of energy flux divergence in the system evolution. More recently, by means of a revised synoptic energy budget, *Hsu et al.* [2010] examines the interaction between tropical Intraseasonal Oscillation and the EKE over western Pacific, they reports that the synoptic-scale EKE gain energy through barotropic energy conversion when the ISO in its active phase and vice versa.

1.2. North Pacific Hydro-Climate Variability

1.2.1. Water Cycle and Precipitation

The water, or hydrological, cycle in the Earth system is the endless movement of

water among the atmosphere, continents and oceans. Movement of water can occur in any of the three phases, for example, the movement of water between the land surface and the atmosphere occurs in the vapor phase (evaporation and condensation), liquid phase (rain), and solid phase (snowfall). One of the fundamental concepts of the water cycle is residence time, which is a measure of the average amount of time that a molecular of water spends in a particular system. Water in the ice sheets has a residence time of more than 6000 years, and of about 3000 years for oceans, while in the atmosphere it has a residence time of approximately 8 days.

The atmosphere is often considered as the starting point of the water cycle. Driven by solar energy and gravity, the dominant hydrological process involving atmospheric water is precipitation over the land surface. Most of the precipitation falling over a continent, including North America, originates from the bordering oceans, and from there the precipitated water is transported significant distances across the continent.

Precipitation has significant natural and social impacts over the western North American continent, from the Bering Sea coast of Alaska, the Pacific Northwest to the southwestern U.S.. For example, winter precipitation over Alaska not only brings a significant amount of water, but also alters the local temperature, which plays a principal role in the flow of most of Alaska's rivers and the permafrost thaw [e.g., *Jorgenson et al.*, 2001]. The Pacific Northwest and California are particularly vulnerable to winter storms due to the substantial coastal terrain as well as its unique vegetation [*Mass and Dotson*,

2010]. Moreover, the precipitation over the Sierra Nevada and Rocky Mountains in the form of snowfall determines the snowpack in these regions; the accumulation occurring during the winter months becomes all-important during spring runoff, which provides much of the streamflow, ground water recharge, and soil moisture for western North America [*Guan et al.*, 2011; *Serreze et al.*, 1999].

1.2.2. *Variability and Modulation of Eastern Pacific Precipitation*

Because of its significant ecological influence and socioeconomic impact, understanding the hydrological cycle, especially precipitation, over the Eastern Pacific and western North America becomes a pressing task. A large portion of winter precipitation in western North America is associated with North Pacific extratropical cyclones [*Myoung and Deng*, 2009]. Extratropical cyclones are the primary organization of HF disturbances generated in midlatitudes. These synoptic scale migrating systems tend to occlude and dissipate over the coast of western North America, and the entrainment of the water vapor in these systems can trigger heavy precipitation once it approaches the land. For example, *Raphael and Mills* [1996] reported that the total precipitation received at ten California stations in two El Niño winters was drastically different because of different effects of local circulation anomalies on cyclone tracks. *Raphael and Cheung* [1998] further pointed out that the diminished extent of cyclonic activity over the East Pacific is responsible for the dryness of the second half of the 1980s

12

in California. Even though the length of the period considered in these two studies is rather short, their results suggest that the variability of coastal cyclones largely determines the variability of the winter precipitation in the western United States on interannual time scales. Such influences are also expected to be modulated by tropical signals such as ENSO.

In a series of landmark studies by *Bjerknes* [1966; 1969; 1972], the link between sea surface temperature anomaly and the variability of convection in the central equatorial Pacific is established; meanwhile, Bjerknes relates extratropical circulation anomalies over the North Pacific to changes in the regional Hadley circulation. Inspired by the seminal concept of the teleconnection mechanism proposed by *Wallace and Gutzler* [1981], *Higgins and Mo* [1997], *Mo and Higgins* [1998], *Mo* [1999] and *Higgins et al.* [2000] demonstrated that tropical convection plays a vital role in setting up persistent North Pacific circulation anomalies, affecting the strength of moisture transport, inducing upper level divergence/convergence over California, and thus driving the transition between "dry" and "wet" episodes and the occurrence of extreme rainfall events over the U.S. west coast. In particular, *Mo and Higgins* [1998] pointed out that enhanced tropical convection over the western Pacific (near 150 °E) tends to create wet (dry) conditions over the Pacific Northwest and dry (wet) conditions over the Southwest. *Jones* [2000] and *Jones et al.* [2004] further showed that extreme precipitation events on both regional (California) and global scale tend to occur more frequently in active phases than in

quiescent phases of the Madden-Julian Oscillation [MJO, *Madden and Julian*, 1972; 1994].

1.2.3. Atmospheric River

Besides extratropical cyclones, atmospheric river (AR) is another important weather phenomenon, which tends to trigger high impact precipitation over western North American coastal area. ARs are long, narrow water vapor corridors within a broad region of generally poleward transport of heat and moisture. These filamentary bands occupy less than 10% of the Earth's circumference at mid-latitudes at any given time, but are responsible for more than 90% of the water vapor transport from tropics to extratropics [*Zhu and Newell*, 1998]. Due to the intense water vapor it transports, AR can produce significant amounts of precipitation within a short period once they reach the west coast of midlatitude continents and lead to severe flooding and landslides [e.g., *Guan et al.*, 2010; *Ralph and Dettinger*, 2011; *F M Ralph and M D Dettinger*, 2011]. However, AR and their extreme precipitation also provide essential water for supply and reservoirs in various forms seasonally, and thus maintain the water balance in western regions through their cumulative effect [*Dettinger et al.*, 2011].

Over the past decade, field experiments and other studies have documented physical characteristics that contribute to AR development and landfall and they span from the planetary scale to the mesoscale. Also, most have focused on events over eastern Pacific

and western North America. For example, by using observational data from one winter airborne and satellite, *Ralph et al.* [2004] reported that the characteristic dimensions of AR are thousands of kilometers long, but only 400 km wide on average, and that the integrated water vapor (IWV) in AR regions are generally greater than 20 mm and associated with a pre-frontal low-level jet. In other studies of AR and associated extreme precipitation, it is found that AR events occur primarily within the warm sector of the extratropical cyclones [*Neiman et al.*, 2008a; *Ralph et al.*, 2004; *Ralph et al.*, 2005; *Ralph et al.*, 2006]. However, they can also develop in the absence of extratropical cyclones, in which case they are fueled by tropical moisture directly [*Bao et al.*, 2006]. On the other hand, *Neiman et al.* [2008b] found that when AR make landfall in winter over the eastern North Pacific, there is a trough-like structure which sits over the Intermountain West on 500hPa height field. In another case study of a Pacific AR event during March 2005, *Ralph et al.* [2010] reported that several major planetary scale phenomena including Madden-Julian Oscillation, extratropical wave packets, and Kelvin waves all could potentially influence the AR event. Based on high resolution reanalysis data, *Jiang and Deng* [2011] constructed the first AR probability climatology map and showed that AR and associated precipitation can be modulated by IF disturbance over the eastern North Pacific following the East Asian Cold Surges (EACS) in winter. However, this work does not provide the detail nor dynamical mechanisms behind this downstream modulation.

1.3. Summary of Research Objectives

As a testament to the complexity of atmospheric disturbances over the North Pacific Ocean and adjacent continents, the following dissertation covers a variety of research problems. These topics range from eddy kinetic energy, to the local energetics of HF and IF eddies, to activities of extratropical cyclones and atmospheric rivers, with the intent to understand their variability, cross-frequency interaction and modulation as well as the implications with regards to the water cycle and extreme events over the western North American continent. The list below summarizes the research goals for the work that follows.

- Derive and quantify the local energetic budgets for HF and IF eddies including the cross-frequency interaction processes. What is the role of cross-frequency terms in determining the HF and IF EKE? How do the energetic processes of IF eddies are distributed in the troposphere? (Chapter 2).

- Utilize the local energetic budgets as well as a feature tracking algorithm to investigate the modulation of HF and IF eddies by tropical interannual and intraseasonal timescales forcing as well as the teleconnection modes (e.g., PNA and WP) over the North Pacific. Does tropical intraseasonal oscillation modulate precipitation over the west coast of North America? How do the teleconnection modes project onto the drought over the U.S. Southern Great

Plain during winter 2005/2006 with regard to the alteration of the synoptic-scale cyclones? (Chapter 3)

- Develop algorithms for atmospheric river detection, and quantitatively analyze atmospheric river activity. To what extent is extreme precipitation over the west coast of the U.S. related to atmospheric river events? (Chapter 3)

- Study the relationship between high-impact precipitation over western North America and another upstream weather extreme (e.g., East Asia cold air outbreak). How do atmospheric rivers bridge the weather extremes? Do HF disturbances still play a dominant role in atmospheric river events? (Chapter 4)

- Consider the filamentary structure of atmospheric rivers and the dynamical mechanism with which it is associated. Can climate models accurately capture the extreme weather phenomenon and upstream modulation? Does model resolution matter? (Chapter 4)

CHAPTER 2

LOCAL ENERGETICS FOR HF AND IF EDDIES

2.1 Derivation of EKE Budgets

We derive the EKE equation starting with the horizontal momentum equation of transient eddies in pressure coordinates [e.g., *Chang and Orlanski*, 1993; *Orlanski and Katzfey*, 1991]:

$$\frac{\partial \vec{V}_T}{\partial t} = -\vec{V}_{3M} \times \nabla_3 \vec{V}_T - \vec{V}_{3T} \times \nabla_3 \vec{V}_M - \vec{V}_{3T} \times \nabla_3 \vec{V}_T - \overline{\vec{V}_{3T} \times \nabla_3 \vec{V}_T} - \nabla \Phi_T - f\vec{k} \times \vec{V}_T + \vec{F}_{rT}$$

(1)

where $\vec{V}$ and $\vec{V}_3$ stand for horizontal and three-dimensional wind vector, respectively; Φ is geopotential; f is Coriolis parameter, and $\vec{F}_r$ is the viscous force. Subscripts "*T*", and "*M*" in (1) represent the transient eddy and time-mean component of the flow, respectively. The overbar here stands for time mean. The transient eddy component here, obtained as departure from the seasonal mean in the calculation, is further broken down into 3 frequency bands: HF (2-6 days), IF (7-29 days) and low frequency (LF, 30-90 days). Note that the definitions of the frequency bands adopted here are slightly different compared to those used in Deng and Jiang (2011) due to the use of a "sharper" bandpass filter. The results to be presented are not sensitive to the small changes in the definition of eddies. Applying an HF bandpass filter to (1), we obtain the momentum equation for HF eddies as follows,

$$\frac{\partial \vec{V}_H}{\partial t} = -\vec{V}_{3M} \times \nabla_3 \vec{V}_H - \vec{V}_{3H} \times \nabla_3 \vec{V}_M - \overline{\vec{V}_{3H} \times \nabla_3 \vec{V}_H}^H - \nabla \Phi_H - f\vec{k} \times \vec{V}_H + \vec{F}_{rH}$$

(2)

where subscript "*H*" indicates the HF component of the total eddy field and overbar with

superscript "*H*" denotes the HF bandpass filtering.

Taking the dot product of (2) with $\vec{V}_H$, utilizing hydrostatic balance and the continuity

equation in pressure coordinates, we obtain the following HF EKE equation,

$$\frac{\partial K_H}{\partial t} = -\nabla_3 \cdot (\vec{V}_M K_H + \Phi_H \vec{V}_{3H}) - \vec{V}_H \cdot (\vec{V}_{3H} \cdot \nabla_3 \vec{V}_M) - \omega_H \alpha_H - \vec{V}_H \cdot \overline{(\vec{V}_{3T} \cdot \nabla_3 \vec{V}_T)}^H + \vec{F}_{rH} \cdot \vec{V}_H$$

(3)

In (3), $K_H = \frac{1}{2}|\vec{V}_H|^2$ represents the HF EKE; ω and α stand for vertical velocity in

pressure coordinates and specific volume, respectively. The first term on the right hand

side (RHS) of (3) is the convergence of the 3D energy flux (EFC), which includes the

advection of HF EKE by the time-mean flow and the energy dispersion associated with

ageostrophic geopotential flux. Note that the EFC term reduces to the net flux at the upper

and lower boundaries when integrated over the entire atmosphere, and it mainly acts to

redistribute EKE in the space. The second term on the RHS of (3) represents the conversion

of kinetic energy from the time-mean flow to the HF eddies and is often referred to as

barotropic conversion (BT). The third term on the RHS measures the rate of conversion

from eddy potential energy (EPE) to EKE, also known as baroclinic conversion (BC). The

fourth term is the production of HF EKE via cross-frequency eddy-eddy interaction (CFEI).

The last term on the RHS of (3) is the mechanical dissipation of HF EKE. The CFEI term

can be further divided by separating the total flow of transient eddies into the HF, IF and LF

component, i.e.,

$$-\vec{V}_H \cdot \overline{(\vec{V}_{3T} \cdot \nabla_3 \vec{V}_T)}^H = -\vec{V}_H \cdot \overline{(\vec{V}_{3H} \cdot \nabla_3 \vec{V}_H)}^H - \vec{V}_H \cdot \overline{(\vec{V}_{3H} \cdot \nabla_3 \vec{V}_I + \vec{V}_{3I} \cdot \nabla_3 \vec{V}_H + \vec{V}_{3I} \cdot \nabla_3 \vec{V}_I)}^H$$
$$-\vec{V}_H \cdot \overline{(\vec{V}_{3H} \cdot \nabla_3 \vec{V}_L + \vec{V}_{3L} \cdot \nabla_3 \vec{V}_H + \vec{V}_{3L} \cdot \nabla_3 \vec{V}_L)}^H - \vec{V}_H \cdot \overline{(\vec{V}_{3I} \cdot \nabla_3 \vec{V}_L + \vec{V}_{3L} \cdot \nabla_3 \vec{V}_I)}^H \tag{4}$$

In (4), the CFEI term now consists of 4 parts: kinetic energy generation due to interaction among HF eddies (HH, first term on the RHS of (4)), interaction between HF and IF eddies (HI, second term on the RHS of (4)), interaction between HF and LF eddies (HL, third term on the RHS of (4)), and interactions among HF, IF and LF eddies (HIL, last term on the RHS of (4)). A full list of the abbreviations and definitions is shown in table 2.1. In a similar way, the IF EKE equation can be obtained, i.e.,

$$\frac{\partial K_I}{\partial t} = -\nabla_3 \cdot (\vec{V}_M K_I + \Phi_I \vec{V}_{3I}) - \vec{V}_I \cdot (\vec{V}_{3I} \cdot \nabla_3 \vec{V}_M) - \omega_I \alpha_I - \vec{V}_I \cdot \overline{(\vec{V}_{3T} \cdot \nabla_3 \vec{V}_T)}^I + \vec{F}_{rI} \cdot \vec{V}_I \tag{5}$$

Where

$$-\vec{V}_I \cdot \overline{(\vec{V}_{3T} \cdot \nabla_3 \vec{V}_T)}^I = -\vec{V}_I \cdot \overline{(\vec{V}_{3I} \cdot \nabla_3 \vec{V}_I)}^I - \vec{V}_I \cdot \overline{(\vec{V}_{3H} \cdot \nabla_3 \vec{V}_I + \vec{V}_{3I} \cdot \nabla_3 \vec{V}_H + \vec{V}_{3H} \cdot \nabla_3 \vec{V}_H)}^I$$
$$-\vec{V}_I \cdot \overline{(\vec{V}_{3I} \cdot \nabla_3 \vec{V}_L + \vec{V}_{3L} \cdot \nabla_3 \vec{V}_I + \vec{V}_{3L} \cdot \nabla_3 \vec{V}_L)}^I - \vec{V}_I \cdot \overline{(\vec{V}_{3H} \cdot \nabla_3 \vec{V}_L + \vec{V}_{3L} \cdot \nabla_3 \vec{V}_H)}^I \tag{6}$$

Table 2.2 presents a full list of the abbreviations and definitions used in discussing the IF EKE budget. Note that the CFEI terms presented here do not represent direct transfers of EKE among eddies residing in different frequency bands. For example, HI in the HF EKE equation quantifies the production of HF EKE due to the interaction between HF and IF eddies and it is not the direct opposite to the HI in the IF EKE equation which represents the generation of IF EKE due to the interaction between HF and IF eddies. The complete set of EKE equations including the so-called "cross-terms" are provided in the appendix of

this paper for the reader's reference.

Table 2. 1: Abbreviations and definitions of the HF EKE budget.

Abbreviations	HF EKE	EFC	BT	BC	CFEI
Formula	$\dfrac{1}{2}\left|\vec{V}_H\right|^2$	$-\nabla_3 \cdot (\vec{V}_M K_H + \Phi_H \vec{V}_{3H})$	$-\vec{V}_H \cdot (\vec{V}_{3H} \cdot \nabla_3 \vec{V}_M)$	$-\omega_H \alpha_H$	$-\vec{V}_H \cdot \overline{(\vec{V}_{3T} \cdot \nabla_3 \vec{V}_T)}^H$
Definition	HF eddy kinetic energy	Energy flux convergence	Barotropic conversion	Baroclinic conversion	cross-frequency eddy-eddy interaction

Table 2. 2: Abbreviations and definitions of the IF EKE budget.

Abbreviations	IF EKE	EFC	BT	BC	CFEI
Formula	$\dfrac{1}{2}\left|\vec{V}_I\right|^2$	$-\nabla_3 \cdot (\vec{V}_M K_I + \Phi_I \vec{V}_{3I})$	$-\vec{V}_I \cdot (\vec{V}_{3I} \cdot \nabla_3 \vec{V}_M)$	$-\omega_I \alpha_I$	$-\vec{V}_I \cdot \overline{(\vec{V}_{3T} \cdot \nabla_3 \vec{V}_T)}^I$
Definition	IF eddy kinetic energy	Energy flux convergence	Barotropic conversion	Baroclinic conversion	cross-frequency eddy-eddy interaction

2.2 Data and Methods

The budget analysis for HF and IF EKE is based upon Eqs. (3) - (6) and uses the NCEP-DOE Reanalysis for the period 1979 to 2011. This dataset consists of standard daily atmospheric fields such as horizontal and vertical wind, geopotential height and temperature on 17 pressure levels and a 2.5^o latitude 2.5^o longitude grid (Kanamitsu et al. 2002). Monthly sea surface temperature (SST) in the Nino 3.4 region is obtained from

the NOAA Climate Prediction Center (CPC, http://www.cpc.ncep.noaa.gov/data/indices/) to identify El Niño and La Niña events in the composite analysis. A Lanczos filter [*Duchon*, 1979] with 203 weights is used throughout the analysis to separate transient eddies into different frequency bands and to conduct corresponding bandpass filtering for the CFEI term. The choice of 203 weights guarantees the tradeoff between Gibbs effect and the sharpness of stop-band. Mass-weighted vertical averaging between 1000 mb and 200 mb is done for part of the results to highlight the horizontal distribution of EKE budget terms in the troposphere.

2.3 Results

2.3.1 Climatology of HF EKE budget

The winter (December-January-February, DJF) climatology of the HF EKE and the related energy conversion terms are shown in Figure 2.1. All quantities displayed are mass-weighted tropospheric averages. The two localized maxima in the HF EKE field (Fig. 3.1a) correspond to the two distinct storm tracks over the North Pacific and North Atlantic in boreal winter with the Atlantic storm track being more intense compared to the Pacific one [e.g., *Chang et al.*, 2002]. The EFC term in the HF EKE budget (Fig. 2.1b) is characterized by a west-east dipole over both basins. This spatial structure indicates that mean-flow advection and energy dispersion via ageostrophic geopotential flux effectively

redistribute EKE eastward and extend the storm tracks to the east ocean basins where local baroclinicity is relatively weak compared to the west ocean basins, a process known as "downstream development" [*Chang*, 1993; *Mak and Cai*, 1989]. The values of barotropic conversion (BT, Fig. 2.1c) are generally negative over the North Pacific and North Atlantic, and are positive over East Asia, North America and North Africa, consistent with previous findings that HF eddies gain (lose) kinetic energy from (to) the background flow as they propagate toward (away from) a localized jet and become more isotropic (anisotropic) in the confluent (diffluent) region of the jet entrance (exit) [e.g., *Cai et al.*, 2007; *Deng and Mak*, 2006; *Wallace and Lau*, 1985]. The close match between local maxima in baroclinic conversion (BC, Fig. 2.1d) and those in HF EKE field (Fig. 2.1a) clearly demonstrates that BC is the primary process generating HF EKE. Fig. 2.1f show the distribution of EKE production due to nonlinear interaction among eddies of different timescales, i.e., the CFEI term. The net effect of CFEI is to decrease HF EKE over the eastern North pacific and the entire North Atlantic. This is a clear demonstration that nonlinear, scale-interaction processes are more important over regions where synoptic waves attain large amplitudes. The main contributor to the CFEI term is the interaction between HF and IF eddies, i.e., HI, shown in Fig. 2.1e.
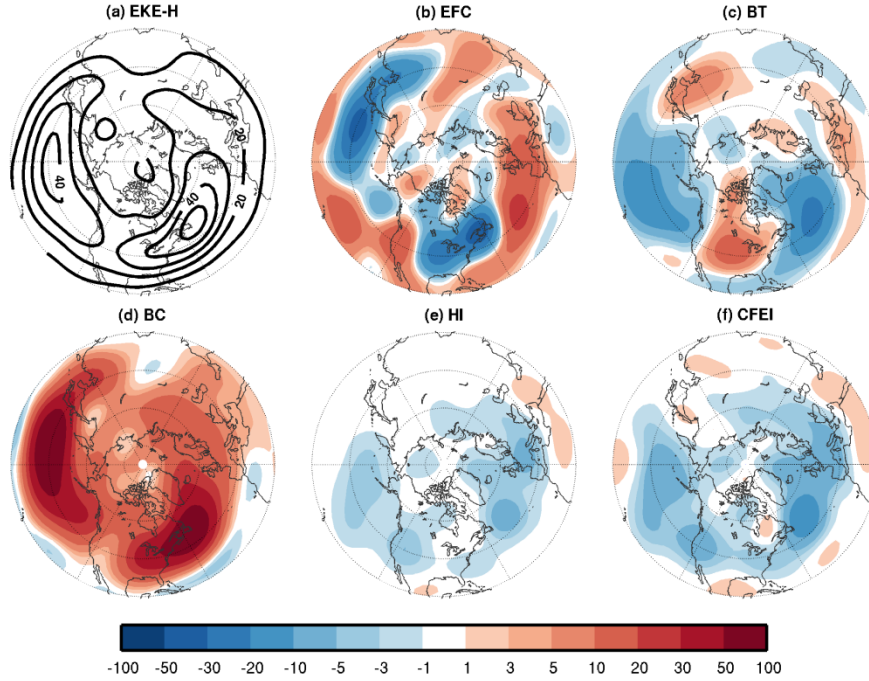
Figure 2.1: Winter climatology of the tropospheric-averaged EKE budget for HF eddies. (a) HF EKE (contour interval: $10m^2/s^2$); (b) EFC; (c) BT; (d) BC; (e) HI; (f) CFEI. Units in (b)-(f) are m^2s^{-2}/day. All data have been spectrally truncated to T15 before plotting. For detailed definitions of various budget terms, please refer to Table 2.1.

To delineate the vertical structure of the EKE budget, we present here also the zonal mean of the various conversion terms. Figure 2.2 shows the corresponding latitude-pressure cross-sections for the zonal mean quantities in the HF EKE budget. The maximum HF EKE (Fig. 2.2a, contours) is found in the upper troposphere around 300 mb with peak amplitude exceeding 30 J • m^{-3}. It is located on the northern flank of the tropospheric zonal-mean zonal jet (Fig. 2.2a, shading). In the sense of zonal mean, the primary role of EFC process (Fig. 2.2b) is to vertically redistribute HF EKE, which is mainly produced by BC (Fig. 2.2d) in the mid-lower troposphere (below 500mb). This redistribution process leads to the HF EKE maximum in the upper troposphere; meanwhile,

part of the EKE is dispersed to lower levels where mechanical dissipation in the boundary layer removes EKE. The damping of HF EKE by barotropic processes (BT) is strongest around 500mb and located primarily on the northern flank of the zonal jet (Fig. 2.2c). CFEI (Fig. 2.2f) is another major sink of HF EKE in the midlatitudes, and the largest negative conversion, due to interaction between HF and IF eddies, is found in the middle troposphere (~500 mb) directly beneath the center of maximum EKE. The vertical structure of HI is similar to that of BT indicating the same physical nature of the two conversion processes, i.e., both related to Reynolds stresses.
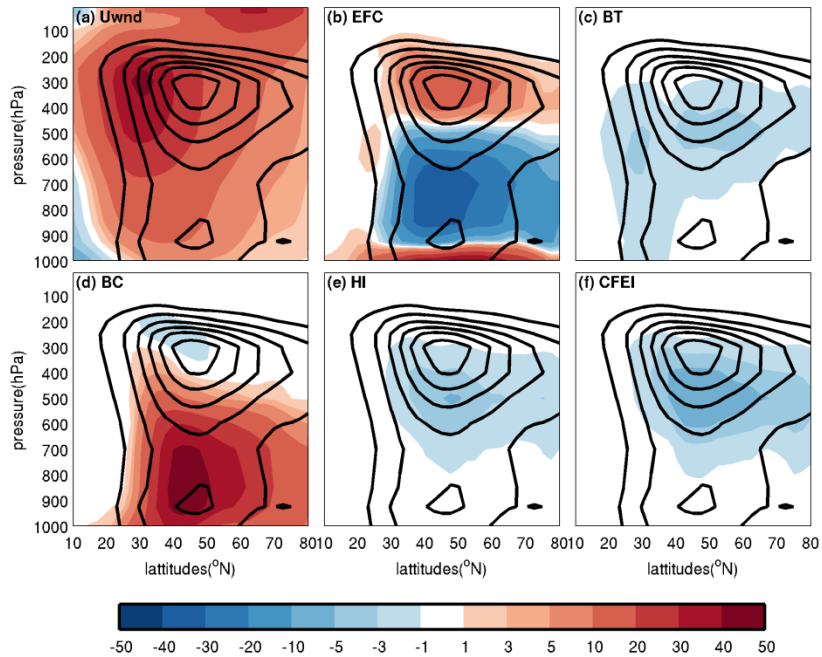
Figure 2.2: Latitude-pressure cross-sections of the climatological zonal-mean EKE budget terms for HF eddies. All terms have been mass-weighted by multiplying the air density. Contours are HF EKE (contour interval: 5 $J•m^{-3}$). Color shading in (a)-(i) correspond to (a) zonal wind; (b) EFC; (c) BT; (d) BC; (e) HI; (f) CFEI. Unit is ms^{-1} in (a) and $J•m^{-3}$/day in (b)-(f).

In addition to the zonal mean, we also examine longitude-pressure cross-sections of meridionally-averaged (over 30°N-60°N) quantities. Fig. 2.3 shows the corresponding budget terms for HF eddies. The zonal distribution of HF EKE clearly reveals two distinct storm tracks over the North Pacific and North Atlantic (Fig. 2.3a, contour). EFC (Fig. 2.3b) redistributes part of the HF EKE generated by BC (Fig. 2.3d) in the lower-mid troposphere to upper levels and is responsible for the formation of the upper tropospheric maximum in EKE. The two lower-tropospheric maxima in HF EKE are located over the west ocean basins adjacent to the east coasts of the Asian and North American continent, where near surface baroclinicity and BC tend to peak (Fig. 2.3d). In Fig. 2.4, EFC is further separated into energy convergence due to (horizontal and vertical) mean-flow advection and due to (horizontal and vertical) ageostrophic geopotential flux. It is clear that the convergence due to ageostrophic geopotential flux, particularly its vertical component (Fig. 2.4d), is the dominant process of EFC in the HF EKE budget. The horizontal components of the mean-flow advection (Fig. 2.4a) and EKE dispersion (Fig. 2.4b) reach their respective maximum values in the upper troposphere. As in the zonal mean case, BT (Fig. 2.3c) and CFEI (mainly HI, Figs. 2.3f and 2.3e) serve as two major sinks of HF EKE.
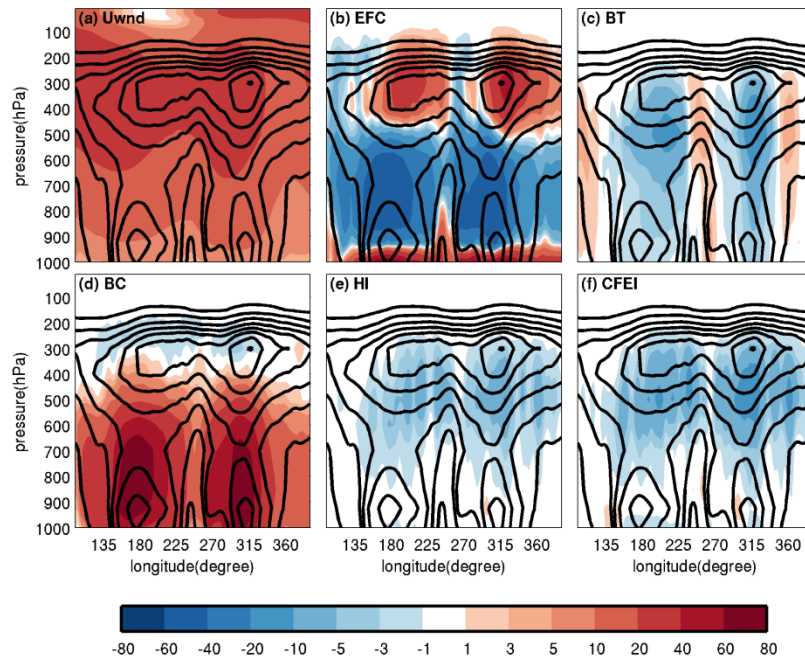
Figure 2.3: Longitude-pressure cross-sections of the climatological HF EKE budget terms meridionally averaged between 30 N and 60 N. All terms have been mass-weighted by multiplying the air density. Contours are HF EKE (contour interval: 5 J • m^{-3}). Color shading in (a)-(i) correspond to (a) zonal wind; (b) EFC; (c) BT; (d) BC; (e) HI; (f) CFEI. Unit is ms^{-1} in (a) and J • m^{-3}/day in (b)-(i).
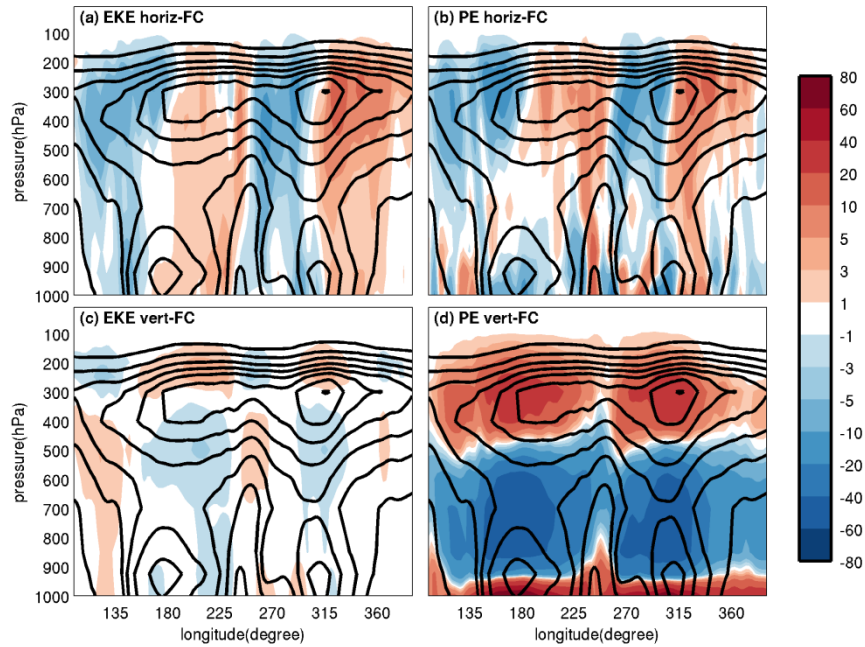
Figure 2.4: Longitude-pressure cross-sections of the HF EKE convergence due to advection of EKE by the winter-mean flow (a), horizontal ageostrophic geopotential flux (b), vertical advection of EKE by the winter-mean flow (c), and vertical ageostrophic geopotential flux (d). All terms have been mass-weighted by multiplying the air density. Contours are HF EKE (contour interval: 5 $J m^{-3}$). All quantities shown are meridional-averages between 30 N and 60 N. Unit is $J m^{-3}$/day

2.3.2   Climatology of IF EKE budget

Figure 3.5 shows the climatological budget terms for IF EKE. The maxima in IF EKE (Fig. 2.5a) are located downstream of the respective storm tracks as indicated by the maxima in HF EKE (Fig. 2.1a). The larger magnitude of IF EKE compared to HF EKE is consistent with the result of *Sheng and Hayashi* [1990a] that the peak transient eddy kinetic energy is found in the period ranging from 6.8 to 34 days, roughly corresponding to our definition of the IF band. The horizontal distribution of EFC (Fig. 2.5b) is characterized by

two dipoles. Over the North Pacific, EFC reduces IF EKE over the entire basin and increases EKE over western North America. Negative (positive) EFC values are also found over eastern North America (North Atlantic). Similar to that in the HF EKE budget, BT (Fig. 2.5c) shows three centers of positive conversion upstream of the winter time-mean jets (East Asia-Western Pacific, North America and North Africa) and three centers of negative conversion downstream of the jets (eastern North Pacific, North Atlantic and East Europe). BC (Fig. 2.5d) still contributes substantially to the production of IF EKE in the northern midlatitudes.
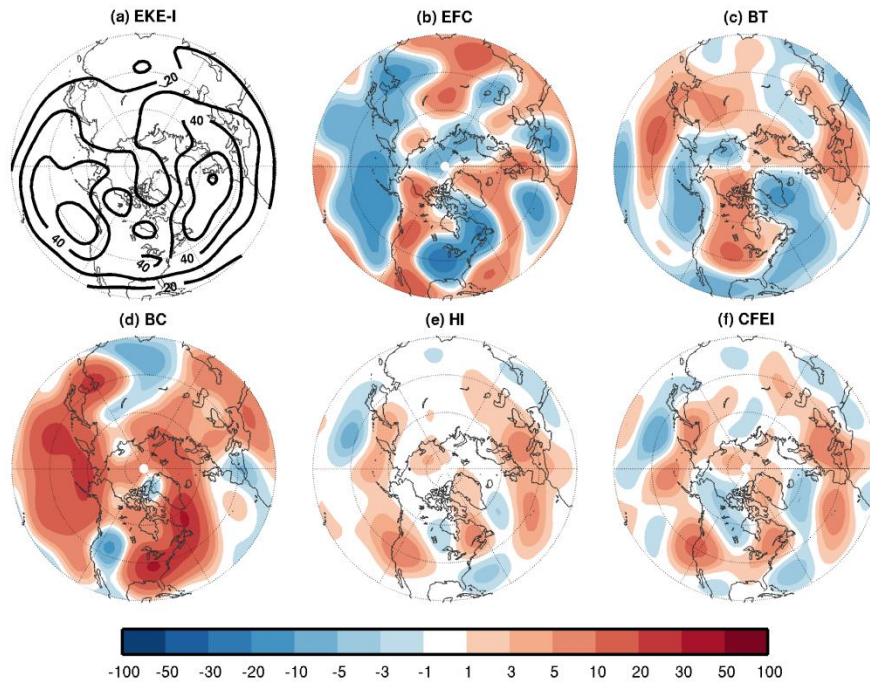
Figure 2.5: Same as Fig. 2.1, except for IF eddies; for detailed definitions, please refer to Table 2.2.

Over a large portion of the North Pacific, the effects of BC, EFC and BT cancel out.

This leaves CFEI (Fig. 2.5f) to stand out, especially over the eastern North Pacific and western North America, where HI (Fig. 2.5e) dominates the CFEI term and overlaps with the maximum of IF EKE. The significant contribution to IF EKE from the interaction between HF and IF eddies (i.e., the HI term) confirms the critical role of synoptic eddies in the development and maintenance of IF disturbances such as a blocking high or a cutoff low [e.g., *Cai and Van Den Dool*, 1994]. Note that the HI term does not quantify the direct kinetic energy transfer between HF and IF eddies. Over the eastern North Atlantic and West Europe, the northern portion of the IF EKE maximum is largely determined by the effect of EFC while the southern portion is collectively contributed by BT and CFEI (primarily HI). The positive BT contribution here supports the idea that some IF eddies might originate from barotropic instability of a zonally-varying background flow [for a review, please see *Dole*, 2008]. These results suggest that the characteristics of IF EKE budget are fundamentally different between the two ocean basins. Additionally, our analysis also suggests that the interaction among IF eddies themselves, i.e., the II term (not shown due to small values), has little contribution to the lifecycle of IF disturbance as discussed earlier by *Cash and Lee* [2000].

For the IF EKE, the maximum in its zonal mean is located to the north of and slightly above the jet core with peak amplitude exceeding 40 J $\cdot$ m^{-3} (Fig. 2.6a, contours). Similar to that in the HF EKE budget, the effect of BC is still concentrated below 500 mb (Fig. 2.6d). The effect of BC is largely balanced by the effect of EFC (Fig. 2.6b). In the

zonal-mean sense, the role of BT in the IF and HF EKE budget is distinctly different. BT represents an important sink of HF EKE (Fig. 2.6c), but only does so for IF EKE on the southern flank (equatorward side) of the zonal-mean jet. On the northern flank and near the level of maximum IF EKE, BT acts as a primary source of IF EKE. Given the strong cancelation between BC and EFC, the positive EKE productions due to BT and CFEI (dominated by HI, Figs. 2.6f and 2.6e) turn BT and HI into the two most important contributors to IF EKE when the zonal-mean budget is considered.
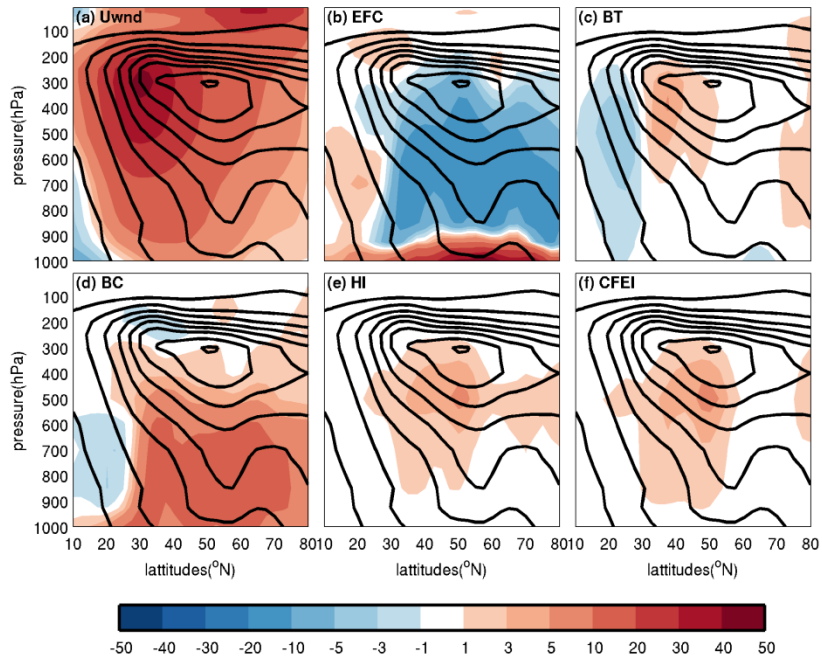
Figure 2.6: Same as Fig. 2.2 except for IF eddies.

The longitude-pressure cross-sections for IF EKE budget terms are shown in Figure 2.7. Consistent with the zonal mean quantifies, BT (Fig. 2.7c) acts as an important source of IF EKE directly contributing to the formation of the two upper-tropospheric maxima

over the east ocean basins. BC has non-negligible contributions to the upper-tropospheric EKE maxima, although the main positive conversions associated with BC are still found in the lower troposphere over the west ocean basins (Fig. 2.7d). The overall impact of EFC in determining the upper-tropospheric maxima of IF EKE is relatively small compared to that in the HF EKE budget. Further breakdown of the EFC term indicates that it is also dominated by the energy convergence due to the vertical component of the geopotential flux (figure not shown). CFEI (Fig. 2.7f), another critical source of IF EKE, is mainly contributed by the EKE generation due to interaction between HF and IF eddies (HI, Fig. 2.7e). The zonal and vertical distribution of HI indicates that such nonlinear interactions preferentially occur in the mid-upper troposphere over Eastern Pacific-Western North America and over Eastern Atlantic-Western Europe. Both regions are characterized by an elevated activity of atmospheric blocking. The positive role played by HI in the IF EKE budget therefore provides additional evidence that synoptic-scale transients and eddy-eddy interactions are an integral part of the dynamics of atmospheric blocking [e.g., *Egger*, 1978; *Nakamura and Wallace*, 1990; 1993; *Nakamura et al.*, 1997; *Shutts*, 1983; 1986]. Consequently, one of the potential applications of the local energetics diagnosis presented here is model evaluations that seek to identify sources of biases and improve the representation of blocking events in a global model.
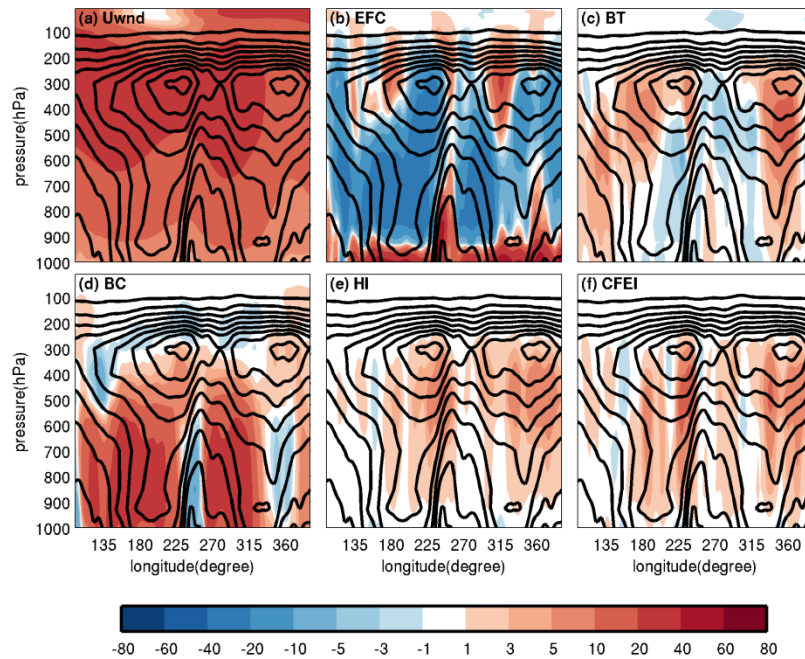
Figure 2.7: Same as Fig. 2.3 except for IF eddies.

2.4 Summary

In this section, we quantify the winter climatology of the local kinetic energy budget terms for both the HF and IF eddies. HF eddies depict extratropical storm tracks that are responsible for day-to-day weather variability in northern winter while IF eddies represent the class of relatively low-frequency disturbances giving rise to phenomena such as atmospheric blocking and teleconnections. By adopting a new form of the EKE equation, we are able to isolate the effect of EKE generation/destruction due to interactions among eddies of different timescales. The so-called CFEI term is a

significant sink of HF EKE and a major source of IF EKE over both the North Pacific and North Atlantic basins. The results of local energetics, presented in the forms of both tropospheric-average and latitude/longitude-pressure cross-sections, confirm findings in earlier studies that synoptic-scale disturbances contribute positively to the onset and maintenance of extratropical atmospheric low-frequency variability, particularly over the eastern ocean basins. In the winter climatology, BT is most active in the mid and upper troposphere while BC is concentrated below 500 hPa. BC contributes positively to both HF and IF EKE while BT often damps HF EKE and enhances IF EKE. The mean-flow advection of EKE and kinetic energy dispersion, captured in the EFC term, are always important in determining the final 3D distribution of EKE in the troposphere.

The results presented here demonstrate that in terms of local energetics, IF eddies are more complicated compared to HF eddies. Diagnosing local energetics of transient eddies of various timescales thus can serve as an efficient tool for identifying sources of differences in general circulation features among various reanalysis datasets and model simulations. Finally, it is important to recognize here that kinetic energy budget represents only one part of the total eddy energy budget.

The work presented in this chapter is published in Climate Dynamics [Jiang et al., 2013]

CHAPTER 3

MODULATION OF THE ATMOSPHERIC DISTURBANCES BY

TROPICAL AND EXTRATROPICAL VARIABILITY AND THE

INFLUENCE TO WESTERN NORTH AMERICAN WATER CYCLE

3.1 Interannual Timescale Modulations

3.1.1   Interannual Variability of Local Energetics

The interannual variability of the various energy conversion terms constitutes an important aspect of the EKE budget, in some sense, it represents a "mean state" of the variability itself. We first quantify the overall amplitude of the interannual variation in various budget terms in terms of the standard deviation of their respective DJF-mean values. Figure 3.1 presents the results for HF eddies. The maximum standard deviations of EFC, BC and BT, shown in Figs. 3.1b, 3.1c and 3.1d, respectively, are located downstream of the corresponding time-mean jets over the western North Pacific and western North Atlantic. The maximum interannual variability of CFEI (Fig. 3.1f) is found over the eastern North Pacific and over the western North Atlantic. Over both basins, EFC exhibits the largest interannual variability among all the budget terms. The magnitudes of interannual variations in terms of standard deviations are generally larger over the North Atlantic than those over the North Pacific, likely a result of larger eddy

amplitudes in the former region. On average, interannual variability represents approximately 20-70% changes with respect to the local climatological values.
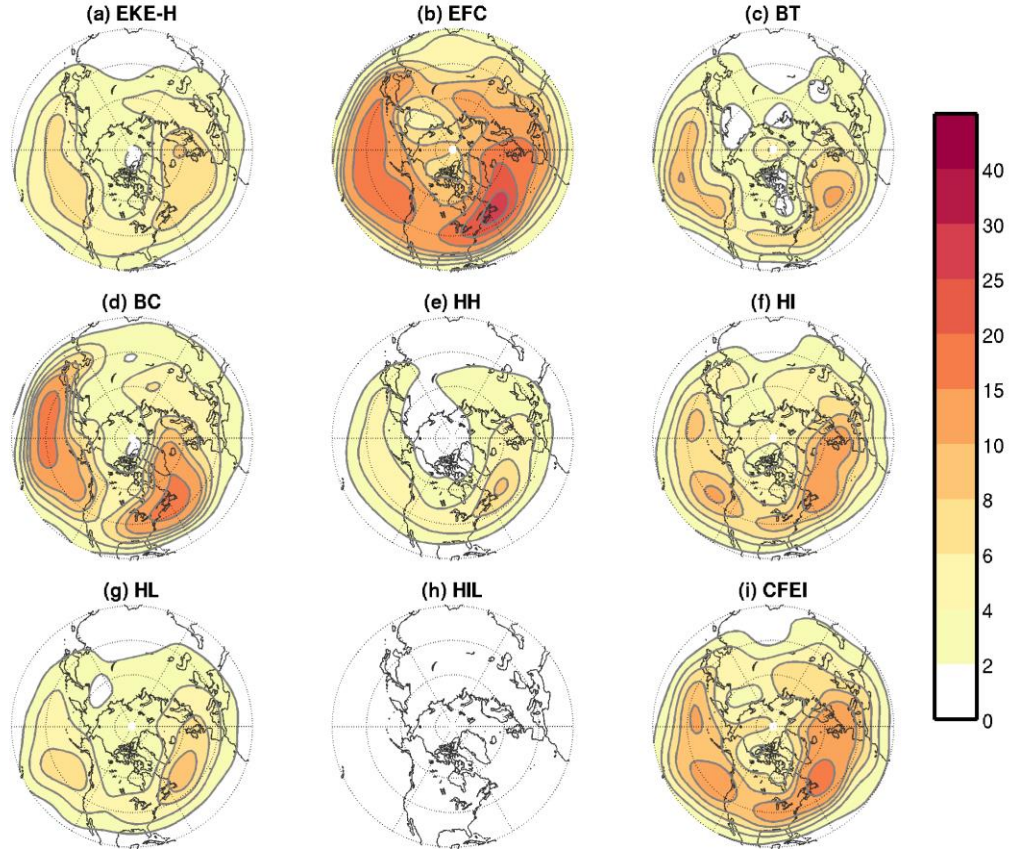
Figure 3.1: Interannual standard deviations of the HF EKE budget terms in winter season. (a) HF EKE (contour interval: $10m^2/s^2$); (b) EFC; (c) BT; (d) BC; (e) HH; (f) HI; (g) HL; (h) HIL; (i) CFEI. Units in (b)-(i) are m^2s^{-2}/day. All data have been spectrally truncated to T15 before plotting. For detailed definitions of various budget terms, please refer to table 2.1.

The overall spatial structure of the interannual variability in the IF EKE budget terms (Fig. 3.2) is similar to that of the HF EKE budget terms in the sense that the maximum variability tends to overlap with the maximum climatological values of the respective terms. For IF eddies, EFC shows the largest amplitude of interannual variation among all the budget terms, and it is equivalent to more than 100% changes with respect

to the climatological values over Gulf of Alaska and the North Atlantic (Fig. 3.2b). The

interannual variability of BT (Fig. 3.2c) in the IF EKE budget shares similar spatial

patterns with that in the HF EKE budget (Fig. 3.1c) but with a larger amplitude. The

amplitude of the interannual variability of BC, on the other hand, is weaker for IF eddies

(Fig. 3.2d) compared to that for HF eddies (Fig. 3.1d). The standard deviations of the

CFEI term turn out to be large for both HF and IF eddies (Fig. 3.1i and Fig. 3.2i). A

distinction between the HF and IF eddies is that the magnitude of the interannual

variability of the interaction among eddies of similar scales, i.e., HH (Fig. 3.1e) and II

(Fig. 3.2e), is quite different. II clearly varies more substantially on a year-to-year basis

compared to HH.
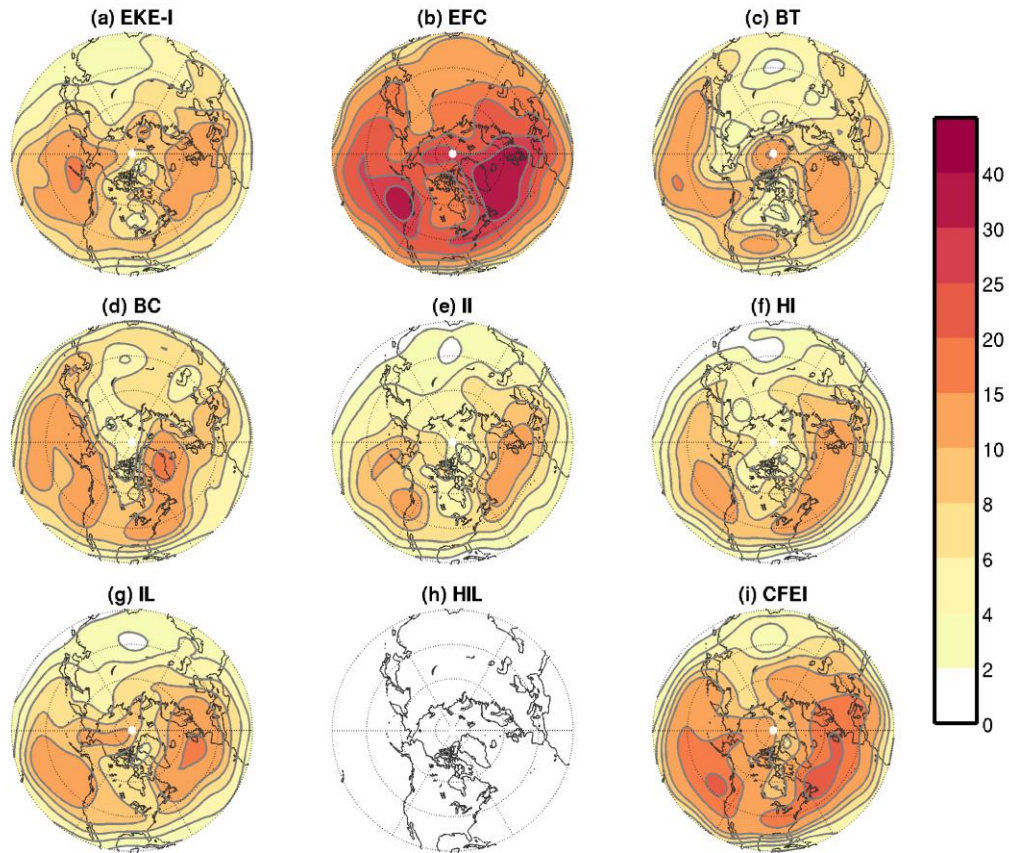
Figure 3.2: Interannual standard deviations of the IF EKE budget terms in winter season. (a) IF EKE (contour interval: $10 m^2/s^2$); (b) EFC; (c) BT; (d) BC; (e) II; (f) HI; (g) IL; (h) HIL; (i) CFEI. Units in (b)-(i) are $m^2 s^{-2}$/day. All data have been spectrally truncated to T15 before plotting. For detailed definitions of various budget terms, please refer to table 2.2.

3.1.2 A Special Case of Interannual Modulations: ENSO

ENSO represents the most prominent signal of interannual variability in the Earth's climate system and has profound impacts on global atmospheric circulation [e.g., *Bjerknes*, 1969; *Trenberth et al.*, 1998]. To investigate the influence of ENSO on local EKE budgets, we regress DJF-mean values of the zonally- and vertically-averaged energy conversion terms onto the Nino3.4 index. The longitudinal sectors for zonal averaging is

38

chosen based on regions exhibiting maximum interannual variability as shown in Figs. 3.1 and 3.2 The meridional distribution of the regression coefficients for the HF EKE budget terms are plotted in Figure 3.3. A meridional dipole in the regression coefficients for HF EKE over the North Pacific (thick black line in Fig. 3.3a) indicates an equatorward shift of the Pacific storm track during El Niño winters as discussed in previous studies [e.g., *Trenberth and Hurrell*, 1994]. The elevated level of EKE on the equatorward side of the climatological storm track is accompanied by a southward shift of the maximum BC (red line in Fig. 3.3a) and positive anomalies of BT around 35°N (cyan line in Fig. 3.3a). The decrease of HF EKE to the north is a result of negative conversion anomalies in BC. In contrast, both EFC (thin black line in Fig. 3.3a) and CFEI (magenta line in Fig. 3.3a) work against the observed pattern of EKE anomalies meaning positive (negative) EFC and EFC anomalies are found where EKE anomalies are negative (positive).
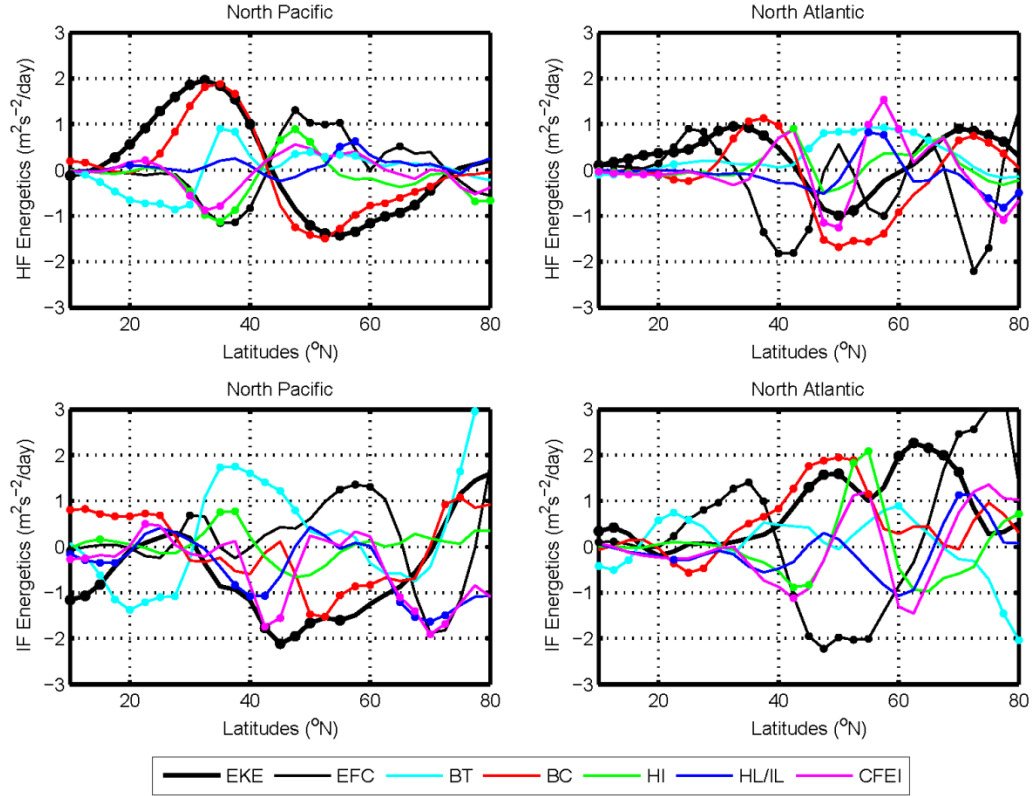
Figure 3.3: Response of the EKE budget terms to ENSO forcing in terms of coefficients obtained by regressing the corresponding budget terms onto the monthly Nino3.4 index. (a) HF EKE budget terms that are zonally-averaged over the North Pacific basin (140°E-120°W) and mass-weighted, vertically-averaged in the troposphere; (b) HF EKE budget terms that are zonally-averaged over the North Atlantic basin (90°W-0°E) and mass-weighted, vertically-averaged in the troposphere. (c) IF EKE budget terms that are zonally-averaged over the North Pacific basin (160°E-110°W) and mass-weighted, vertically-averaged in the troposphere. (d) IF EKE budget terms that are zonally-averaged over the North Atlantic basin (60°W-30°E) and mass-weighted, vertically-averaged in the troposphere. The EFC term in IF EKE budget (c) and (d) is scaled by 0.5 to fit the panels. The blue solid lines in (a) and (b) represent HL in the HF EKE budget; while in (c) and (d) they represent IL in the IF EKE budget. The unit for EKE anomalies is m^2s^{-2}/K, and $m^2s^{-2}day^{-1}K^{-1}$ for rest of the terms. Results passed the 80% significance level are marked with filled circle.

Over the North Atlantic, the ENSO response in the HF EKE field is characterized by

a tri-pole anomaly with decreased EKE in midlatitudes (around 50°N) and increased EKE

in subtropics and high latitude regions (thick black line in Fig. 3.3b). Note that due to the southwest-northeast tilt of the North Atlantic storm track, zonal averaging tends to smooth out the signal. The results presented in Fig. 3.3b are thus a slight underestimate of the actual response. The tri-pole anomaly in HF EKE over the North Atlantic is largely induced by anomalies in BC (red line in Fig. 3.3b) and CFEI (magenta line in Fig. 3.3b). Similar to that over the North Pacific, EFC tends to work against this tri-pole anomaly (thin black line in Fig. 3.3b). BT (cyan line in Fig. 3.3b) also works against the decrease of HF EKE around 50°N. Comparing the response of the eddy-eddy interaction term over the two oceanic basins, we find that HI (green line in Fig. 3.3a) dominates the response of CFEI over the North Pacific while both HI (green line in Fig. 3.3b) and HL (blue line in Fig. 3.3b) are relevant for the CFEI response over the North Atlantic.

The corresponding results for IF EKE are shown in Figs. 3.3c and 3.3d. In response to El Niño events, IF EKE generally decreases across the North Pacific between 30°N and 70°N with the maximum decrease found around 45°N (thick black line in Fig. 3.3c). Similar to the HF EKE over the North Pacific, the suppressed IF EKE is clearly associated with negative anomalies of BC (red line in Fig. 3.3c) north of 50°N and EFC (thin black line in Fig. 3.3b) works against the observed EKE anomalies in the midlatitudes. In contrast to the HF EKE, the suppression of IF EKE is also tied to negative anomalies of CFEI (magenta line in Fig. 3.3c), which is dictated by changes in IL (blue line in Fig. 3.3c) between 40°N and 50°N. Unlike that in the HF EKE budget, the

41

effect of BT in the IF EKE budget (cyan line in Fig. 3.3c) tends to work against the IF

EKE anomalies at low and mid-latitudes, while it is clearly contributing positively to the

IF EKE anomalies north of 65°N.

In contrast to the North Pacific, IF EKE generally increases over the North Atlantic

in El Niño winters and the maximum increase is located between 40°N and 70°N (thick

black line in Fig. 3.3d). This increase is largely contributed by a positive BC anomaly

(red solid line in Fig. 3.3d) between 40°N and 60°N while CFEI (magenta line in Fig.

3.3d) and BT (cyan line in Fig. 3.3d) also play some roles north of 50°N. The CFEI

response receives similar contributions from HI (green line in Fig. 3.3d) and IL (blue line

in Fig. 3.3d) north of 50°N. EFC term (thin black line in Fig. 3.3d), on the other hand,

still works against the observed EKE anomalies, particularly between 40°N and 70°N.

3.1.3 *The HF Disturbances and Low Frequency Modes: Extreme Drought In Southern*

   Great Plains During The Winter of 2005-2006

In 20th century, people live in the U.S. Great Plains suffered a number of major

droughts, most notably the droughts of the 1930s, the 1950s, and 1988 [*Schubert et al.*,

2004a; b; *Seager et al.*, 2005]. During hydrological year 2006 (October 2005 to

September 2006), extreme drought occurs in the Southern Great Plains (SGP). In the state

of Oklahoma, the annual precipitation amount is about 61% of the normal year; more

specifically, during the winter of 2005-2006, the seasonal precipitation amount (27% of

the normal year) break the historical record, ranked as the driest winter season as reported by *Dong et al.* [2011].

This persistent extreme drought event is inevitably associated with local feedback among cloud properties, radiation and precipitation. However, Rauber et al. (2008) point out that SGP winter precipitation is typically associated with the passage of the extratropical cyclones, a typical weather phenomenon related to HF eddies; therefore, it is important to examine the anomalous activity of these synoptic scale (HF), precipitation producing systems during winter months. Understanding the connection between this anomalous cyclonic activity and large−scale teleconnection patterns helps to infer potential predictability of winter hydrological extremes over the SGP region.

To analyze the activity of extratropical cyclones in this region, firstly, we need to derive a set of "winter storm tracks" via a "feature tracking" algorithm in Lagrangian framework which proposed by *Hoskins and Hodges* [2002]. In our analysis, we apply the same idea to the sea level pressure (SLP) and geopotential height in 300 hPa level acquired from NASA Modern Era Retrospective-Analysis for Research and Applications (MERRA) reanalysis from 1979 to 2009; the captured tracks are then interpolated onto a 1 degree by 1 degree grid based on Cressman method [*Cressman*, 1959] with both the instantaneous storm intensity (local minima) and influential radius considered. The accumulated result is named as cyclonic activity intensity. Figure 3.4 present a map of all the cyclone tracks (green trajectories) and the mean interpolated cyclonic activity during

the winter of 2005-2006 from the SLP data (gray shading). Two striking features are

shown here: firstly, the pattern of cyclonic activity intensity is largely consistent with the

storm tracks or HF EKE with two prominent maxima over North Pacific and North

Atlantic; secondly, for SGP region, the experienced cyclones can either originate from

North Pacific or from the high latitudes regions of western continent of North American,

in either case, the associated large-scale systems could produce impact to SGP region.
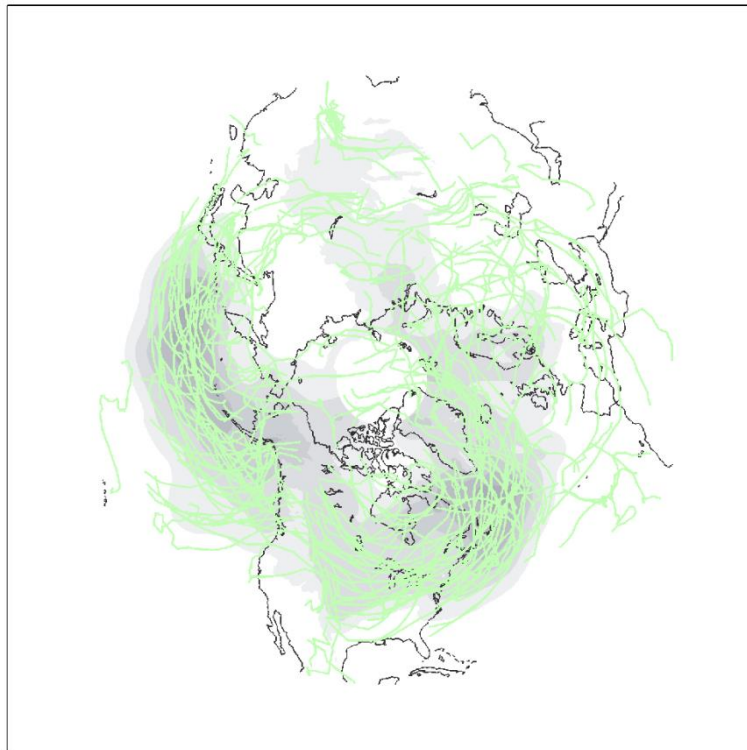
Figure 3.4: Extratropical cyclone tracks (green trajectories) and the corresponding track
intensity (gray shading) derived from SLP field in MERRA reanalysis data for winter
2005- 2006.

Figure 3.5a shows the correlation between the monthly cyclonic activity over the

continental United States and the precipitation over a grid box of $30°-40°N$ and $105°-$

$95°W$ representing the broader SGP region during the period November–February

1979/1980–2008/2009 (note that the sign of precipitation was reversed in the calculation

to reflect the drought condition). The winter precipitation deficit over the SGP is clearly

linked to significantly suppressed cyclonic activity (i.e., negative anomalies) over the

southwestern United States. This result is consistent with a winter cyclone's westward tilt

with height, thus the fact that the surface precipitation zone tends to be located to the east

of the upper level (300 hPa) trough. The suppressed cyclonic activity (Fig. 3.5b) and

positive 500 hPa geopotential height anomalies (Fig. 3.5c) over the southwestern United

States have demonstrated that large−scale flow anomalies play a key role in leading to the

extreme dry period.

(a)   (b)
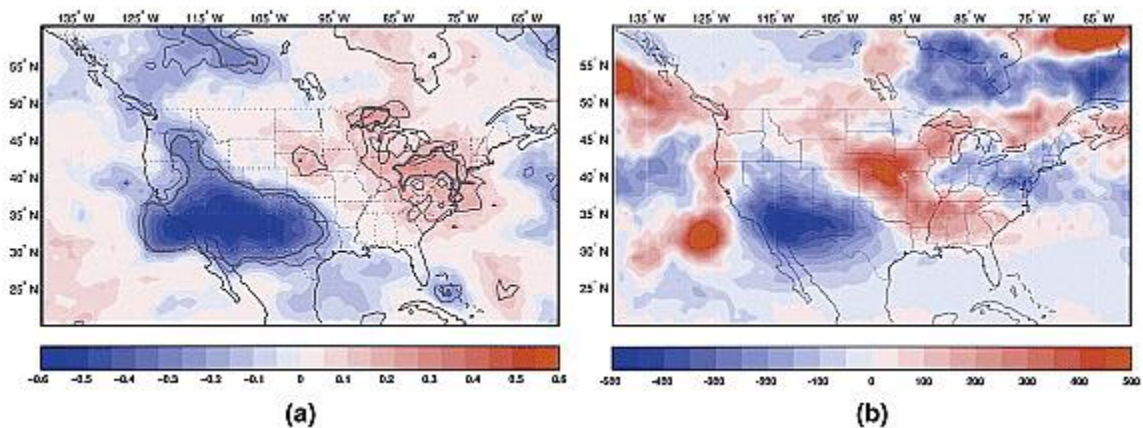
Figure 3.5: (a) Correlation between the monthly cyclonic activity over the continental United States and the precipitation (from the MERRA precipitation) over a grid box of 30°–40°N and 105°–95°W during the period November to February 1979/1980–2008/2009 (sign of the precipitation is reversed to reflect the drought condition). (b) Anomalies of the cyclonic activity during the extreme dry period (November 2005 to February 2006) relative to the 1979/1980–2008/2009 climatology (color shadings in meters per day). Thick (thin) contours in Figure 10a correspond to the 99% (95%) level of statistical significance.

To find out what teleconnection patterns can modulate the cyclonic activity over the

southwestern United States and therefore drive the winter precipitation variability in the

SGP, we first defined a Cyclonic Activity Index (CAI) by integrating anomalies of the

cyclonic activity over 30°–37°N and 120°–100°W representing the southwestern United

States. The correlation coefficients between this index and the Northern Hemisphere 500

hPa geopotential height (GH) are given in Figure 3.6a, where enhanced cyclonic activity

in winter is generally associated with positive (negative) height anomalies over the

western Pacific regions south (north) of Japan and with negative height anomalies over

the southwestern United States. The suppressed cyclonic activity during the extreme dry

period thus corresponds to the exact opposite of the anomalous pattern shown in Figure

3.6a. This triple action-center pattern clearly resembles the loading pattern of the WP

teleconnection, a primary low frequency mode over the North Pacific [*Barnston and*

Livezey, 1987; *Wallace and Gutzler*, 1981]. In fact, the correlation between the

November–February averaged CAI and the WP index is 0.43 and statistically significant

at the 99% level (Fig. 3.6c). The southwestern CAI is also slightly correlated with the

PNA index on monthly time scales with a correlation coefficient of 0.21 statistically

significant at the 95% level (Fig. 3.6b). Since positive phases of WP and PNA are

characterized by negative GH anomalies over western North America and the North

Pacific, respectively, and such anomalies tend to push westerly jets southward and

enhance upper level divergence downstream of the geopotential height anomalies, the

positive phases of WP and PNA can contribute to increased cyclonic activity over the

Southwest. This is consistent with the positive correlations between the CAI and WP/PNA identified above. Given the linkages between the CAI (therefore, the SGP precipitation) and the WP and PNA index on, respectively, seasonal and monthly time scales, improved understanding and simulation of the WP and PNA variability have strong implications for future studies that explore the predictability of the SGP winter hydrological extremes.
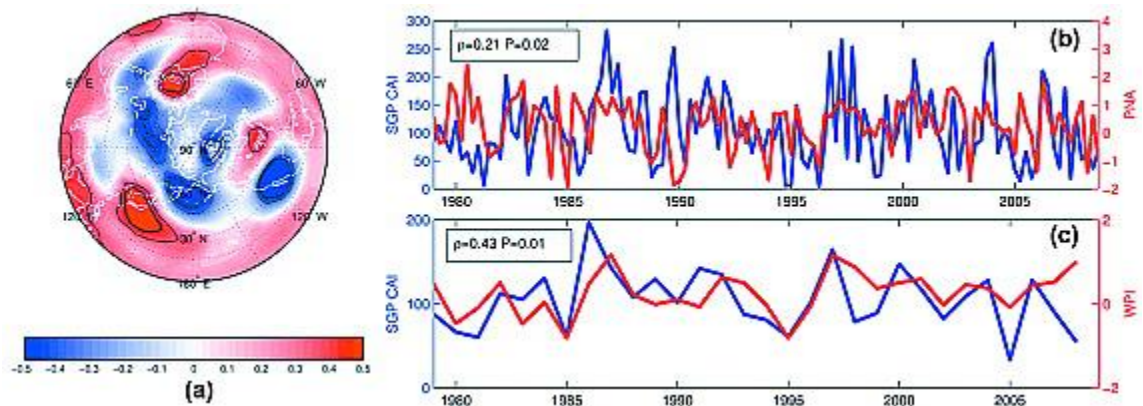
Figure 3.6: Correlation between the (a) November–February averaged 500 hPa GH and the CAI, (b) monthly CAI (blue line) and the corresponding NOAA PNA index (red line) during November–February 1979/1980–2008/2009, and (c) November–February averaged CAI and the corresponding NOAA WP index during November–February 1979/1980–2008/2009. Thick (thin) contours in Figure 11a correspond to the 99% (95%) level of statistical significance. The source of the PNA and WP index is http://www.cpc.noaa.gov/data/teledoc/telecontents.

3.2 Tropical Intraseasonal Scale Modulations

3.2.1. *Motivation*

The response of the extratropical circulation to the Madden-Julian Oscillation , the

prominent intraseasonal convection system, has been actively studied in the past thirty years. Early work represented by *Weickmann* [1983] and *Weickmann et al.* [1985] demonstrated that the extratropical flow anomaly associated with the MJO variability is characterized by an eastward propagating, wavenumber-1 structure manifesting itself as an eccentric circumpolar vortex expanding (contracting) in regions of enhanced (suppressed) tropical convection. *Weickmann et al.* [1992] and *Weickmann et al.* [1997] further investigated the atmospheric angular momentum (AAM) cycle associated with the MJO and discussed the dynamics of the intraseasonal AAM oscillations. Most recently, *Egger and Weickmann* [2007] showed that during the lifecycle of MJO, AAM anomalies of one sign first develop in the tropical upper troposphere and propagate downward and poleward to the subtropics in about two weeks, at which time AAM anomalies of the opposite sign start to appear in the tropical upper troposphere. *Matthews et al.* [2004] provided a good review on this topic but focused their discussion on the direct response to tropical heating that can be understood with a barotropic model, i.e., quasi-stationary, extratropical waves driven by time-dependent, tropical heat source derived from the observed MJO anomalies [e.g., *C Zhang and Hagos*, 2009]. *Pan and Li* [2008] further suggested that synoptic-scale transients play a key role in the interaction between tropical intraseasonal oscillation and mid-latitude low frequency flow. *Matthews and Kiladis* [1999] presented a pioneering analysis on the interaction between high-frequency transients and the MJO. They showed that during the early phase of the MJO when the

enhanced convection is located over the East Indian Ocean, the upper level Asian-Pacific jet and the tropical easterlies move westward, leading to a "leakier" waveguide along the jet and strengthened equatorward propagation of transient eddy activity into the tropical central Pacific. The enhanced convective variability associated with stronger transient eddy activity at the ITCZ projects back onto the intraseasonal timescale and become an integral part of the slowly evolving MJO signal. As the enhanced convection moves over the South Pacific Convergence Zone (SPCZ), a stronger Asian-Pacific jet (waveguide) extends over the central Pacific suppressing equatorward propagation of wave activity. Note that in this work, "high-frequency" is obtained through a 6-25 day band-pass filter and does not correspond exactly to the typical 2-8 day timescale of synoptic eddies comprising a storm track, although the authors did mention that the magnitude of the anomalies of the perturbation kinetic energy almost doubled over the North Pacific when a 25-day high-pass filter was used in calculation. Therefore, there is still missing in the literature a comprehensive analysis of the intraseasonal modulation of the North Pacific storm track by tropical convection in boreal winter.

Additional implications of a tropical-convection-induced stormtrack anomaly include its projection onto regional hydro-climate variability in winter. *Myoung and Deng* [2009] showed that by affecting coastal cyclonic activity, synoptic eddies existing the Pacific storm track determine a large portion of the interannual variance of the winter precipitation characteristics in western U.S. Moreover, a series of studies have

demonstrated that the amplitude and location can significantly alter the moisture transport and further affect the extreme precipitation over U.S. west coast [*Higgins and Mo*, 1997; *Higgins et al.*, 2000; *Jones*, 2000; *Jones et al.*, 2004; *Mo and Higgins*, 1998; *Mo and Higgins*, 1998].

The aim of Section 3.2 is to 1) quantify the observed Pacific storm track anomalies during the course of a typical MJO event, 2) identify the key dynamical processes leading to the storm track anomalies by diagnosing the HF EKE budget, 3) investigate the role of the MJO-induced, anomalous synoptic eddy forcing in driving the extratropical intraseasonal flow anomalies, and 4) explore the implications of this storm track variability for subseasonal prediction of the winter hydrological condition in western North America.

3.2.2. Data and Methods

The analysis of this study focuses on the most recent 30 winters (December-March, 1979/80-2008/09). The main dataset used is the NCEP/NCAR Reanalysis [*Kalnay et al.*, 1996; *Kistler et al.*, 2001]. The daily values of the NOAA Interpolated Outgoing Longwave Radiation [OLR, *Liebmann and Smith*, 1996] on a $2.5°$ latitude $\times$ $2.5°$ longitude grid are used as the basis for characterizing intraseasonal variations in the tropical convection.

The intensity of the North Pacific storm track is measured in terms of the

mass-weighted, vertically-averaged HF EKE in the troposphere. A 30-90 day band-pass Lanczos filter with 181 daily weights is applied to variables such as daily OLR, HF EKE, zonal wind and precipitation to extract the intraseasonal fluctuations in these fields. The number of weights used in the filter is increased for lower values of cutoff frequencies to ensure a sharp frequency response [*Duchon*, 1979].

A Multivariate Empirical Orthogonal Function Analysis (MEOF) is conducted on the 30-90 day filtered, daily HF EKE (defined over 110°E-100°W, 5°N-65°N) and tropical OLR field (defined over 90°E-90°W, 15°S-5°N) to identify the dominant structure of intraseasonal coupling between the North Pacific storm track and tropical convection. Before solving for the eigenvectors of the correlation matrix, the filtered daily HF EKE and OLR values at each grid-point have been centered (i.e., temporal-mean removed) and normalized respectively by the standard deviation of the filtered daily HF EKE and OLR time series at the same grid-point. The results of the MEOF analysis turn out not sensitive to small changes in the choice of the HF EKE and OLR domain.

Composite maps for multiple fields including the HF EKE, precipitation and various local energy conversion terms are created based upon the time series of the Principal Components (PCs) obtained in the MEOF analysis. A day is denoted as a "day 0" when the anomaly of the daily PC value rises above one standard deviation and is greater than the anomaly values of at least 25 days preceding and 25 days following that day. A total

of 73 day 0s are identified out of the 30 winters being studied. This gives us a set of 73

events for case-compositing. Composite daily anomalies of various 30-90 day band-pass

filtered fields, i.e., composite "intraseasonal" anomalies, are constructed from day -30 to

day 30 by averaging the corresponding daily fields across the 73 cases selected.

Statistical significances of the composites are assessed through Welch's t-test [*Welch*,

1947]. Two periods characterized by pronounced HF EKE response to intraseasonal

tropical OLR anomalies are identified through the MEOF analysis and designated as

period I and II. They correspond to day -7 to day +7 and day +15 to day +29, respectively.

Most results of the composite analysis are presented as averages over each of the two

Periods.

For the HF EKE local energetics analysis, we use the HF EKE budget with

cross-frequency energy exchange terms derived in Chapter 2.

3.2.3. Linear Modulation of the Pacific Storm Tracks by Tropical Convection

The linearly co-varying patterns of the Pacific storm track and tropical OLR on

intraseasonal timescales are first identified through a MEOF analysis on the filtered HF

EKE and OLR field. The top three EOFs account for respectively 11.7%, 8.3% and 6.4%

of the total intraseasonal variance in the two fields. The HF EKE and OLR EOFs, in

terms of the coefficients of regression onto the corresponding normalized PC time series,

are shown in Fig. 3.7 and 3.8, respectively. $EOF1_{HFEKE}$ (Fig. 3.7b) has a monopole

structure indicating increase or decrease of the overall intensity of the Pacific storm track. This mode of storm track variability is largely independent of the tropical OLR as the amplitude of the corresponding $EOF1_{OLR}$ (Fig. 3.8a) is rather weak across the entire tropical region being considered. $EOF2_{OLR}$ (Fig. 3.8b) and $EOF3_{OLR}$ (Fig. 3.8c), on the other hand, indicate an eastward propagating OLR-couplet with the negative anomaly (enhanced convection) located to the west of the positive anomaly (suppressed convection). The center of the enhanced convection moves from about 110°E in $EOF2_{OLR}$ to about 160°E in $EOF3_{OLR}$. According to the multivariate MJO index defined by Wheeler and Hendon (2004), this movement roughly corresponds to the phase 4 to phase 6 evolution of the MJO-related OLR signal over the tropical oceans. The storm track response, i.e., $EOF2_{HFEKE}$ (Fig. 3.7b), is characterized by a dipole anomaly over the North Pacific with above-normal HF EKE over mid-high latitudes and below-normal HF EKE over the subtropical eastern Pacific. The slightly above-normal HF EKE is also observed over the tropical-subtropical central Pacific around the International Date Line. The eastern portions of the storm track anomalies exhibit a general northwest-southeast (NW-SE) tilt. In $EOF3_{HFEKE}$ (Fig. 3.7c), the overall distribution of the storm track anomaly is displaced northeastward compared to $EOF2_{HFEKE}$, with a negative anomaly now dominating the mid-high latitudes and a positive anomaly appearing over the subtropical eastern Pacific.
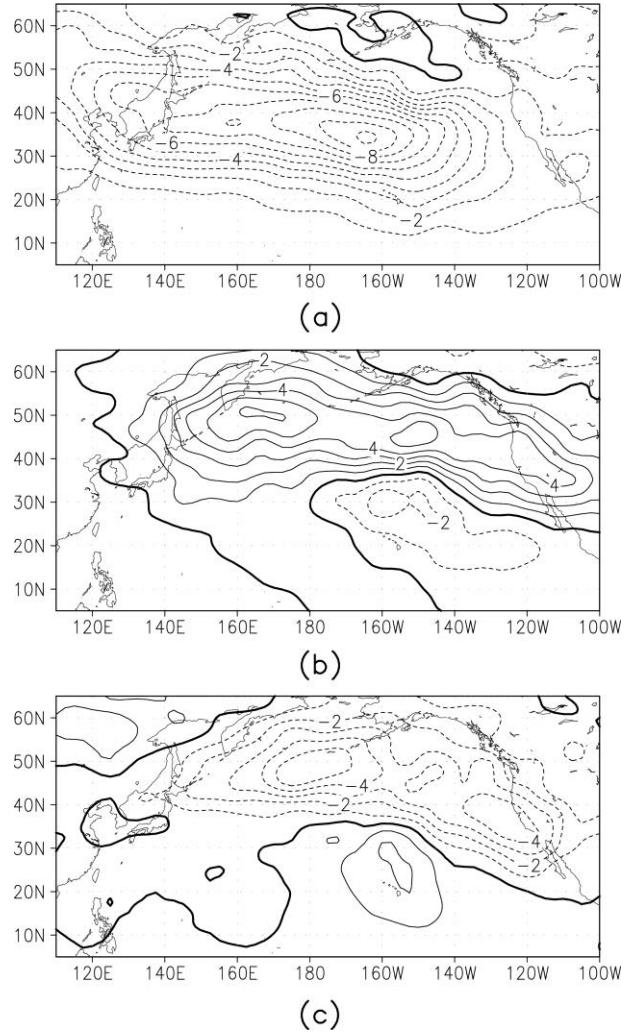
Figure 3.7: The first 3 EOF modes of the HF EKE shown as the regression coefficients between the intraseasonal HF EKE and the corresponding normalized PC time series: (a) $EOF1_{SEKE}$, (b) $EOF2_{SEKE}$, and (c) $EOF3_{SEKE}$. Contour interval is $1\ m^2\ s^{-2}$. Solid (dashed) contours correspond to positive (negative) values and 0 contours are highlighted. Displayed are values reaching the 95% significance level.
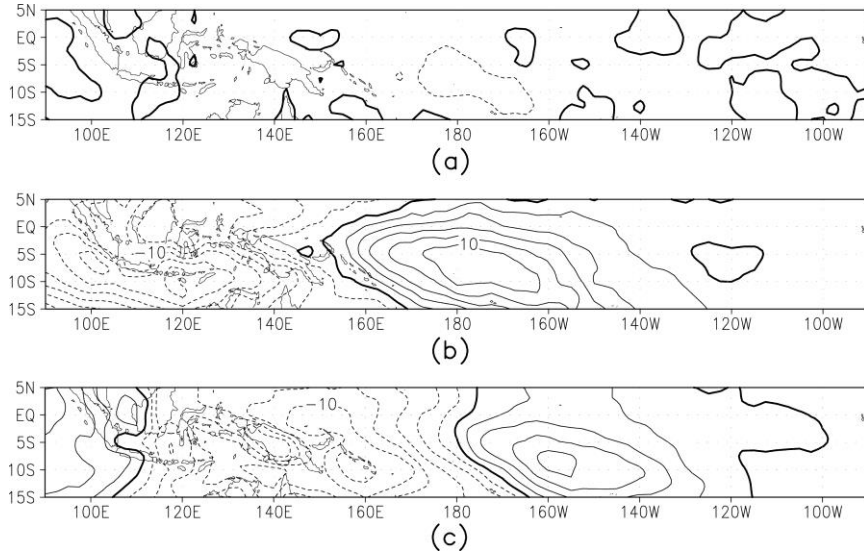
Figure 3.8: The first 3 EOF modes of the tropical OLR shown as the regression coefficients between the intraseasonal OLR and the corresponding normalized PC time series: (a) EOF1$_{OLR}$, (b) EOF2$_{OLR}$, and (c) EOF3$_{OLR}$. Contour interval is 2 W m^{-2}. Solid (dashed) contours correspond to positive (negative) values and 0 contours are highlighted. Displayed are values reaching the 95% significance level.

3.2.4. *Development of The Storm Track Anomalies*

The development of the storm track anomalies during the course of a typical MJO event is further examined through case compositing. Day 0s (please see the definition in Section 3.2.2) are selected based upon the second PC (PC2) time series obtained during the MEOF analysis. Fig. 3.9 illustrates the distributions of the lagged regression coefficients between the intraseasonal tropical OLR anomalies and the normalized PC2 time series. At day -15 (Fig. 3.9a), a negative OLR anomaly emerges over the Indian Ocean and a positive anomaly appears over the western Pacific. The amplitude of the negative (positive) anomaly increases (decreases) as this OLR-couplet propagates

55

eastward between day -15 and day +5 (Fig. 3.9b and c). By day +15 (Fig. 3.9d), the positive OLR anomaly has disappeared over the central Pacific and another positive anomaly is found over the Indian Ocean. At day +25 (Fig. 3.9e), the negative OLR anomaly reaches the central Pacific and is now located south of the equator. The intraseasonal evolution of the tropical OLR associated with the coupled HF EKE-OLR variability (PC2) is thus consistent with the lifecycle of a typical MJO event [e.g., Fig. 8 of *Wheeler and Hendon*, 2004].
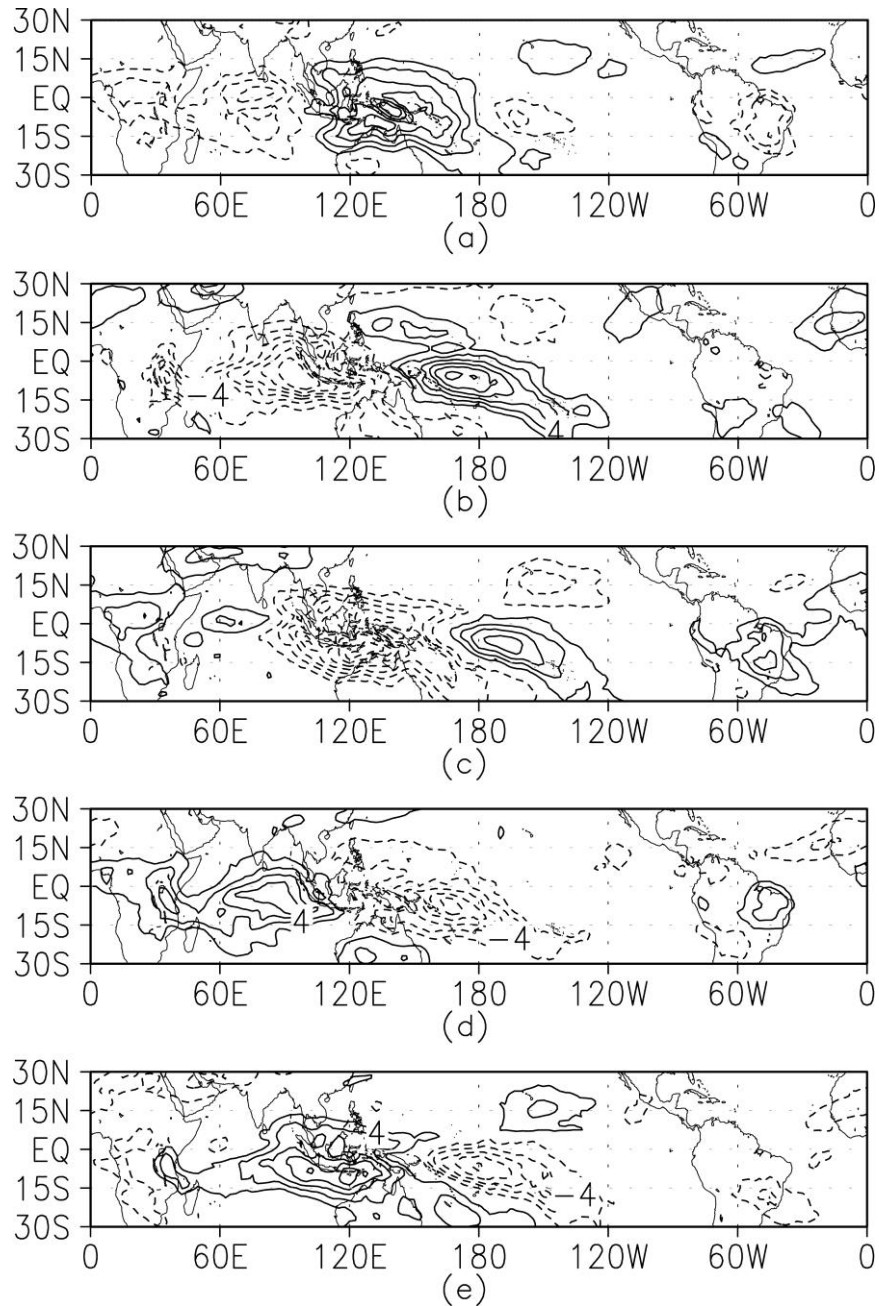
Figure 3.9: The distribution of the lagged regression coefficients between the intraseasonal tropical OLR anomalies and the normalized PC2 time series at (a) day −15, (b) day −5, (c) day +5, (d) day +15, and (e) day +25. Contour interval is 2 W m^{-2}. Solid (dashed) contours correspond to positive (negative) values and 0 contours are omitted. Displayed are values reaching the 95% significance level.

Fig. 3.10 displays the composite intraseasonal anomalies of HF EKE for the two periods defined in Section 3.2.2. Period I (day -7 to day +7, Fig. 3.10a) is centered about

57

day 0, the time of the peak amplitude of the second EOF mode (Fig. 3.7b and 3.8b).

During this period, the negative OLR anomaly in the tropics is located over the eastern

Indian Ocean and maritime continent (Fig. 3.9b and c). The Pacific storm track

strengthens across the North Pacific between 35°N and 60°N and weakens over the

tropical-subtropical eastern Pacific. The slightly enhanced synoptic eddy activity

(positive HF EKE anomalies) over the tropical-subtropical central Pacific is consistent

with the presence of a "leakier" waveguide over the North Pacific during this stage of

MJO as discussed by *Matthews and Kiladis* [1999]. The major difference is here we focus

on eddies with shorter timescales (2-8 day versus 6-25 day). As the negative OLR

anomaly moves eastward over the equatorial Pacific, the dipole storm track anomaly of

Fig. 3.10a propagates northeastward and the relative amplitude of the two centers of

action also evolves. In period II (day +15 to day +29), the center of the enhanced tropical

convection is now over the tropical western-central Pacific (Fig. 3.9d and e). The

corresponding HF EKE field (Fig. 3.10b) now indicates largely suppressed synoptic eddy

activity (negative HF EKE anomalies) north of 35°N and enhanced eddy activity over the

tropical-subtropical eastern Pacific. The overall anomaly distribution is almost the same

compared to that in Period I (Fig. 3.10a) but with opposite signs. Over the

tropical-subtropical central Pacific, the HF EKE anomalies are weakly negative at this

stage, which is in contrast with the positive values found in Period I. The similarities

between the Period I (II) HF EKE composite and the EOF1(2)$_{HF\,EKE}$ demonstrate that 1)

the second and third EOF mode indeed reflect respectively two consecutive stages during

the intraseasonal coupling between the HF EKE and tropical OLR, and 2) the response of

the North Pacific storm track to the intraseasonal variation in tropical convection is

largely linear. In general, this intraseasonal modulation can be described as a

northeastward-propagating, amplitude-varying dipole anomaly in the HF EKE field. If

counting in the weak yet distinct anomalies over the tropical-subtropical central Pacific,

the synoptic eddy activity over the North Pacific is characterized by a tri-pole pattern.
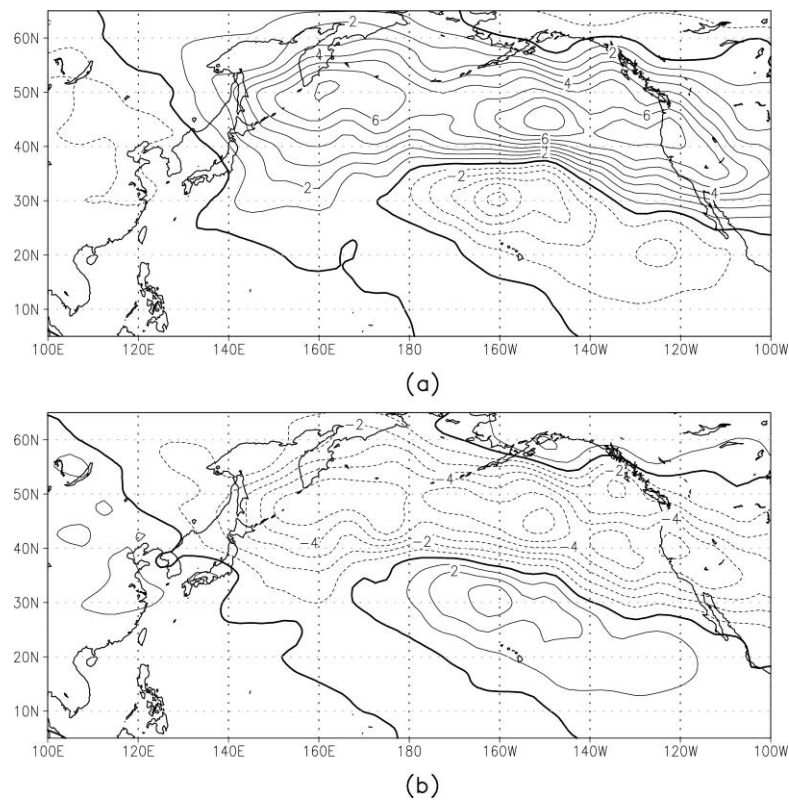
Figure 3.10: Composite intraseasonal storm-track anomalies in terms of the vertically (925–200 mb) averaged SEKE during (a) period I (b) and period II. Please refer to the text for the definition of the 2 periods. Contour interval is 1 $m^2\,s^{-2}$. Solid (dashed) contours correspond to positive (negative) values and 0 contours are highlighted. Displayed are values reaching the 95% significance level.

To explore the potential feedback of storm track anomalies to tropical convection, we document the temporal evolution of the meridional propagation of synoptic eddy energy across a subtropical zone (15 °N-20 °N) and compare this evolution to that of the synoptic variability in the tropical (0 °-15 °N) OLR during the course of a MJO event. The direction of eddy group velocity is approximately quantified by the barotropic E-vector, $\vec{E} = (E_x, E_y) = \left(\overline{v'^2} - \overline{u'^2}, -\overline{u'v'}\right)$, where u' and v' are the synoptic eddy component of the zonal and meridional wind, respectively, and overbar indicates time-averaging [*Hoskins et al.*, 1983]. Fig. 3.11a is a longitude-time plot showing the anomalies of the 2-8 day band-pass filtered tropical OLR variance (contour) between day -15 and day +30 together with the corresponding anomalies of the meridional component of the 250mb E-vector (E_y) averaged over 15 °N-20 °N (color shading). Between 140 °E and 170 °E, during the period day -15 to day +10, the equatorward propagation of synoptic eddy energy (negative values of E_y) leads an enhancement of the tropical OLR variability by about 3-5 days. After day +10, the sign of E_y changes and poleward propagation of eddy energy is now evident across the subtropics between 140 °E and 170 °E. This propagation also slightly leads the suppressed tropical OLR variability between day +12 and day +30. In Fig. 3.11b, the tropical OLR variance is replaced with the 30-90 day band-pass filtered OLR anomalies. A comparison between Fig. 3.11a and b indicates that enhanced (suppressed) synoptic variability of OLR is typically associated with negative (positive) intraseasonal anomalies of OLR except for a region around 170 °E between day

+10 and day +25. The equatorward propagation of the synoptic eddy energy identified between day -15 and day +10 over 140°E-170°E thus suggests a positive feedback of the storm track response to the eastward advance of the MJO-related OLR signal in the tropics, in terms of both its synoptic variability and intraseasonal anomalies. Similar behavior for transient eddies with lower frequencies was discussed by *Matthews and Kiladis* [1999]. No distinct feedback process is found for longitudes east of 170°E or after day +10.
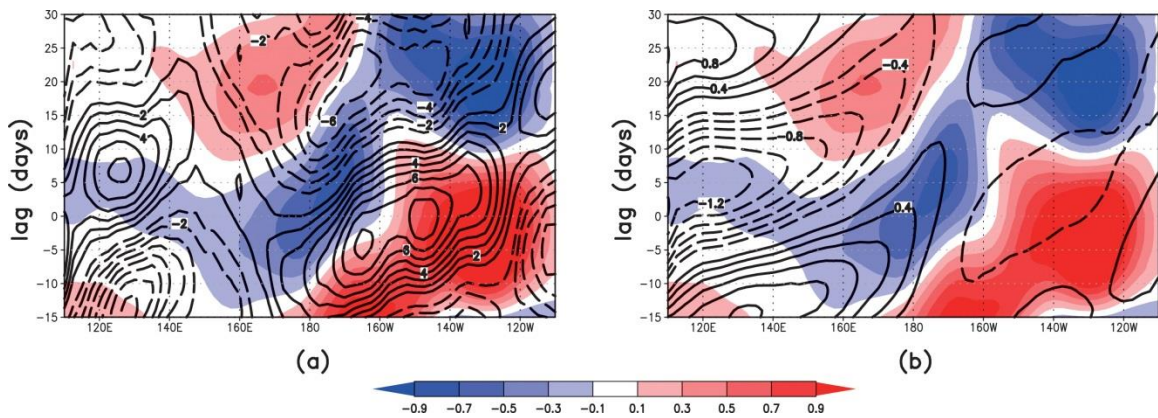
Figure 3.11: (a) Longitude–time plot of the composite intraseasonal anomalies of the 2–8-day bandpass-filtered OLR variance (contours) averaged over $0°$–$15°N$ and the composite intraseasonal anomalies of E_y (color shading) averaged over $15°$–$20°N$. (b) As in (a), but for the contours now corresponding to the composite intraseasonal (30–90-day bandpass-filtered) anomalies of the OLR averaged over $0°$–$15°N$. Contour interval is 1 $W^2\,m^{-4}$ in (a) and 0.2 W m^{-2} in (b). Solid (dashed) contours correspond to positive (negative) values and 0 contours are omitted. Unit for the color shading is m^2 s^{-2}. Please refer to the text for the definition of day 0.

3.2.5. *Energetic Processes Contributing To Storm Track Anomalies*

The local HF EKE budget is analyzed with Eq. (3) to identify the key energetic

processes contributing to the composite anomalies of HF EKE in periods I and II (Fig.

3.10). The discussion is focused on the four main conversion terms on the RHS of

(3)—namely, the energy flux convergence (EFC), barotropic conversion (BT), baroclinic

conversion (BC), and the generation of HF EKE due to CFEI. The CFEI term is further

decomposed into HH, HI, HL, and HIL (please refer to the definitions in Chapter 2) to

identify the most important component of the cross-frequency eddy–eddy interaction.

Since energy conversion terms represent only the "tendency" of the local HF EKE, the

composite intraseasonal anomalies of these terms are time shifted and constructed for

periods preceding previously defined periods I and II. Specifically, the energy composites

for period I (II) are averages over day −12 to day +2 (day +10–day +24) and are shown in

Fig. 3.12 (Fig. 3.13). Figures 3.12a–e correspond to the mean HF EKE tendency, EFC,

BT, BC, and CFEI, respectively. The mean HF EKE tendency in Fig. 3.12a has a

distribution very similar to that of the HF EKE anomalies of period I shown in Fig. 3.10a,

which demonstrates that the choice of the averaging period for energy conversion terms is

appropriate. The magnitudes of the anomalies of EFC, BC, and CFEI are comparable,

indicating equally important contributions to the HF EKE tendency by all three processes.

It is also worth noting that the values of the individual conversion terms are typically an

order of magnitude larger than those of the mean HF EKE tendency, implying substantial

cancellations among various conversion terms.
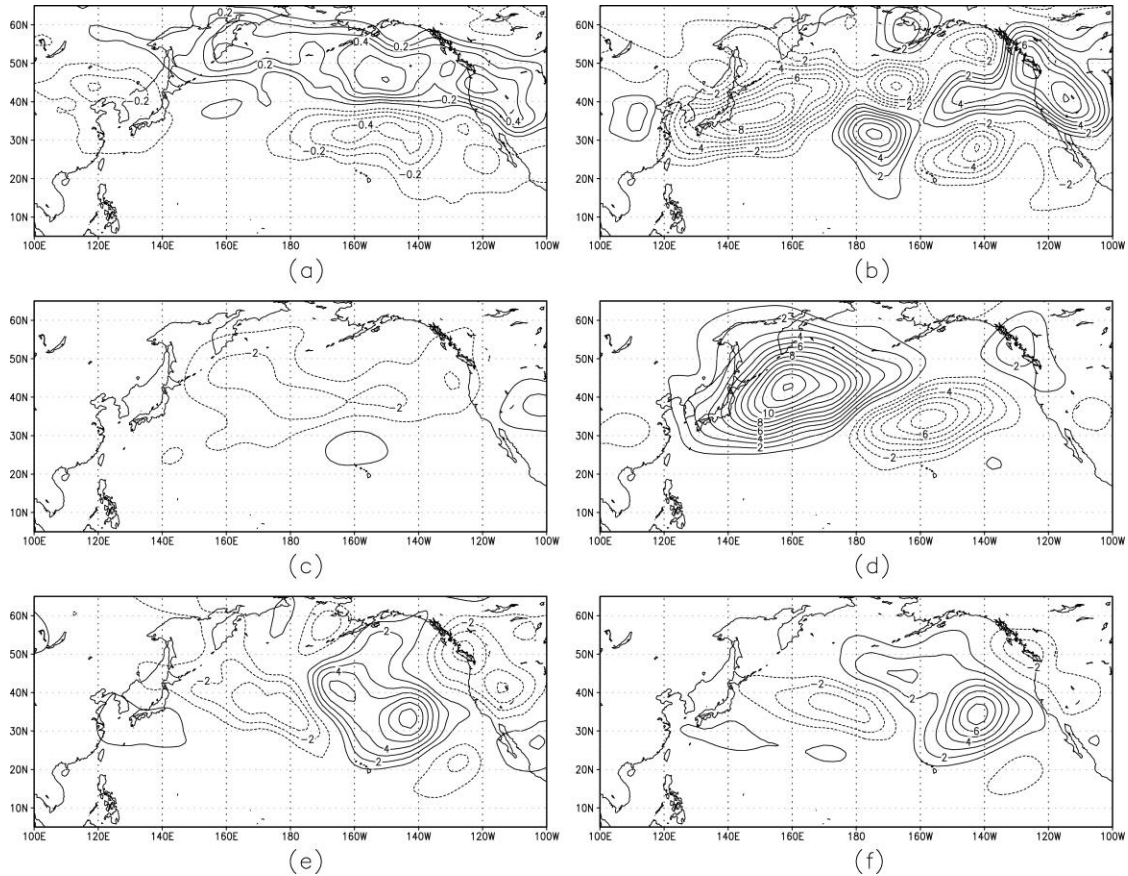
Figure 3.12: Composite intraseasonal anomalies of the (a) SEKE tendency, (b) EFC, (c) BT, (d) BC, (e) CFEI, and (f) HL for the period (day −12 to day +2) relevant to period I SEKE anomalies. Contour interval is 0.1 $m^2 s^{-2} day^{-1}$ for (a) and 1 $m^2 s^{-2} day^{-1}$ for the rest. Solid (dashed) contours correspond to positive (negative) values and 0 contours are omitted. Displayed are values reaching the 95% significance level.

In Fig. 3.12a, an above-normal growth rate of HF EKE is found north of 40°N, extending from the northwestern North Pacific to western North America. This above-normal growth is collectively contributed by positive anomalies of BC over the northwestern North Pacific east of Japan (Fig. 3.12d), positive anomalies of CFEI over the eastern Pacific (Fig. 3.12e), and positive anomalies of EFC over western North America (Fig. 3.12b). The below-normal growth rate of HF EKE over the subtropical eastern Pacific is largely associated with the negative BC anomalies over 180°–130°W

(Fig. 3.12d) with secondary contributions from EFC (around 140°W, 25°N, Fig. 3.12b) and CFEI (around 130°W, 20°N, Fig. 3.12e). The BT anomalies (Fig. 3.12c) are concentrated around 40°N, generally negative, and have smaller amplitudes compared to other conversion terms. They have minor negative (positive) contributions to the HF EKE tendency north (south) of 40°N. After comparing the four components of the eddy–eddy interaction term (i.e., HH, HI, HL, and HIL), we found that the interaction between synoptic eddies and LF dominates the CFEI anomalies seen in Fig. 3.12e. Shown in Fig. 3.12f, the distribution of HL anomalies is approximately characterized by a dipole structure in the zonal direction across the midlatitude North Pacific. It indicates that substantial amounts of HF EKE are generated (lost) through the interaction between the synoptic eddy and intraseasonal eddy component of the flow over the eastern Pacific (western-central Pacific).

The mean HF EKE tendency in Fig. 3.13a is also consistent with the HF EKE anomalies observed during period II (Fig. 3.10b). Similar to the previous period, the below-normal growth rate north of 40°N is contributed by negative BC anomalies (Fig. 3.13d) over the northwestern North Pacific, negative CFEI anomalies over the eastern Pacific (Fig. 3.13e), and negative EFC anomalies over the eastern Pacific–western North America (Fig. 3.13b). The enhanced HF EKE growth south of 40°N is primarily associated with positive BC anomalies over 180°–130°W (Fig. 3.13d) and positive EFC anomalies over 160°–110°W (Fig. 3.13b). The BT anomalies are again weaker compared

to other conversion terms and have minor negative (positive) contributions to the HF EKE tendency north (south) of 40 °N (Fig. 3.13c). During this stage, CFEI (Fig. 3.13e) is also dominated by HL (Fig. 3.13f) with the signs of the zonal dipole reversed compared to the previous stage (Fig. 3.12f). Significant loss of HF EKE due to the interaction between synoptic eddies and intraseasonal flow is now seen over the eastern Pacific.
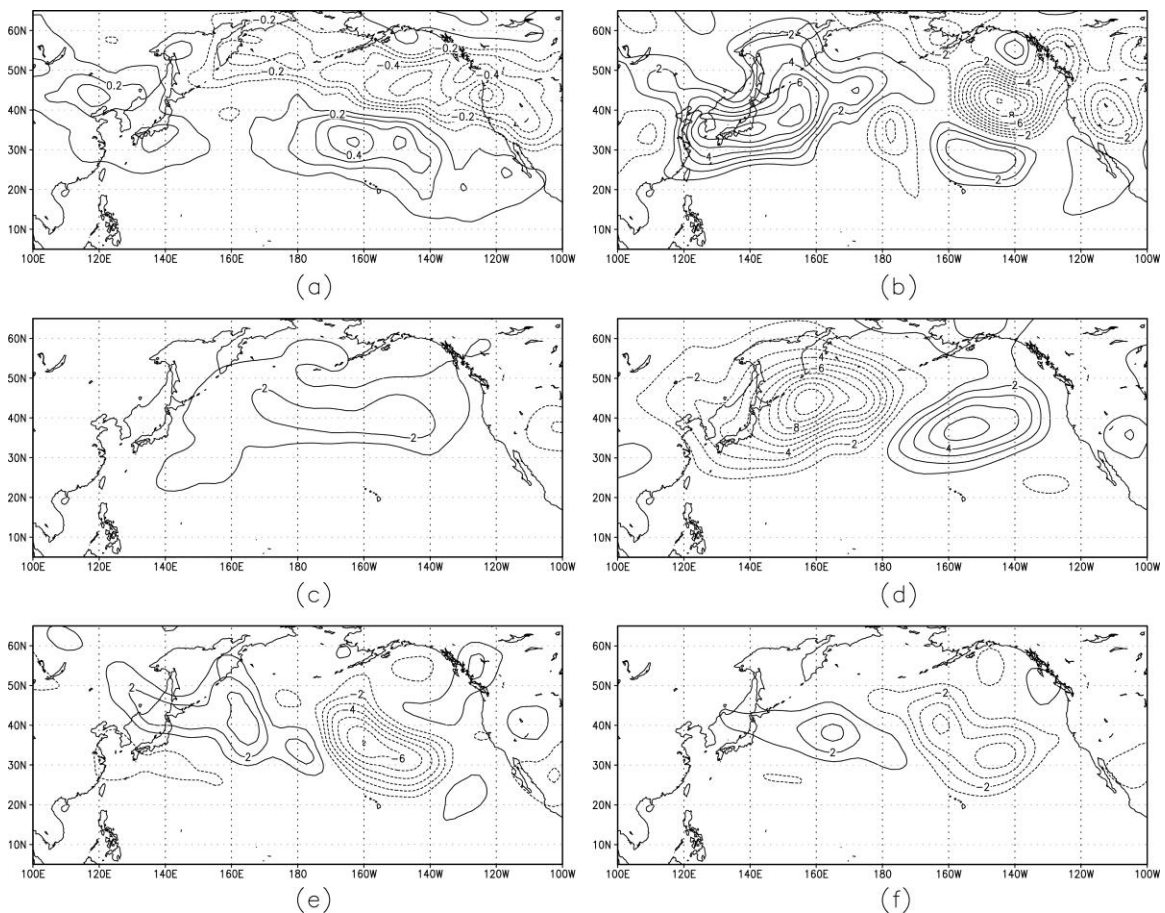
Figure 3.13: As in Fig. 3.12, but for the period (day +10–day +24) relevant to period II HF EKE anomalies.

From Figs. 3.12 and 3.13, we may conclude that the storm-track response to intraseasonal variation in tropical convection is generated through nearly equally

65

important changes in the convergence of energy flux, baroclinic conversion, and HF EKE

generation due to the interaction between synoptic eddies and intraseasonal flow. Both

the magnitudes and signs of these three terms have large spatial variations and also

evolve during the course of a typical MJO event. Among these processes, EFC and CFEI

are, respectively, linked to the properties of a wintertime–mean flow and intraseasonal

flow anomalies that often appear in the form of barotropic Rossby waves forced directly

by anomalous tropical heating [e.g., *Matthews et al.*, 2004]. The significant contribution

of HL to the HF EKE anomalies thus suggests the importance of the "direct" extratropical

response to MJO variability in setting up the storm-track anomalies associated with the

MJO. The HF EKE budget analysis done here serves a first step toward understanding the

rather complicated processes of eddy–mean flow interaction and eddy–eddy interaction

involved in the development of the extratropical response to MJO variability.

3.2.6. Precipitation over Western North America.

Coastal cyclonic activity in winter largely determines the year-to-year fluctuations

of the precipitation characteristics over western U.S. [*Myoung and Deng*, 2009]. Here, as

an initial effort to study the subseasonal, downstream precipitation impact of the Pacific

storm track, we compare the temporal evolutions the intraseasonal anomalies of

precipitation and HF EKE over the eastern North Pacific during the course of a MJO

event. Fig. 3.14a is a time-latitude plot showing the precipitation (contour) and HF EKE

(color shading) anomalies averaged over 160 °W-130 °W (see Section 2 for a definition of day 0). The precipitation signal is characterized by a three-band anomaly ("dry-wet-dry") propagating poleward from day -25 to day 25. The precipitation anomalies are largely in phase with those of HF EKE, i.e., above (below) normal precipitation corresponds to enhanced (suppressed) HF EKE, which is particularly strong after day -10. Due to this non-stationary, three-band precipitation anomaly, the region over the eastern Pacific between 25 °N and 45 °N experiences a transition at day 0 from a dry to a wet regime and each regime lasts approximately 20 days. South of 20 °N, two transitions, dry to wet and wet to dry occur respectively around day -15 and day 5. In Fig. 3.14b, the color shading is replaced with the anomalies of the 2-8 day band-pass filtered OLR variance over the eastern Pacific. Positive (negative) precipitation anomalies are found at regions with enhanced (suppressed) synoptic variability in OLR in the time-latitude space. This further confirms the effect of storm track modulation on the intraseasonal variability of precipitation over the North Pacific near western North America.
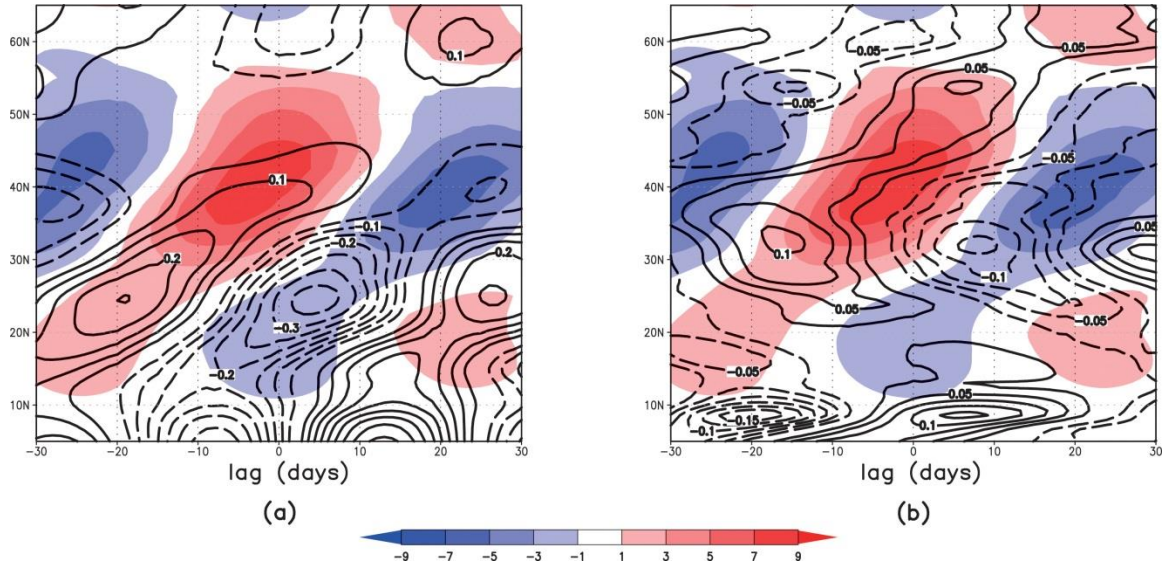
Figure 3.14: (a) Time–latitude plot of the composite intraseasonal anomalies of precipitable water (contours) and SEKE (color shading) averaged over 135 °–120 °W. (b) As in (a), but the contours now correspond to the composite intraseasonal anomalies of precipitation. Contour interval is 0.05 mm in (a) and 0.025 mm day^{-1} in (b). Solid (dashed) contours correspond to positive (negative) values and 0 contours are omitted. Unit for the color shading is m^2 s^{-2}.

3.2.7. Section Conclusions

This diagnostic study examines the response of the Pacific storm track to the intraseasonal variation in tropical convection characteristic of a typical MJO event in boreal winter. A MEOF analysis conducted on the 30–90-day bandpass-filtered tropical OLR and mass-weighted, vertically-averaged HF EKE field reveals a pronounced dipole anomaly of the Pacific storm track propagating northeastward as an OLR couplet moves from the East Indian Ocean to the western-central Pacific. This movement roughly corresponds to the phase 4–phase 6 evolution of MJO according to the multivariate MJO index defined by *Wheeler and Hendon* [2004]. We further divide the development of the

storm-track response into two periods with period I and II corresponding to the days when the center of enhanced tropical convection (largest negative OLR anomalies) is located over the eastern Indian Ocean–Maritime Continent and the equatorial western-central Pacific, respectively. Case compositing for the HF EKE anomalies during these two periods confirms that the storm-track response to the intraseasonal variation in tropical convection can be described as a northeastward-propagating, amplitude-varying dipole anomaly in the HF EKE field. A tripole anomaly pattern in the North Pacific HF EKE field is identified if counting in the weak yet distinct HF EKE anomalies found over the tropical–subtropical central Pacific. During period I, over $140°–170°E$, the anomalous equatorward propagation of transient energy over a subtropical zone $(15°–20°N)$ contributes to a higher level of synoptic variability in the tropical OLR, which projects into the negative, eastward-propagating intraseasonal anomalies of the OLR. This constitutes a positive feedback of storm-track response to MJO-related variability in tropical convection.

A diagnosis of the local HF EKE budget shows that three energy conversion processes (i.e., convergence of energy flux, baroclinic conversion, and generation of HF EKE due to interaction between synoptic eddies and intraseasonal flow) are nearly equally important in terms of contributing to the HF EKE anomalies observed during the two periods. The relative magnitude and spatial distributions of these three conversion terms also evolve during the course of an MJO event. This budget analysis demonstrates

significant roles played by eddy–mean flow interaction and eddy–eddy interaction in the development of the extratropical response to MJO variability. Accompanying the evolution of the tropical OLR, an anticyclonic (cyclonic) circulation anomaly in the upper-tropospheric intraseasonal flow, and to its south, a cyclonic (anticyclonic) circulation anomaly, develops over the North Pacific during period I (period II). The anticyclonic (cyclonic) circulation anomaly found during period I (period II) is part of a Rossby wave train forced primarily by anomalous tropical heating associated with the MJO. The eastern and northern portions of these circulation anomalies, however, are partly maintained by the anomalous synoptic eddy forcing that is quantified in terms of the divergence–convergence of the barotropic E vector. The last part of the analysis is an initial effort to quantify the subseasonal, dynamical control of the Pacific storm tracks on the hydroclimate variability over its downstream region. Associated with the HF EKE anomalies identified here, a three-band (dry–wet–dry) precipitation anomaly forms and propagates poleward over the eastern North Pacific and the coastal region of western North America during the course of an MJO event. The region between $25°$ and $40°$N makes a transition from a wet to a dry regime around day -5 (i.e., when the center of enhanced tropical convection reaches $110°$E), with each regime lasting approximately 25 days. North of $40°$N, two transitions occur at day -10 and day $+15$, respectively. Future research efforts will include a quantification of the predictive skill resulting from the storm-track modulation of the subseasonal hydroclimate variability in western North

America.

Part of the work presented in this chapter are published in Climate Dynamics (Jiang et al.

2013), Journal of Climate [Deng and Jiang, 2010], Journal of Geophysical Research

[Dong et al., 2011]

CHAPTER 4

ATMOSPHERIC RIVERS AND INTERMEDIATE FREQUENCY

DISTURBANCES: LINKAGE BETWEEN WEATHER EXTREMES

4.1 A Newly Developed AR Detection Algorithm

The methods to detect AR can be categorized into different groups, depending on whether they use AR characteristics, atmospheric variables or coordinate frameworks for identification. For example, Lagrangian framework [e.g., *Bao et al.*, 2006; *Dirmeyer and Brubaker*, 2007; *Gimeno et al.*, 2010; *Knippertz and Wernli*, 2010; *Stohl and James*, 2005] versus Eulerian framework [e.g., *Guan et al.*, 2011; *Lavers et al.*, 2011; *Neiman et al.*, 2008b]; Integrated Water Vapor (IWV) based algorithm [e.g., *Neiman et al.*, 2008b] versus moisture flux based algorithm [e.g., *Zhu and Newell*, 1998]; extreme event oriented identification [*Byna et al.*, 2011] versus spatial structure oriented identification [e.g., *Jiang and Deng*, 2011; *Lavers et al.*, 2012; *Wick et al.*, 2012]. Based on an AR-like structure detection algorithm they developed, *Jiang and Deng* [2011] propose an idea of "AR probability" which quantifies the AR activity with respect to the odds of its occurrence. Using this, they construct the first AR activity climatology over North Pacific.

Presently, we develop a new algorithm for AR-like structure detection based on IWV; the step by step procedures are presented as follows:

1) The IWV value at any grid point (Qr) is retained if only it satisfies

$$Q_r \geq Q_{zmean} + A \bullet (Q_{z\max} - Q_{zmean}), \text{ and}$$

$$Q_r \geq Q_{mmean} + B \bullet (Q_{m\max} - Q_{mmean}). \tag{7}$$

whereby, Q_{zmean} denotes the zonal mean IWV along the same latitude of the grid point under consideration and Q_{zmax} is the maximum value of IWV found along that latitude. Similarly, Q_{mmean} denotes the meridional average of IWV between $0°$ and $90°N$ along the longitude of the grid point and Q_{mmax} is the maximum value of IWV found along that longitude between $0°$ and $90°N$. Parameters A and B are assigned to 0.3 and 0.1 respectively; however, these two values are arbitrary and adjustable to best capture the filamentary structure of AR.

2) The criterion of IWV > 20 mm is applied to the result from step 1, meanwhile, the southernmost boundary is set to 15 °N.

3) A "connected components labeling" algorithm [*Liu et al.*, 2008] is used to filter out smaller scale structures; AR with a total area smaller than 2.5×10^5 km^2 are screened out from the daily map.

4) Estimate the general shape of selected region by putting a minimum sized rectangle box and estimate the fraction it occupies. If the fraction is less than 3/4 (so it is elongated, and the ratio of length to width is less than 2:1), then the labeled pattern can be retained.

5) Next, the orientation of the selected pattern is measured by regressing the latitudes onto the longitudes, and screening out all patterns where the overall orientation is not

northeast (0 degree ~ 90 degree from the east).

6) Finally, all the retained regions are flagged as 1, else, the flag is set to 0.

Based on this more sophisticated AR detection algorithm, the climatology of AR probability is constructed and shown in Figure 4.1 for reanalysis data (Fig. 4.1b) and T85 (Fig. 4.1a) and T341 (Fig. 4.1c) resolution simulation output. Over the west coast of the U.S., the AR occurrence probability from the MERRA data is about 10%, which is in good agreement with a previous study [*Dettinger et al.*, 2011]. Clearly, both medium (T85, Fig. 4.1a) and high (T341, Fig. 4.1c) resolution simulations reproduce the AR distribution well over the west coast compared with MERRA. We can estimate the ratio of AR induced extreme precipitation by matching the AR-like structure and extreme precipitation (99th percentile) on daily map along a dilated west coast belt. The distribution from MERRA data (Fig. 4.1e) shows that the coastal region between 38°N and 50°N is more likely affected by AR events, because over 70% of the extreme precipitation events are AR-related. Whereas, applied the same algorithm to the two simulations, the high resolution simulation (T341) correctly captures the spatial distribution and much of the magnitude (Fig. 4.1f), but the pattern with the medium resolution shows an obvious southern bias, with the maximum value located around 35°N (Fig. 4.1d).
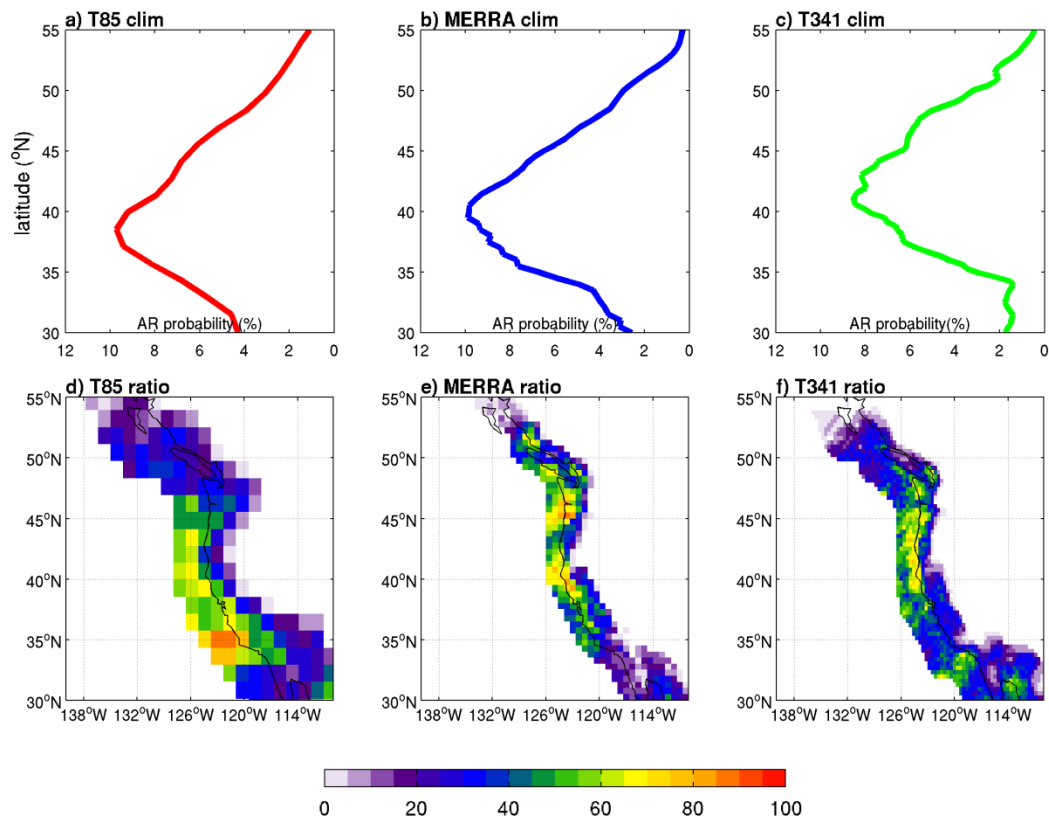
Figure 4.1: AR activity over the west coast U.S. winter season (December − January). Climatology of the AR activity probability derived from (a) T85 simulation; (b) MERRA reanalysis data; (c) T341 simulation. The ratio of AR induced extreme precipitation (99th percentile) is also shown for (d) in T85 simulation; (e) MERRA reanalysis data; (f) T341 simulation. (Unit: percentage).

4.2 An Attempt Towards An Objective AR Detection: The Complexity And Challenge

As introduced in Section 4.1, AR events can be identified and measure through several approaches. Among them, algorithms that use IWV field are better accepted by the community, because it is essentially how we are aware of the event from the satellite image or other dataset; meanwhile, the wind profile information is not always available especially

in satellite data.

From technical aspect, most of the algorithms [e.g., *Neiman et al.*, 2008a] used by now are based on the thresholds described in *Ralph et al.* [2004, total water vapor > 20mm; length > 2000km; width < 1000km]. These algorithms can roughly detect the occurrence of the events that made landfall (IWV> 20mm and AR must reach the continent), which, make the result subjective to some criteria beside the feature of AR itself. In *Byna et al.* [2011], they develop a new approach not only by the amplitude and landfall of IWV, but also employ a "connected component labeling method" [*Liu et al.*, 2008，based on binary pixels connectivity] to screen the horizontal shape of areas which the IWV exceed 20mm and use this to decide the occurrence of event.

It is worth emphasizing the term "event", because AR events are observed only when they have already made significant influence over certain regions (western North America / Western Europe). However, most of the algorithms can't provide information on what the phenomenon "looks like", such as position, length, width and source region, which are used to describe the AR in almost all the studies; moreover, on the developing stage of AR, monitoring the AR-like pattern is crucial for the predictability and preparation of extreme events in coastal regions.

The task ongoing tries to find out an objective way to detect and quantify AR-like pattern by its own characteristics. The finding will help us identify the main axis, the width and tropical origin of AR.
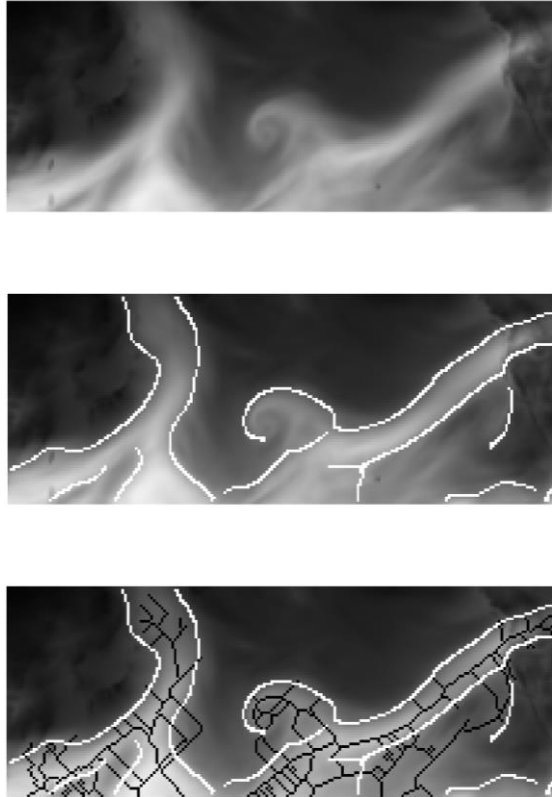
Figure 4.2: An attempt on an objective detection of AR pattern. On top panel, the IWV field (date: November 7th 2006) is transformed into a grayscale image (the brighter the color, the higher the amplitude); in the middle panel, the edge (white color) of potential AR pattern is detected and overlaid on top of the grayscale image; in the bottom panel, the skeleton of the AR is plotted (black lines).

Some initial result is shown in Figure 4.2. In this image, the AR edge is defined

primarily based on its gradient; and its skeleton is identified by tracking the local maxima

on the grayscale map. The detections of AR edge and axis are processed independently

through the standard image processing approaches, but if we can combine these two

results, we can objectively identify not only the length and position (by the information

from the black axis) of AR, but also the width (by the information from the white edge)

and affected area.

77

However, there are two big challenges in achieving the purpose. The first challenge is how to get rid of the side branches from the main axis (which has a generally southwest-northeast orientation and large IWV amplitude); and the second issue need to be addressed is how to automatically associate the edge with the existing axis.

For the first challenge, the axis can be treated as a "graph traversal" problem, since every identified axis pixel are potentially connected to 1 (leaf), 2(normal axis point) or 3 (node) pixels. Therefore, the work left for the "axis" part is to find a way to optimize this "graph traversal" problem to best capture the orientation, the origin, the length and the intensity of AR from daily map. The second problem can be optional, because in some sense, the width of AR can be arbitrary decided by the amplitude of IWV or use constant width threshold to identify the affected region on the map. In any case, if we can combine the edge information, the detection of AR-like pattern would be more objective and accurate.

4.3 Downstream Modulation of the AR by EACS: Observation and Simulation

4.3.1. Motivation

East Asia Cold Surge (EACS) is one of the most efficient mechanisms in Earth's climate system through exchange of the kinetic and potential energy between high latitudes and mid-low latitudes. The accompanying hazardous weather phenomena, such as

snowstorms and freezing rain, bring tremendous social and economic impacts over East

Asian countries, including the second and third largest economies [*Chang*, 2004].

Associated with strong northwesterly winds that originate from Lake Baikal, EACS

sweep across East Asia and cause steeply rising surface pressure and sharply lowering of

the surface temperature [*Wang*, 2005]. Once these cold and dry airmasses approach the east

coast and encounter the warm and moist airmasses over the East China Sea and Sea of

Japan, atmospheric disturbances brought about by this strong contrast are strengthened

immediately in this region [*Kung and Chan*, 1981]. Studies on the initiation of EACS, as

well as their interaction with tropical-extratropical planetary-scale circulations such as jet

stream, Hadley Circulation, Walker Circulation [e.g., *Chang and Lau*, 1980; *C-P Chang*

and Lau, 1982] and ENSO [*Chen et al.*, 2004] reveal that the conspicuous role of synoptic

scale features within surge event. By using 11 individual EACS events in winter 1978/79,

Lau and Lau [1984] constructed the composite synoptic charts and illustrate that the HF

disturbances and LF disturbances are distinguished with respect to their three-dimensional

structure and energetics: accompanying the cold surges, the HF disturbances are organized

in the form of extratropical cyclone and migrate along the northwest boundary of North

Pacific from East Asia to the Gulf of Alaska, while the LF disturbances propagate

equatorward and its shape elongated zonally. In a survey of various phenomena associated

with East Asian monsoon (EACS) given by *Lau and Li* [1984], it is suggested that the

disturbances brought about by the EACS may further profoundly influence other

downstream circulation regimes by the collaboration of tropical and midlatitudes systems.

Because the plume-like structure of AR is so thin (~400 km) and long (>1000 km), it is important to be aware that the spatial resolution is a vital factor in identifying the phenomenon from either the long term climatology dataset or in simulating its feature from Global climate model (GCM). For example, with a grid spacing of about 1.3 degrees (e.g. T85 spectral), the width of AR is barely resolved by 3 grid points; whereas models with grid spacing of about 1/3 degrees can resolve AR with 13 grid points across. Therefore, 1/3 degrees enables the event location to be captured more accurately, and also the gradient and plume features are resolved more precisely.

Due to the span of influence across the Earth, GCM simulations are the optimal experimental framework to examine AR and their variability under various conditions. However, it has not been tractable to generate long global climate simulations at a spatial resolution adequate to resolve the AR until recently. In addition, large-scale dynamical effects that are captured with the coarser models can potentially be better represented at the finer spatial scale. There is evidence that increasing the horizontal resolution of global atmosphere models provides improved simulation of smaller scale features, such as precipitation [*Li et al.*, 2011; *Wehner et al.*, 2010] and tropical cyclones [*Wehner et al.*, 2010]. But analyzing the link between global and sub-global features in a GCM is not well documented yet because the necessary spatial resolution is only recently available.

Using a combination of high resolution reanalysis data and GCM simulations in

different resolutions, we will 1) establish causality between EACS and western U.S. precipitation using observationally based MERRA data and; 2) perform a similar analysis with medium and high resolution GCMs. This will enable an evaluation of the model performance, quantify the advantage of high resolution models in understanding scale interactions among different disturbances, and motivate more detailed investigation of the downstream modulation in future scenario runs. Section 4.4.2 will introduce the dataset and GCM and a revised AR detection algorithm and other general analysis methods are also discussed. Section 4.4.3 will present the response of AR and coastal precipitation following the EACS in both the observation and model. Section 4.3.4 will show the associated large scale circulation from both the observation and simulations over the same time period. Section 4.3.5 diagnoses the mechanism behind the scale interaction by partitioning the height tendency equation; and section 4.3.6 will discuss the relative importance of disturbances at different timescales. Section 4.4 will summarize the results.

4.3.2. *Data, Model and Methods*

This study uses the NASA Modern Era Retrospective-Analysis for Research and Applications (MERRA) dataset, which assimilates a number of state of the art water cycle products from satellite observation. The surface air temperature (SAT), integrated water vapor (IWV), geopotential height, specific humidity and horizontal wind fields for 1979-2005 are retrieved from this high quality reanalysis data with a native spatial

resolution of $1/2^o$ latitude by $2/3^o$ longitude and 72 hybrid levels [*Rienecker et al.*, 2011].

Because of its fine resolution, the IWV product from MERRA has served as the date source

for AR detection and analysis in Section 4.1 already.

Model simulations are conducted with the NCAR Community Climate System Model

version 4 (CCSM4) [*Gent et al.*, 2011]. CCSM4 as configured for this study is comprised

of an active global spectral atmosphere model (CAM4) for two different horizontal

resolutions T85 and T341,which correspond to approximately $1.4\,°$ and $0.3\,°$ grid spacing,

respectively. The Community Land Model (CLM4) is the active land model coupled to

CAM4 and is configured with a grid of $0.9\,°$ latitude by $1.25\,°$ longitude. The sea-ice model

uses climatological sea-ice coverage and the ocean model is represented with

climatological, monthly-averaged sea surface temperatures [*Rayner et al.*, 2006]. More

details of the model configuration can be found in *Evans et al.* [2013]. Both the T85 and

T341 model configurations were initialized with land datasets spun up from a previous

CCSM4 production run using the FV dycore of comparable resolution [*Evans et al.,* 2013].

To initialize the atmosphere, outputs from a comparable preindustrial configuration were

used.

To identify the large scale extreme EACS events, a daily index for winter time

(October-March) is constructed with averaged SAT over East Asia (100 °E–130 °E, 20 °N–

40 °N, Figure 4.3a). Then, a 30-day highpass filter is applied to this index. Two criteria are

used to identify the extreme events: 1) local minima of the index must less than -3 standard

deviation, 2) and successive events must be at least 5 days apart. [based on the typical EACS frequency; *Zhang et al.*, 1997] The identified local minimum represents the peak of each EACS event and are labeled "day 0" in the following analysis. Applied to MERRA, 35 extreme events are identified, and they are in good agreement with the EACS events identified by *Park et al.* [2011] through a different definition. The mean feature of the SAT at the peak (day 0) of EACS is shown in Figure 4.3.
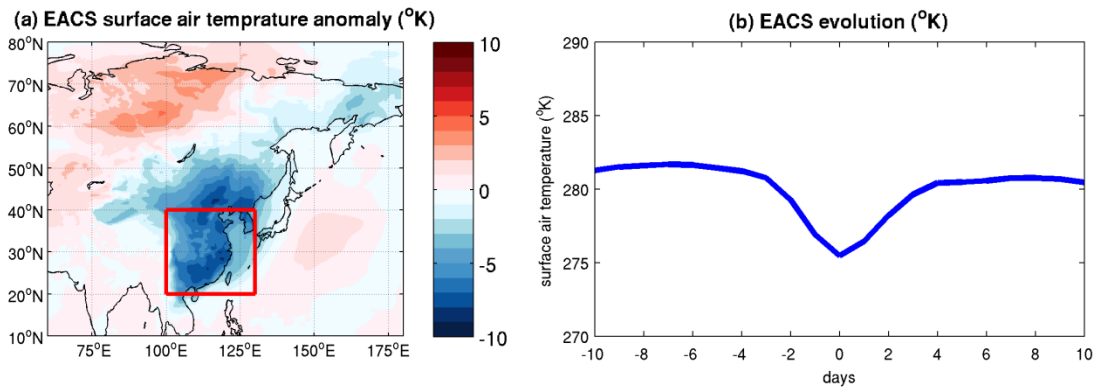
Figure 4.3: Mean surface air temperature feature of East Asia cold surge in MERRA data. (a) Distribution of SAT anomaly on the peak of EACS (day 0); (b) SAT time series averaged over the red box as indicated in (a) from day -10 to day 10. (Unit: K)

Finally, a Lanczos filter [*Duchon*, 1979] with 203 weights is used throughout this study to isolate fluctuation in different timescales. The choice of 203 weights guarantees the tradeoff between Gibbs phenomenon and the sharpness of stop-band. Standard daily composite analysis is employed to reveal the downstream impact of EACS on the North Pacific atmospheric circulation and moisture transport. The significance levels throughout the study were obtained through a non-parametric approach (i.e., Monte Carlo sampling).

4.3.3. The Response of AR Probability And Coastal Precipitation To EACS Events

Using the detection algorithm to identify AR in MERRA, T85 and T341 simulation data, the day-to-day evolution of coastal AR probability following the extreme EACS event is shown in the left column of Figure 4.4 (Fig. 4.4a, c, e) respectively. Based on the results from MERRA (Fig. 4.4c), immediately after the peak of EACS event (day 0), the North Pacific AR activity is less likely observed over the West coast of the U.S. north of 35^oN. From day 2 to day 8, however, the activity of AR is enhanced significantly, and the positive anomaly peaks on day 5 in the coastal band between 35^oN and 45^oN, region which is the most vulnerable to AR-induced extreme precipitation. It is important to point out that although the amplitude only exceeds 5% in either phase, the whole evolution indicates a roughly 100% phase transition relative to its climatology. The anomalous AR activity also projects onto the precipitation anomaly (Fig. 4.4d), changing from a suppressed to enhanced phase as well as southward propagation along the coast region following the EACS. About 7 to 9 days after the peak of the EACS event, the North California coast experiences more than 2.5 mm above normal precipitation on average in the MERRA data.
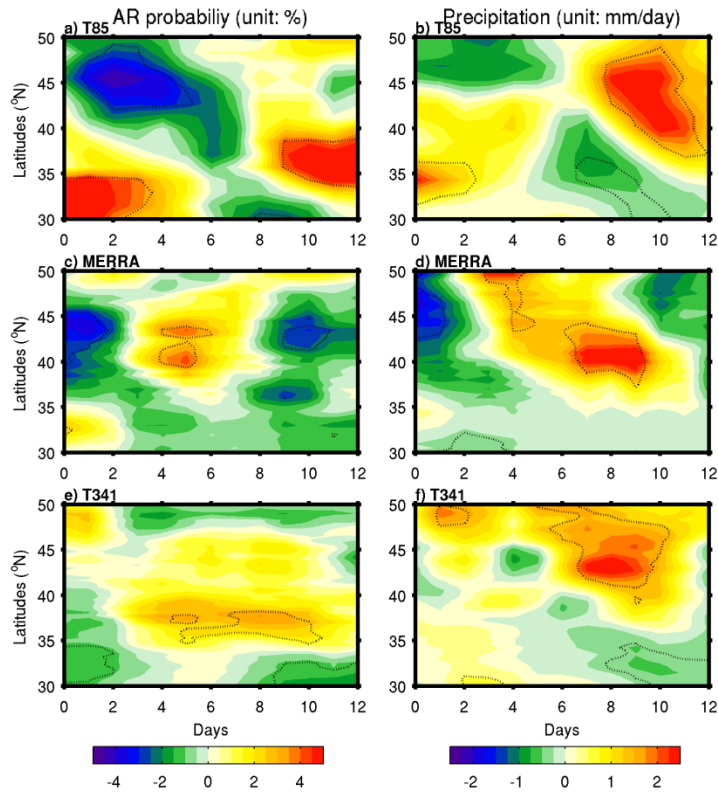
Figure 4.4: Composite response of AR activity probability (left) and precipitation (right) over the west coast of the U.S. to the EACS events. Dashed contours indicate 90% significance level. Left column: AR probability (unit: %); right column: precipitation (unit: mm/day). Both columns show T85, MERRA and T341 from top to bottom.

In the medium-resolution simulation (T85) data, the most prominent feature is the significantly southward shift of the AR activity (Fig. 4.4a) immediately after the peak of EACS, the north-south dipoles pattern maintains up to day 6. In the following 2 days, AR activity over the West coast U.S. is suppressed entirely. From day 8, the ARs become very active with a maximum increase of more than 5%. Associated with the distinct AR evolution, the precipitation anomaly (Fig. 4.4b) also exhibits a north-south dipole feature and the sign was reversed on day 6.

The high-resolution simulation (T341, Fig. 4.4e) exhibits development more similar

to the observationally derived data. The AR probability anomaly increases 2 days after the peak (day 0) of the EACS event and the West coast area of California between 35°N and 45°N experiences by enhanced AR activity for more than 10 days (beyond day 12). With T341, the associated precipitation anomaly (Fig. 4.4f) is above than normal from day 7 to day 9 over the coastal region as with MERRA. Overall, the downstream responses of AR activity and coastal precipitation suggest good agreement between MERRA and T341 simulation; whereas, these features are missed in the T85 simulation.

4.3.4. The large-scale circulation following the EACS

To understand the inconsistency between simulations with different resolutions depicted in Section 4.3.3, it is instructive to construct and examine the flow and moisture transport in the troposphere over the same time period. The panels in Figure 4.5 show the height anomaly (color shading) in the mid-troposphere, overlain by the moisture transport anomaly (arrows) in the lower troposphere over the North Pacific following the peak of EACS based on MERRA data. Immediately after the EACS approaches its mature stage (Fig. 4.5b), an intense trough is brought about over Sea of Japan with height change of more than 160 m. At the same time, an anticyclonic height anomaly is to the East but the peak amplitude is only about half of its cyclonic counterpart. After that, the cyclonic pattern migrates northeastward along the coast of the Eurasian continent (Fig. 4.5e) and approaches the Gulf of Alaska on day 4 (Fig. 4.5h). Then, the movement of this height

anomaly branch slows and is locally enhanced over eastern North Pacific (Fig. 4.5k).
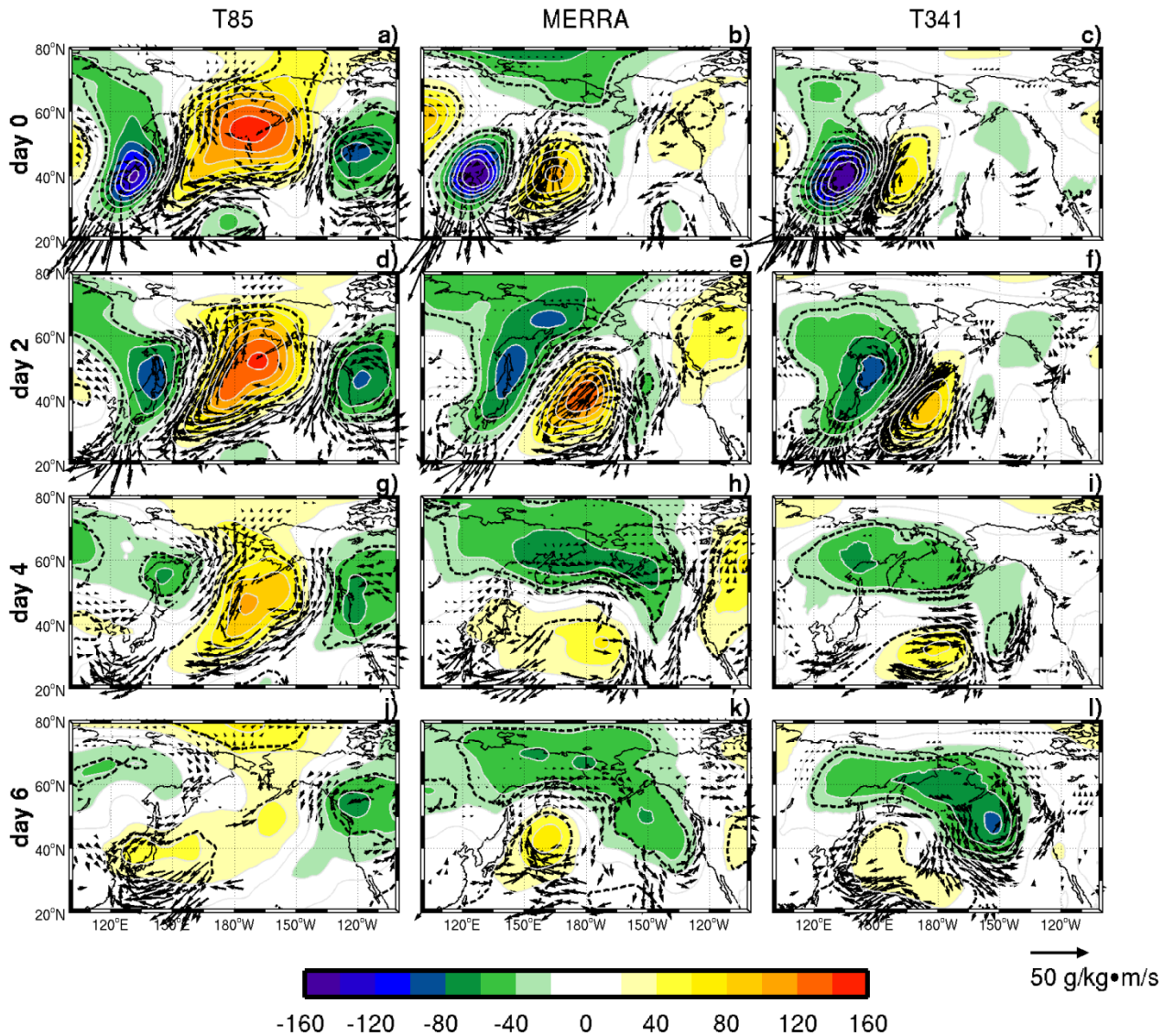
Figure 4.5: Composite of the 500 hPa geopotential height anomaly (color shading, unit: meter) and water vapor transport anomaly (vector) at 850 hPa following the peak (day 0) of EACS events. Dashed contours indicate the height anomaly exceeds 90% significance level and vectors plotted on the map indicate at least one component of the moisture flux exceeds 90% significance level. Results from T85 simulation are presented on the left column; the middle column is for the MERRA reanalysis data; the right column is for the T341 simulation. From top to bottom are result from day 0 (peak of EACS events) to day 6, plotted every 2 days.

A composite of the water vapor transport anomaly in the MERRA data is also shown

on the middle column of Figure 4.5. When the EACS approaches its peak amplitude (Fig.

4.5b), on day 0, a significant amount of water vapor is pumped from the western Pacific

northward and brings about significant weather affecting the Japan and Korean peninsula.

Over the central North Pacific, the moisture flux anomaly illustrates suppressed poleward

water vapor transport in this region; meanwhile there is only scattered moisture flux

anomaly activity over the eastern North Pacific. 2 days later (Fig. 4.5e), the pattern of the

moisture flux anomaly moves eastward slightly. At the same time, some of the poleward

moisture transport anomaly starts to appear over eastern North Pacific. After 4 days from

the peak of EACS (Fig. 4.5h), anomalous water vapor transport over most of the North

Pacific basin exhibits southward progression. However, the most prominent feature is the

significant north-eastward anomalous flux of moisture, which represents a well-defined

narrow moisture corridor that transports the water vapor from subtropical (and possibly

tropical) eastern Pacific to the west coast of the U.S. in the midlatitudes. On day 6 (Fig.

4.5k), the water vapor flux anomaly becomes less organized, although a significant

moisture band still extends from 30°N to 50°N poleward in this region. Combining the

development of the flow anomaly with the evolution of the AR probability as well as

precipitation reveals that the AR and precipitation over west coast of U.S. in this case are

primarily determined by the large scale circulation anomaly.

The height and water vapor flux anomaly composite of T85 and T341 simulations are

also presented in Figure 4.5. The height anomaly as well as the moisture flux are both stimulated immediately after the peak (day 0) of EACS (Fig. 4.5a, c) in the western North Pacific sector, although the strength of the trough-ridge pattern is less intense in T85 simulation, as is the moisture flux anomaly. On day 2 (Fig. 4.5d, f), the big cyclone in both simulations exhibit slower than observed, nonetheless, north-eastward migration, although T85 is slower than T341. The peak responses for both T85 and T341 on day 0 are situated in the same location. On day 4 (Fig. 4.5g, i), the cyclonic circulation patterns between T85 and T341 are distinct; in the medium resolution version (T85), the migration slows down over the Sea of Okhotsk and weakens at the same time; whereas, in the high resolution simulation (T341), the negative anomaly extends to the Gulf of Alaska, but the amplitude is still smaller than observational (MERRA) data. With respect to the water vapor transport anomaly on day 4, the T85 simulation exhibits poleward transport west of date line, but equatorward anomaly over eastern North Pacific. In other words, the T85 doesn't capture the water vapor transport feature over eastern North Pacific; whereas, the T341 simulation depicts eastward water vapor transport over North Pacific, and roughly reproduces northeastward moisture flux anomaly in eastern portion of North Pacific. After about 6 days, the height and moisture flux anomalies in T85 (Fig. 4.5j) are completely different from observations, the cyclonic pattern recesses to Siberia, and the pre-existing negative height anomaly over western North America is also weakened simultaneously. Because of the distinct circulation pattern in T85, there is no significant land to sea transport in the

Gulf of Alaska region. In the T341 simulation, on day 6 (Fig. 4.5l), the prominent feature is the trough structure over eastern North Pacific. Associated with this, the northeastward transport of water vapor is also enhanced. Note that the negative height anomaly in T341 is slightly removed from the west coast of the U. S., so a large portion of the moisture transport is retained over the ocean. However, this trough moves gradually beyond day 6, and can be observed even on day 10 (not shown), which partly explains the prolonged AR anomaly in T341 simulation (Fig. 4.4e).

4.3.5.   *Dynamical Processes Underlie the Downstream Development*

The downstream modulation by EACS not only strongly determines the atmospheric circulation over western North Pacific, but it also significantly alters the flow pattern off the west coast of North America. This impact determines the activity of AR in this region and further transforms into significant inland precipitation. *Jiang and Deng* [2011] suggest that the trough structure over eastern North Pacific is primarily represented by IF and LF fluctuations based on a spatial projection analysis. However, this does not address what and how the dynamical processes evolve and produce this large scale anomaly.The quasi-geostrophic height tendency equation is employed to examine the dynamical processes that make up the event. Following *Nakamura et al.* [1997], in the upper troposphere, it is governed by the barotropical processes as follows,

$$\frac{\partial Z}{\partial t} \simeq \frac{f_o}{g}\nabla^{-2}\left[-\nabla\bullet(\vec{V}\zeta)-\beta v\right]$$

(7)

here, Z is geopotential height, f_o is the Coriolis parameter at 43^oN ($= 1\times10^{-4}$s^{-1}); g is the acceleration of gravity; $\vec{V}$ is the horizontal wind; ζ is the relative vorticity; β is the variation of the Coriolis parameter with latitude; and v is meridional wind.

The wind components and vorticity on 200 hPa are further partitioned into 4 timescales, namely, high frequency (HF, 2-8 days), intermediate frequency (IF, 8-30 days), low frequency (LF, 30-90 days) and seasonal mean (M). Therefore, the height tendency equation can be expanded to separate the dynamical scales be

$$\frac{\partial Z}{\partial t} = \frac{f_o}{g}\nabla^{-2}[\underbrace{-\nabla\bullet(\vec{V}_H\zeta_H)}_{HH}\underbrace{-\nabla\bullet(\vec{V}_I\zeta_I)}_{II}\underbrace{-\nabla\bullet(\vec{V}_L\zeta_L)}_{LL}-\underbrace{\nabla\bullet(\vec{V}_M\zeta_M)}_{MM}$$
$$\underbrace{-\nabla\bullet(\vec{V}_H\zeta_I+\vec{V}_I\zeta_H)}_{HI}\underbrace{-\nabla\bullet(\vec{V}_H\zeta_L+\vec{V}_L\zeta_H)}_{HL}\underbrace{-\nabla\bullet(\vec{V}_I\zeta_L+\vec{V}_L\zeta_I)}_{IL}$$
$$\underbrace{-\nabla\bullet(\vec{V}_H\zeta_M+\vec{V}_M\zeta_H)}_{HM}\underbrace{-\nabla\bullet(\vec{V}_I\zeta_M+\vec{V}_M\zeta_I)}_{IM}\underbrace{-\nabla\bullet(\vec{V}_L\zeta_M+\vec{V}_M\zeta_L)}_{LM}\underbrace{-\beta v}_{\text{planetary vorticity advection}}]$$

(8)

the H, I, L, M denote HF, IF, LF and mean flow components respectively.

On the right hand side (RHS), the first 4 terms (HH, II, LL, MM) represent the forcing by vorticity flux in different timescales, the following 3 terms (HI, HL, IL) indicate the forcing by vorticity fluxes through cross frequency interaction, the next 3 terms (HM, IM, LM) are forcing associated with eddy-mean flow interaction, and the last term is the forcing of planetary vorticity flux, which is kept in its original form as background forcing. Because the height tendency represents the average rate of height change, we present only the results on day 1, day 3 and day 5 following the peak of EACS.

Shown in Figure 4.6 is the height tendency associated with nonlinear interaction within IF disturbances (II). Clearly, the primary role of II term is to deepen and expand the large scale polar vortex in the upper troposphere following the EACS, as depicted in MERRA data (middle column). On day 1 (Fig. 4.6b), this process produces negative height anomaly north of 45^oN with an amplitude exceeding 3 meter /day in most regions. 2 days later (Day 3, Fig. 4.6e), the influence of this term grows and expands southward. It clearly splits zonally into 2 branches with a northwest-southeast tilt of its southern component extending from East Asia to the west coast of North America. On day 5 (Fig. 4.6h), the center of action moves eastward, although the strength of this forcing is weakened as compared to day 3. Nonetheless, its distribution still positively contributes to the height anomaly over eastern North Pacific.
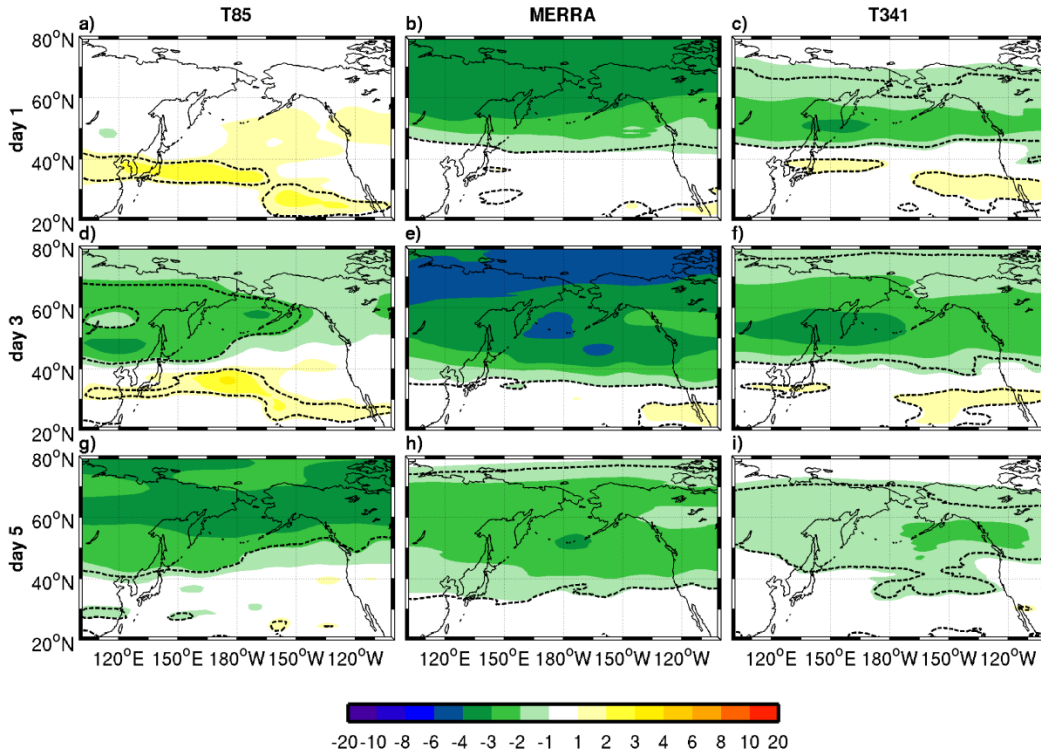
Figure 4.6: Composite of the height tendency (unit: meter/day) forced by the interaction of IF eddies (II) after the peak of EACS events on "Day 1" (top row), "Day 3" (center row), "Day 5" (bottom row). Results are from MERRA reanalysis (Middle column), T85 simulation (Left column) and T341 simulation (Right column). Dashed lines indicate 90% significance level.

The response of the II term in the two simulations is also shown in Figure 4.6. The medium resolution simulation (T85) fails to capture the evolution of this process in several aspects. First of all, the general deepening effect in the mid-high latitudes is missing on day 1 (Fig. 4.6a). Secondly, on day 3 (Fig. 4.6d), it produces some significant trough-like effect west of dateline. Moreover, although the significant negative anomaly extends to North America, its influence is limited to the high latitudes and the pattern depicts a southwest-northeast tilt (Fig. 4.6g).

In the T341 simulation, the II forcing brings about a negative anomaly between 45°N

and 70°N on day 1 (Fig. 4.6c); this negative anomaly is enhanced significantly on day 3 (Fig. 5f), which is similar to the southern branch in the observed height field, but the amplitude is slightly smaller than observed. The eastward movement of the trough-like tendency in MERRA data is also found in T341; on day 5 (Fig. 4.6i), the action center is across from Gulf of Alaska to western North American continent which enhances the off coast trough over eastern North Pacific.
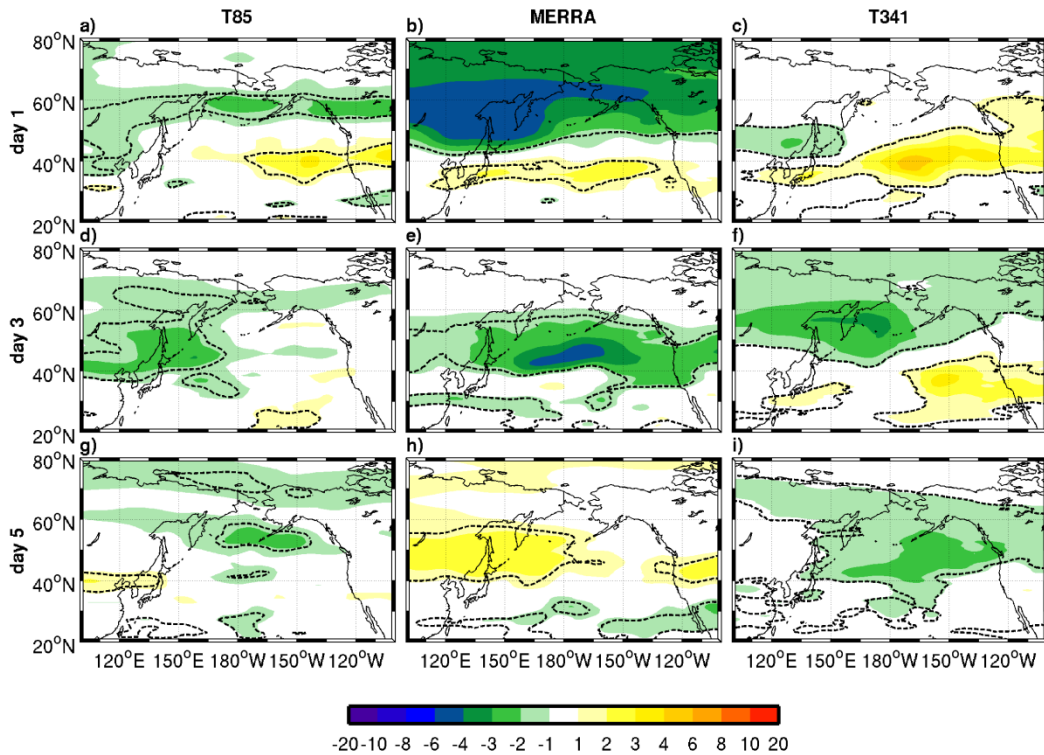
Figure 4.7: Same as Fig. 4.6 but for height tendency forced by the interaction between HF and IF eddies (HI).

The height field forced by voriticity flux associated with HF and IF interaction (HI) is shown in Figure 4.7. In the observational data, following the EACS, the HI term produces a strong cyclonic type height tendency (< -4 m/day) northeastward of the trough pattern over

East Asia on day 1 (Fig. 4.7b), that fuels the migration of the big cyclonic circulation in this region; on day 3 (Fig. 4.7e), the region influenced by the HI term is east of the dateline with its maximum more close to North America. On day 5 (Fig. 4.7c), the negative height anomaly disappears, meanwhile, significant positive height anomaly occupies western North Pacific in the midlatitudes.

Both of simulations fail to fully capture the features associated with this cross-frequency interaction. Specifically, on day 1, T85 only exhibits a significant signal between 50°N and 60°N associated with HI term (Fig. 4.7a); while with the T341, this term shows a significant, though weak, local enhancement (-2 m/day) of the trough structure over Sea of Japan (Fig. 4.7c). 3 days after the peak of EACS, the T85 simulation starts to show some negative height tendency over eastern coast of Eurasian continent (Fig. 4.7d). Whereas, the height tendency in T341 version exhibits northeastward shift as well as a significant enhancement (Fig. 4.7f), which has some correspondence to the observed pattern during day 1. Both simulations indicate the forcing of HI term exerts positive impact to the development of the cyclonic circulation over eastern North Pacific 5 days after the peak of EACS (Fig. 4.7g, i) which is not seen in the observation.

The third term presented here is the forcing induced by the interaction between HF eddy and mean flow (HM). A well-defined wave train is found over North Pacific Basin after the peak of EACS and propagates toward the central-eastern Pacific (Fig. 4.8b), and consistent development of this wave train pattern can be observed on day 3 (Fig. 4.8e) and

day 5 (Fig. 4.8h), with considerable meridional elongation. The strength of the forcing is also intensified in the downstream region up to day 5 (~8 m/day), but it decays quickly after that (not shown). The overall effect of the HM term in the midlatitudes is to advect the HF eddies to the east of the dateline and help the expansion of the negative height anomaly on day 6 (Fig. 4.8k) south of the Bering Strait.
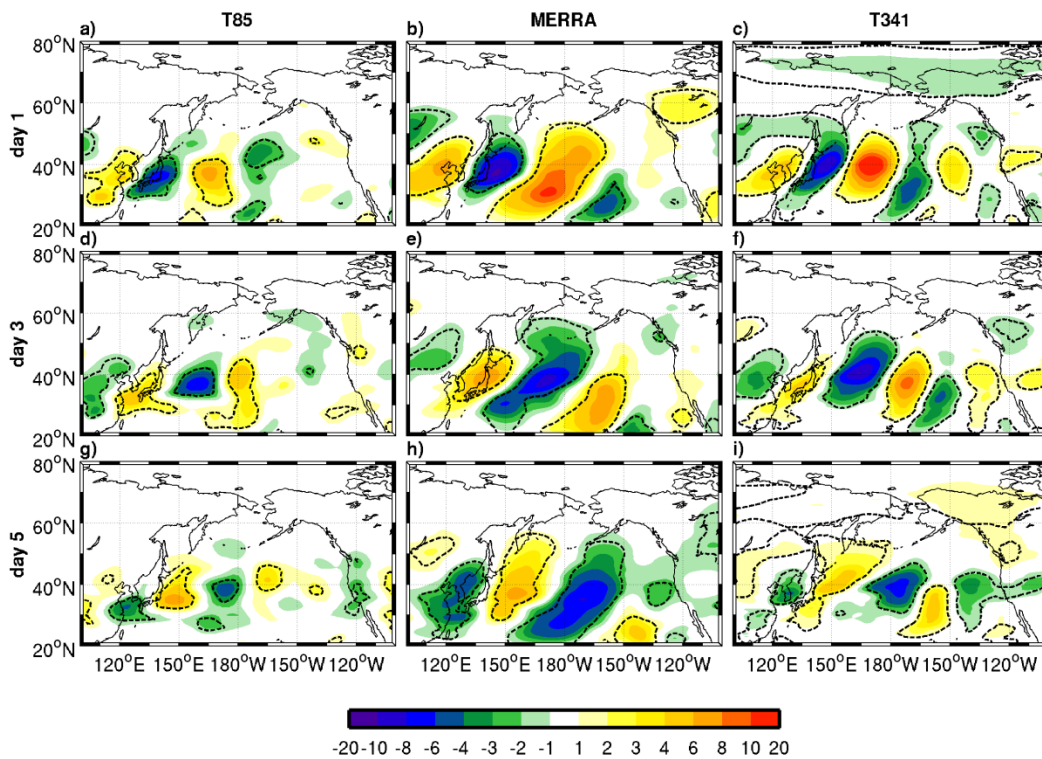
Figure 4.8: Same as Fig. 4.6 but for height tendency forced by the interaction between HF eddies and mean flow (HM).

The height tendency associated with HM term in the high resolution simulation (T341) indicates a similar pattern as observations, but the amplitude is less pronounced (Fig. 4.8c, f); T341 doesn't reproduce the meridional expansion on day 5, though a preceding negative anomaly is found off the west coast of the U.S. (Fig. 4.8i) that is also seen in the

observations. On the other hand, the T85 version underestimates the wave train structure after the event (Fig. 4.8a, d, g), and only produces some scattered and less organized height tendency anomaly over North Pacific, impling a possible inaccurate representative of the eddy mean flow interactionmedium.

The height tendency induced by IF eddies and their interaction with the mean flow (IM) is the most important forcing term for the circulation anomaly over Eastern Pacific where the AR activity is strongly modulated. 1 day after the peak of EACS (Fig. 4.9b), the IM term produces a dipole structure with a large negative height tendency anomaly ($<$ -20 m/day) east of Japan and an adjacent positive height tendency downstream; this indicates an eastward propagation of the trough-ridge pattern in the North Pacific basin. The IM term also contributes to the negative height anomaly north of 55°N, and the amplitude is about 2 m/day. The dipole pattern is still well organized, and it moves eastward gradually on day 3 (Fig. 4.9e), however, the dipole structure in the midlatitudes is more zonally elongated as compared with day 1. The negative height tendency in the high latitudes is further enhanced, and it extends from East Asia to North America, helps the buildup of the coast trough south of Gulf of Alaska. On day 5 (Fig. 4.9h), a negative height tendency center appears across the west coast of North America, and the trough-like anomlay deepened at a rate of about 6~8 m/day on this stage. The dipole structure in the central North Pacific is weakened simultaneously, and it exerts little impact to the circulation in the eastern North Pacific.

97
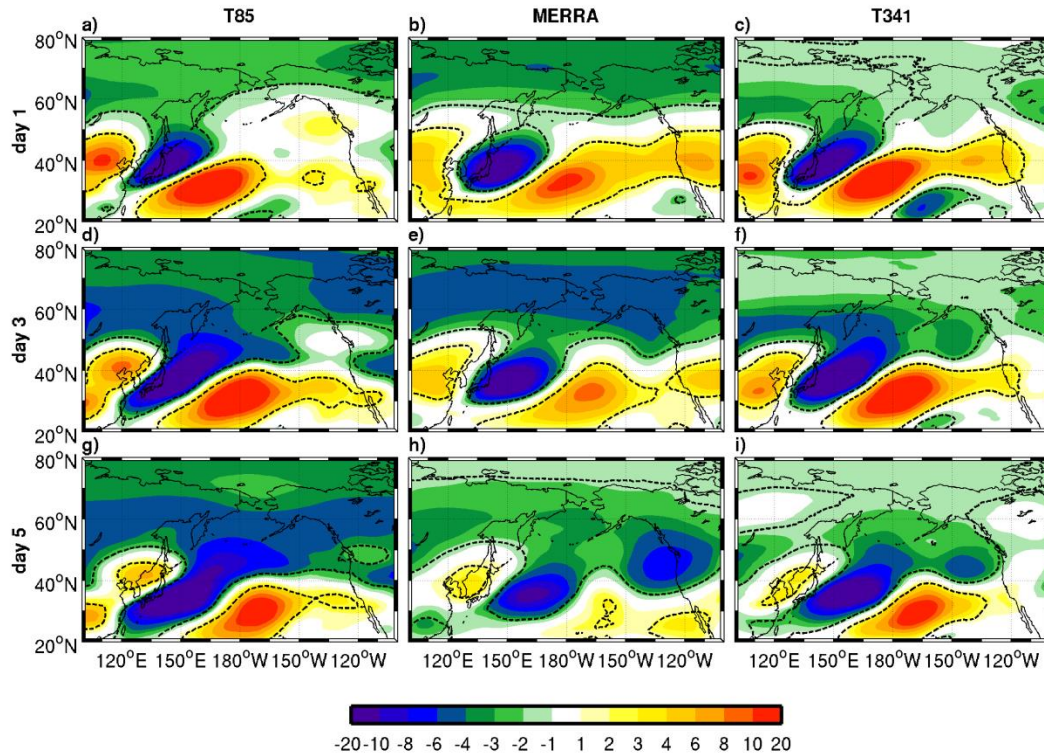
Figure 4.9: Same as Fig. 4.6 but for height tendency forced by the interaction between HF eddies and mean flow (IM).

Both high and medium resolution simulations generally capture the dipole pattern associated with IM term in the midlatitudes on day 1 at east of Japan (Fig. 4.9a, c), however, the negative height tendency in the high latitudes is not quite consistent with respect to amplitude or distribution compare with observes. This negative height tendency moves eastward on day 3 (Fig. 4.9d, f) along with a prominent meridional elongation. At the same time, the extension of negative anomaly over eastern North Pacific is captured by T341 simulation only. The greatest distincton between the simulations and observation is found on day 5, for T85 (Fig. 4.9g), the dipole pattern in the midlatitudes is much more pronounced; although the negative height tendency anomaly is extended to lower latitudes.

The pattern determines the off coast trough and thus the moisture transport corridor over eastern North Pacific-North America, and it is not well defined. For T341 (Fig. 4.9i), the IM term exhibits the trough like height anomaly over eastern Pacific, though its location is slightly westward from the coast. The difference in IM term forcing reveals the weak and delayed moisture transport and resulting precipitation anomaly along the west coast of the U. S. with T341.

In addition to the II, HI, HM and IM terms, the HH term has received attention in a lot of previous studies [*Lau and Holopainen*, 1984]. However, in this study, the HH term (not shown) primarily transports the impact from EACS to the Arctic region and thus suggests little direct causality with the circulation pattern in the midlatitudes especially east of dateline. Moreover, the forcing of planetary vorticity (not shown) is mainly to balance the height tendency produced by the relative vorticity terms with a zonally uniform distribution, and for this reason, it is not presented here either.

4.3.6. The Role of IF Flow

The inverse model to partition the height tendency and the composite analysis described in the preceding sections yield a picture that represents the net effect of the dynamical processes in different timescales. To quantify these processes by demonstrating the relative strength of eddies in different timescales, we make use of a method called "spatial correlation coefficient" [*Jiang and Deng*, 2011]. The coefficient of projection P_n

can be expressed as

$$P_n = \frac{\sum\limits_{\lambda, \varphi} Z_n(\lambda, \varphi) Z'(\lambda, \varphi) \cos \varphi}{\sum\limits_{\lambda, \varphi} Z'^2(\lambda, \varphi) \cos \varphi}$$

(9)

where n denotes the different timescales as defined in section 4.3.2. Z_n represents the composite of geopotential height anomalies for given timescales, and Z' is the composite of height anomalies as shown in Figure 4.5. For a given pressure level, this expression projects the 500 hPa height anomalies in different timescales to the total height anomaly and examines their relative contribution via the day-to-day evolution following the peak of EACS.

Over the western North Pacific sector (20 °N–70 °N, 120 °E–160 °E), as presented in Fig. 4.10c, results from the MERRA data suggest the HF and IF eddies are largely excited immediately after the peak of EACS (day 0). In particular, the IF eddies determine the total circulation anomaly until day 3 while the HF anomaly decays very quick and its influence almost disappears on day 3. This is consistent with the results found in *Compo et al.* [1999]. In the meantime, the relative strength of LF eddies increases quickly and becomes the determinant component since day 4 (greater than 0.3). For the T85 simulation (Fig. 4.10a), IF eddies over western North Pacific modulated by EACS are the most important player throughout the diagnostic period (up to day 12), and explains over 50% of the total height anomaly except for the period from day 4 to day 6. On the other hand, HF and LF eddies barely (< 0.1) contribute to the overall circulation anomaly in this domain compared to the

IF timescale. For T341 (Fig. 4.10e), the evolution of the projection coefficients is consistent with observations, but the HF eddies contribute a very small impact to the total anomaly (less than 0.1). Also, the LF first overwhelms IF on day 5, which is a 2 day delay compared with observation.
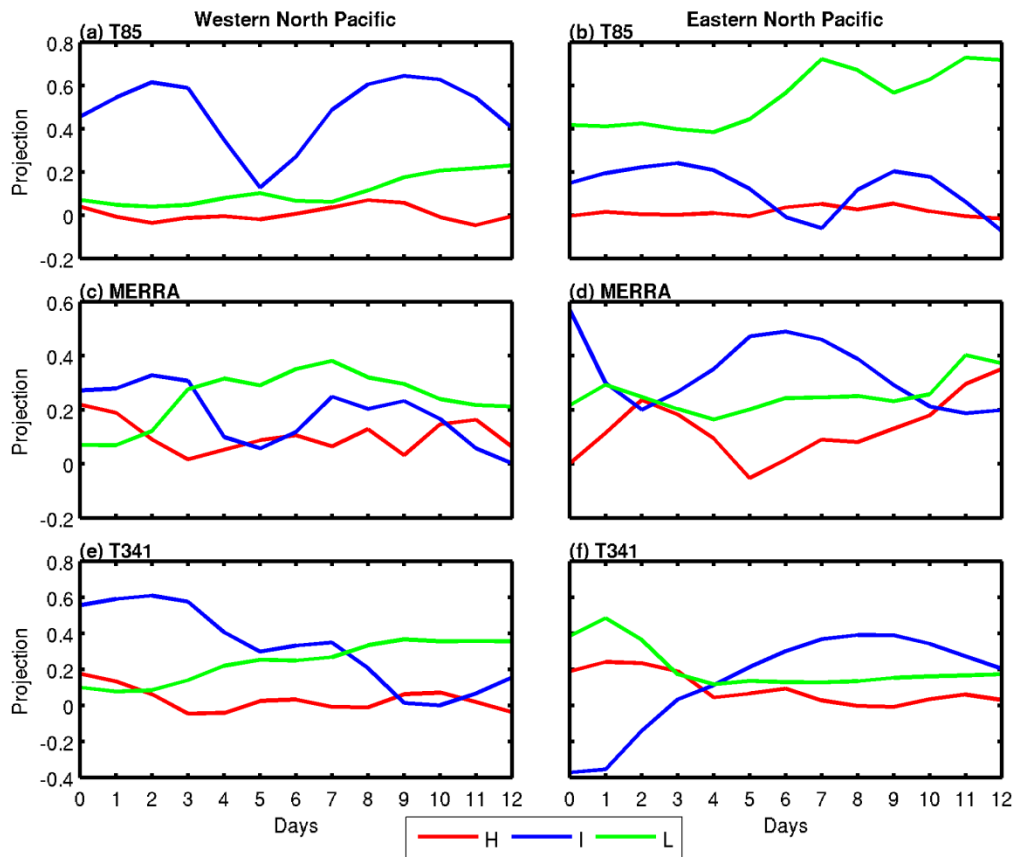
Figure 4.10: Coefficients of projection onto the total disturbance field by disturbances in HF, IF and LF bands. The evolution of the projection coefficients following the peak of the EACS (Day 0) is plotted in (left column) for the western North Pacific and in (right column) for the eastern North Pacific (detailed definition of the regions is provided in 4.3.2). Top row is the result derived from T85 simulation; center row is from MERRA reanalysis; bottom row is from T341 simulation.

Figure 4.10 also displays the spatial projection coefficients over eastern North Pacific

(20 ˚N–70 ˚N, 160 ˚W–120 ˚W) for MERRA data (Fig. 4.10d). At the peak time (day 0) of

the EACS event, the IF timescale anomaly projects most of its circulation pattern to the total height anomaly, while HF eddies do little to influence this stage. 2 days later, the contributions from HF, IF and LF eddies to the total anomaly are comparable, with each of them representing about 20% of the height anomaly in this domain. IF eddies regain their leading position on day 3, lasting up to day 9, with peak amplitude about 0.45 on day 6. During the same period (day 3 to day 9), the LF eddies maintain their influence in this region second to the IF timescale. On the contrary, HF eddies contribute little to the total anomaly on key dates (day 4 to day 6). Following the peak of EACS, the T85 simulation (Fig. 4.10b) plot indicates that the overall circulation pattern is defined by LF eddies, which explain over 40% of the total height anomaly up to day 12; IF eddies are less important in determining the total height anomaly while HF eddies have little directly contribution to the circulation anomaly over eastern North Pacific. The height anomaly projection is better captured by the T341 version (Fig. 4.10f); corresponding to the key period of the circulation anomaly over eastern North Pacific, IF timescale height anomaly largely determines the flow pattern starts from day 5 and up to day 10 in the high resolution simulation; however, the amplitude of projection coefficients for IF eddies are smaller compare with observation.

Result from spatial projection analysis confirm that the IF timescale are the key component to modulate the EACS, and the degree of IF activity largely determines the accuracy of overall circulation pattern especially over eastern North Pacific this is in

contrast to the two simulations. Reported by *Newman et al.* [2012], IF variability is the largest contributor to the moisture transport into southwestern North America during the cool season. IF eddy organizes the water vapor primarily through its advection effect, and AR is a realization of this mechanism [*Jiang and Deng*, 2011; *Newman et al.*, 2012]. On the other hand, as shown in Figure 4.10, the HF variability, which is thought as an essential part of AR development, only plays a very minor role (amplitude less than 0.1) in confining the circulation pattern over western U.S., especially during the active phase of AR following the EACS.

4.4 Section Summary

In this study, the AR activity over the eastern North Pacific near the U.S. west coast and its connection with strong EACS events are evaluated based upon a newly developed AR detection algorithm that quantifies AR occurrence probability. Specifically, it is shown that majority of the precipitation extremes in the U.S. west coast are induced by ARs. The coastal AR activity and precipitation extremes are demonstrated to be significantly modulated by EACS. Following the peak of a strong EACS event, AR occurrence probability initially decreases in the eastern North Pacific, and this decrease is followed by a rapid rise of AR activity 2 days later that persists until 9 days after the cold surge. The elevated AR activity is accompanied by enhanced coastal precipitation during the same period.

Analysis of the North Pacific atmospheric circulation anomalies following the cold surge reveals that the development of a local cyclonic circulation anomaly west of the U.S. coast creates a channel of concentrated moisture transport into the North American continent and this newly-formed AR is directly responsible for the rapid rise of AR activity starting from 2 days after the peak of the cold surge. Local height tendency analysis suggests that the following processes contribute to the development of the local cyclonic circulation anomaly: nonlinear interactions among IF disturbances (II), interactions between HF and IF disturbances (HI), interactions between HF disturbances and the winter mean flow (HM) and between IF and the mean flow (IM). IF disturbances are also found dominate the eastern North Pacific flow anomalies during the period when the AR activity is elevated.

The connection between EACS and AR is further examined in CCSM4 T85 and T341 model output. The higher resolution model (T341) performs much better in terms of capturing the EACS-AR connection. Diagnosis of the model output indicates that the better performance of the T341 model stems primarily from more faithful representations of the IM process and thus the IF disturbances in the T341 model compared to the T85 model. Additionally, a higher model resolution also resolves the filamentary feature of the AR structure more accurately, partly contributing to the better performance of the T341 model. Going with a high resolution global (versus regional) model in climate modeling and projection thus has the following 3 advantages at least when the western U.S.

hydro-climate variability is the main concern: inclusion of spontaneous excitations of remote forcings of hydrological extremes (i.e., EACS), better captured scale-interaction and IF variability, and better resolved concentrated moisture transport (i.e., ARs). Finally, considering that EACS events themselves are also closely tied to IF variability in the extratropics, the importance of an accurate representation of scale-interaction in a model cannot be over-emphasized.

Except Section 4.2, Part of the work presented in this chapter is published on Geophysical Research Letters [Jiang and Deng, 2011] and the other part of the work is submitted to Journal of Climate [Jiang et al. 2013].

CHAPTER 5

CONCLUDING REMARKS

In this dissertation, we have studied the variability of the western U.S. hydrological cycle driven by large-scale circulation anomalies over the North Pacific with a focus on the roles played by the atmospheric high frequency (HF) and intermediate frequency (IF) disturbances (eddies). To serve this purpose, we firstly derived a new set of local eddy kinetic energy (EKE) equations for atmospheric disturbances of different timescales and constructed the 3-D winter climatology of all the energy conversion processes of these equations, including the kinetic energy generation due to the cross-frequency interactions between HF and IF eddies. The main source of HF EKE is baroclinic conversion concentrated in the mid-lower troposphere. Barotropic conversion mainly damps HF EKE and shows positive contributions to IF EKE on the northern flank of the winter-mean tropospheric jet. Interaction between HF and IF eddies acts as a sink for HF EKE and a main source for IF EKE, especially over the eastern (North Pacific and North Atlantic) ocean basins, confirming the substantial role of synoptic-scale transients in the development of IF phenomena such as atmospheric blocking.

On interannual timescales, energy conversion processes of the HF and IF EKE budget exhibit prominent variability, primarily in responses to El Nino-Southern Oscillation (ENSO). The HF EKE response to El Nino is characterized by a dipole (tri-pole) anomaly

over the North Pacific (North Atlantic). Baroclinic conversion is the main driver of the observed changes in HF EKE while barotropic conversion, interaction between HF and IF eddies, and energy flux convergence all play non-negligible roles in determining the final meridional structure of the HF EKE anomalies. Associated with El Nino, IF EKE generally decreases over the North Pacific and increases over the North Atlantic, which mainly result from changes in baroclinic conversion and EKE conversion due to eddy–eddy interactions. The latter is dominated by interaction between IF and LF eddies over the North Pacific, and by interactions between HF and IF eddies, and between IF and LF eddies over the North Atlantic.

HF EKE budget analysis is applied to understand intraseasonal variations of the winter hydroclimate over western North America. During the course of a typical Madden–Julian Oscillation (MJO) event, the HF eddy (storm track) response is characterized by an amplitude-varying dipole propagating northeastward as the center of the anomalous tropical convection moves eastward across the eastern Indian Ocean and the western-central Pacific. The HF EKE budget analysis indicates that the storm track anomaly is induced primarily by changes in the energy flux convergence, baroclinic conversion, and energy generation due to the interaction between HF and LF eddies. The analysis also demonstrates the important roles played by eddy–mean flow interaction and eddy–eddy interaction in the development of the extratropical response to MJO variability.

In the study of extreme droughts over the U.S. Southern Great Plains (SGP), the

winter precipitation deficit over the SGP is clearly linked with significantly suppressed cyclonic activity, i.e., HF disturbances, over the southwestern United States. The suppression of HF disturbances is linked to the low-frequency teleconnection modes over the North Pacific such as the West Pacific (WP) and PNA.

Defined as narrow channels of concentrated moisture transport in the atmosphere, Atmospheric Rivers (ARs) are responsible for over 70% of the extreme precipitation events over the west coast of U.S.. In our study, an automatic AR detection algorithm is developed to identify the AR pattern over North Pacific domain. Based on this algorithm we construct the first climatology of the AR occurrence probability over the western U.S. Our analysis shows that the coastal AR activity and extreme precipitation are significantly modulated by the East Asia Cold Surge (EACS) events: following the peak of event, AR occurrence probability experiences a nearly 100% change relative to its climatology; associated with this, the coastal precipitation over Western U.S. is also enhanced by about 2.5 mm on average in regions of Oregon and North California starting from Day 6 (six days after the peak of the cold surge). Combining the calculation of the spatial projection coefficients with the local height tendency analysis, we find that that the IF eddies play the most important role in establishing the connection between EACS and the anomalous AR activity near western U.S. IF eddies are strongly excited over North Pacific following EACS and largely determined the overall height anomaly, especially over eastern ocean basin; because of the prominent contribution of IF eddy-mean flow interaction in bringing

108

about the off coast trough over Pacific Northwest, the IF eddy itself exhibits positive feedback several days after the peak of EACS. This dynamical feature induced by cold surge over East Asia implies strong inland water vapor transport by means of the advection effect of IF eddies, which alters the AR activity eventually and influences the extreme precipitation over the west coast of the U.S. accordingly.

Downstream development of the large-scale circulation anomalies associated with EACS events is depicted; the barotropical processes lie behind speculate that I-M, I-I, H-I, as well as H-M interactions play important roles in modulating the flow and moisture transport anomalies over North Pacific.

The AR activity and its response to upstream forcing are also evaluated in Community Climate System Model version 4 (CCSM4) simulations with 2 different resolutions. The results indicate that high resolution global model (T341) can better capture those features in three aspects: 1) the filamentary feature of the concentrated water vapor transport can be accurately represented in finer resolution; 2) the scale-interaction, including the eddy-eddy and eddy-mean flow interactions, can be better reproduced; 3) global scale simulation is capable to link spontaneous excitations of hydrological extremes in distant regions..

In conclusion, these studies explore the characteristics of HF and IF eddies, including energy conversion and their interaction, over the northern hemisphere. The works here extend the knowledge of dynamical interaction between tropics and extratropics, and enrich our knowledge of HF and IF eddies over the North Pacific domain. These analyses,

with the goal of serving toward a better understanding of the hydrological cycle over the North Pacific and adjacent downstream continent, illustrate the potential dynamical mechanisms behind the phenomena and extreme events, in both observations and high resolution simulations.

A topic of future work is to utilize the HF and IF EKE budget to study the typical HF and IF phenomena in the midlatitudes (e.g., blocking), and their response and feedback with regard to high latitude phenomena (e.g., Arctic Oscillation). The modulation and phenomena that we identified can be used for assessment in high resolution CCSM4 simulation, and estimate future climate change; meanwhile, the predictability of these phenomena can also be assessed in global and regional models. Another ongoing work is to develop an objective AR-like pattern algorithm based on the image-processing method, and provide an automatic approach to observe the events from both satellite images and forecasting models.

REFERENCES

Bao, J.-W., S. A. Michelson, P. J. Neiman, F. M. Ralph, and J. M. Wilczak (2006), Interpretation of Enhanced Integrated Water Vapor Bands Associated with Extratropical Cyclones: Their Formation and Connection to Tropical Moisture, *Monthly Weather Review*, *134*(4), 1063-1080.

Barnston, A. G., and R. E. Livezey (1987), Classification, Seasonality and Persistence of Low-Frequency Atmospheric Circulation Patterns, *Monthly Weather Review*, *115*(6), 1083-1126.

Berggren, R., B. Bolin, and C. G. Rossby (1949), An Aerological Study of Zonal Motion, its Perturbations and Break-down, *Tellus*, *1*(2), 14-37.

Bjerknes, J. (1966), A possible response of the atmospheric Hadley circulation to equatorial anomalies of ocean temperature, *Tellus*, *18*(4), 820-829.

Bjerknes, J. (1969), ATMOSPHERIC TELECONNECTIONS FROM THE EQUATORIAL PACIFIC1, *Monthly Weather Review*, *97*(3), 163-172.

Bjerknes, J. (1972), Large-Scale Atmospheric Response to the 1964–65 Pacific Equatorial Warming, *Journal of Physical Oceanography*, *2*(3), 212-217.

Black, R. X. (1997), Deducing Anomalous Wave Source Regions during the Life Cycles of Persistent Flow Anomalies, *Journal of the Atmospheric Sciences*, *54*(7), 895-907.

Blackmon, M. L., Y. H. Lee, and J. M. Wallace (1984a), Horizontal Structure of 500 mb Height Fluctuations with Long, Intermediate and Short Time Scales, *Journal of the Atmospheric Sciences*, *41*(6), 961-980.

Blackmon, M. L., J. M. Wallace, N.-C. Lau, and S. L. Mullen (1977), An Observational Study of the Northern Hemisphere Wintertime Circulation, *Journal of the Atmospheric Sciences*, *34*(7), 1040-1053.

Blackmon, M. L., Y. H. Lee, J. M. Wallace, and H.-H. Hsu (1984b), Time Variation of 500 mb Height Fluctuations with Long, Intermediate and Short Time Scales as Deduced

from Lag-Correlation Statistics, *Journal of the Atmospheric Sciences*, *41*(6), 981-991.

Branstator, G. (1987), A Striking Example of the Atmosphere's Leading Traveling Pattern, *Journal of the Atmospheric Sciences*, *44*(16), 2310-2323.

Byna, S., Prabhat, M. F. Wehner, and K. J. Wu (2011), Detecting atmospheric rivers in large climate datasets, in *Proceedings of the 2nd international workshop on Petascal data analytics: challenges and opportunities*, edited, pp. 7-14, ACM, Seattle, Washington, USA.

Cai, M., and M. Mak (1990a), Symbiotic Relation between Planetary and Synoptic-Scale Waves, *Journal of the Atmospheric Sciences*, *47*(24), 2953-2968.

Cai, M., and M. Mak (1990b), On the Basic Dynamics of Regional Cyclogenesis, *Journal of the Atmospheric Sciences*, *47*(12), 1417-1442.

Cai, M., and H. M. Van Den Dool (1994), Dynamical Decomposition of Low-Frequency Tendencies, *Journal of the Atmospheric Sciences*, *51*(14), 2086-2100.

Cai, M., S. Yang, H. M. Van Den Dool, and V. E. Kousky (2007), Dynamical implications of the orientation of atmospheric eddies: a local energetics perspective, *Tellus A*, *59*(1), 127-140.

Cash, B. A., and S. Lee (2000), Dynamical Processes of Block Evolution, *Journal of the Atmospheric Sciences*, *57*(19), 3202-3218.

Chang, C.-P., and K. M. W. Lau (1980), Northeasterly Cold Surges and Near-Equatorial Disturbances over the Winter MONEX Area During December 1974. Part II: Planetary-Scale Aspects, *Monthly Weather Review*, *108*(3), 298-312.

Chang, C.-P., and K. M. Lau (1982), Short-Term Planetary-Scale Interactions over the Tropics and Midlatitudes during Northern Winter. Part I: Contrasts between Active and Inactive Periods, *Monthly Weather Review*, *110*(8), 933-946.

Chang, C. P. (2004), *East Asian monsoon*, viii, 564 p. pp., World Scientific, Hackensack, NJ.

Chang, E. K. M. (1993), Downstream Development of Baroclinic Waves As Inferred from Regression Analysis, *Journal of the Atmospheric Sciences*, *50*(13), 2038-2053.

Chang, E. K. M. (2001), GCM and Observational Diagnoses of the Seasonal and Interannual Variations of the Pacific Storm Track during the Cool Season, *Journal of the Atmospheric Sciences*, *58*(13), 1784-1800.

Chang, E. K. M. (2003), Midwinter Suppression of the Pacific Storm Track Activity as Seen in Aircraft Observations, *Journal of the Atmospheric Sciences*, *60*(11), 1345-1358.

Chang, E. K. M., and I. Orlanski (1993), On the Dynamics of a Storm Track, *Journal of the Atmospheric Sciences*, *50*(7), 999-1015.

Chang, E. K. M., and Y. Fu (2002), Interdecadal Variations in Northern Hemisphere Winter Storm Track Intensity, *Journal of Climate*, *15*(6), 642-658.

Chang, E. K. M., and S. Song (2006), The Seasonal Cycles in the Distribution of Precipitation around Cyclones in the Western North Pacific and Atlantic, *Journal of the Atmospheric Sciences*, *63*(3), 815-839.

Chang, E. K. M., and P. Zurita-Gotor (2007), Simulating the Seasonal Cycle of the Northern Hemisphere Storm Tracks Using Idealized Nonlinear Storm-Track Models, *Journal of the Atmospheric Sciences*, *64*(7), 2309-2331.

Chang, E. K. M., S. Lee, and K. L. Swanson (2002), Storm Track Dynamics, *Journal of Climate*, *15*(16), 2163-2183.

Chen, T.-C., W.-R. Huang, and J.-h. Yoon (2004), Interannual Variation of the East Asian Cold Surge Activity, *Journal of Climate*, *17*(2), 401-413.

Compo, G. P., G. N. Kiladis, and P. J. Webster (1999), The horizontal and vertical structure of east Asian winter monsoon pressure surges, *Quarterly Journal of the Royal Meteorological Society*, *125*(553), 29-54.

Craddock, J. M. (1957), An Analysis of the Slower Temperature Variations at Kew Observatory by Means of Mutually Exclusive Band Pass Filters, *Journal of the Royal Statistical Society. Series A (General)*, *120*(4), 387-397.

Cressman, G. P. (1959), AN OPERATIONAL OBJECTIVE ANALYSIS SYSTEM, *Monthly Weather Review*, *87*(10), 367-374.

Deng, Y., and M. Mak (2005), An Idealized Model Study Relevant to the Dynamics of the

Midwinter Minimum of the Pacific Storm Track, *Journal of the Atmospheric Sciences*, *62*(4), 1209-1225.

Deng, Y., and M. Mak (2006), Nature of the Differences in the Intraseasonal Variability of the Pacific and Atlantic Storm Tracks: A Diagnostic Study, *Journal of the Atmospheric Sciences*, *63*(10), 2602-2615.

Deng, Y., and T. Jiang (2010), Intraseasonal Modulation of the North Pacific Storm Track by Tropical Convection in Boreal Winter, *Journal of Climate*, *24*(4), 1122-1137.

Dettinger, M. D., F. M. Ralph, T. Das, P. J. Neiman, and D. R. Cayan (2011), Atmospheric Rivers, Floods and the Water Resources of California, *Water*, *3*(2), 445-478.

Dirmeyer, P. A., and K. L. Brubaker (2007), Characterization of the Global Hydrologic Cycle from a Back-Trajectory Analysis of Atmospheric Water Vapor, *Journal of Hydrometeorology*, *8*(1), 20-37.

Dole, R. M. (2008), Linking Weather and Climate, *Meteorological Monographs*, *33*(55), 297-348.

Dole, R. M., and N. D. Gordon (1983), Persistent Anomalies of the Extratropical Northern Hemisphere Wintertime Circulation: Geographical Distribution and Regional Persistence Characteristics, *Monthly Weather Review*, *111*(8), 1567-1586.

Dole, R. M., and R. X. Black (1990), Life Cycles of Persistent Anomalies. Part II: The Development of Persistent Negative Height Anomalies over the North Pacific Ocean, *Monthly Weather Review*, *118*(4), 824-846.

Dong, X., et al. (2011), Investigation of the 2006 drought and 2007 flood extremes at the Southern Great Plains through an integrative analysis of observations, *Journal of Geophysical Research: Atmospheres*, *116*(D3), D03204.

Duchon, C. E. (1979), Lanczos Filtering in One and Two Dimensions, *Journal of Applied Meteorology*, *18*(8), 1016-1022.

Egger, J. (1978), Dynamics of Blocking Highs, *Journal of the Atmospheric Sciences*, *35*(10), 1788-1801.

Egger, J., and K. Weickmann (2007), Latitude–Height Structure of the Atmospheric

Angular Momentum Cycle Associated with the Madden–Julian Oscillation, *Monthly Weather Review*, *135*(4), 1564-1575.

Evans, K. J., P. H. Lauritzen, S. K. Mishra, R. B. Neale, M. A. Taylor, and J. J. Tribbia (2013), AMIP Simulation with the CAM4 Spectral Element Dynamical Core, *Journal of Climate*, *26*(3), 689-709.

Evans, K. J., S. Mahajan, J. McClean, J. Caron, M. Maltrud, J. Hack D. Bader, R. Neale, J. Leifeld (2013). A spectral transform dynamical core option within the Community Atmosphere Model, version 4, *Journal of Climate*, *submitted*.

Gent, P. R., et al. (2011), The Community Climate System Model Version 4, *Journal of Climate*, *24*(19), 4973-4991.

Gimeno, L., A. Drumond, R. Nieto, R. M. Trigo, and A. Stohl (2010), On the origin of continental precipitation, *Geophysical Research Letters*, *37*(13), n/a-n/a.

Guan, B., N. P. Molotch, D. E. Waliser, E. J. Fetzer, and P. J. Neiman (2010), Extreme snowfall events linked to atmospheric rivers and surface air temperature via satellite measurements, *Geophys. Res. Lett.*, *37*(20), L20401.

Guan, B., D. E. Waliser, N. P. Molotch, E. J. Fetzer, and P. J. Neiman (2011), Does the Madden-Julian Oscillation Influence Wintertime Atmospheric Rivers and Snowpack in the Sierra Nevada?, *Monthly Weather Review*.

Harnik, N., and E. K. M. Chang (2004), The Effects of Variations in Jet Width on the Growth of Baroclinic Waves: Implications for Midwinter Pacific Storm Track Variability, *Journal of the Atmospheric Sciences*, *61*(1), 23-40.

Hartmann, D. L. (1974), Time Spectral Analysis of Mid-Latitude Disturbances, *Monthly Weather Review*, *102*(5), 348-362.

Hayashi, Y. (1980), Estimation of Nonlinear Energy Transfer Spectra by the Cross-Spectral Method, *Journal of the Atmospheric Sciences*, *37*(2), 299-307.

Held, I. M., S. W. Lyons, and S. Nigam (1989), Transients and the Extratropical Response to El Niño, *Journal of the Atmospheric Sciences*, *46*(1), 163-174.

Higgins, R. W., and K. C. Mo (1997), Persistent North Pacific Circulation Anomalies and

the Tropical Intraseasonal Oscillation, *Journal of Climate*, *10*(2), 223-244.

Higgins, R. W., J. K. E. Schemm, W. Shi, and A. Leetmaa (2000), Extreme Precipitation Events in the Western United States Related to Tropical Forcing, *Journal of Climate*, *13*(4), 793-820.

Hoerling, M. P., and M. Ting (1994), Organization of Extratropical Transients during El Niño, *Journal of Climate*, *7*(5), 745-766.

Holton, J. (2004), An introduction to dynamic meteorology, *International geographics series (88*.

Horel, J. D., and J. M. Wallace (1981), Planetary-Scale Atmospheric Phenomena Associated with the Southern Oscillation, *Monthly Weather Review*, *109*(4), 813-829.

Hoskins, B. J., and K. I. Hodges (2002), New Perspectives on the Northern Hemisphere Winter Storm Tracks, *Journal of the Atmospheric Sciences*, *59*(6), 1041-1061.

Hoskins, B. J., I. N. James, and G. H. White (1983), The Shape, Propagation and Mean-Flow Interaction of Large-Scale Weather Systems, *Journal of the Atmospheric Sciences*, *40*(7), 1595-1612.

Hsu, P.-c., T. Li, and C.-H. Tsou (2010), Interactions between Boreal Summer Intraseasonal Oscillations and Synoptic-Scale Disturbances over the Western North Pacific. Part I: Energetics Diagnosis*, *Journal of Climate*, *24*(3), 927-941.

Jiang, T., and Y. Deng (2011), Downstream modulation of North Pacific atmospheric river activity by East Asian cold surges, *Geophys. Res. Lett.*, *38*(20), L20807.

Jiang, T., Y. Deng, and W. Li (2013), Local kinetic energy budget of high-frequency and intermediate-frequency eddies: winter climatology and interannual variability, *Climate Dynamics*, 1-16.

Jiang, T., K. Evans, Y. Deng, and X. Dong (2013), Intermediate Frequency Atmospheric Disturbances: A Dynamical Bridge Connecting western U.S. Extreme Precipitation with East Asian Cold, *Journal of Climate*, *(Submitted)*.

Jones, C. (2000), Occurrence of Extreme Precipitation Events in California and Relationships with the Madden–Julian Oscillation, *Journal of Climate*, *13*(20),

3576-3587.

Jones, C., D. E. Waliser, K. M. Lau, and W. Stern (2004), Global Occurrences of Extreme Precipitation and the Madden–Julian Oscillation: Observations and Predictability, *Journal of Climate*, *17*(23), 4575-4589.

Jorgenson, M. T., C. H. Racine, J. C. Walters, and T. E. Osterkamp (2001), Permafrost Degradation and Ecological Changes Associated with a Warming Climate in Central Alaska, *Climatic Change*, *48*(4), 551-579.

Kalnay, E., et al. (1996), The NCEP/NCAR 40-Year Reanalysis Project, *Bulletin of the American Meteorological Society*, *77*(3), 437-471.

Kistler, R., et al. (2001), The NCEP–NCAR 50–Year Reanalysis: Monthly Means CD–ROM and Documentation, *Bulletin of the American Meteorological Society*, *82*(2), 247-267.

Knippertz, P., and H. Wernli (2010), A Lagrangian Climatology of Tropical Moisture Exports to the Northern Hemispheric Extratropics, *Journal of Climate*, *23*(4), 987-1003.

Kung, E. C., and P. H. Chan (1981), Energetics Characteristics of the Asian Winter Monsoon in the Source Region, *Monthly Weather Review*, *109*(4), 854-870.

Kushnir, Y. (1987), Retrograding Wintertime Low-Frequency Disturbances over the North Pacific Ocean, *Journal of the Atmospheric Sciences*, *44*(19), 2727-2742.

Kushnir, Y., and J. M. Wallace (1989), Low-Frequency Variability in the Northern Hemisphere Winter: Geographical Distribution, Structure and Time-Scale Dependence, *Journal of the Atmospheric Sciences*, *46*(20), 3122-3143.

Landsberg, H. E., J. M. Mitchell, and H. L. Crutcher (1959), POWER SPECTRUM ANALYSIS OF CLIMATOLOGICAL DATA FOR WOODSTOCK COLLEGE, MARYLAND, *Monthly Weather Review*, *87*(8), 283-298.

Lau, K.-M., and M.-T. Li (1984), The Monsoon of East Asia and its Global Associations—A Survey, *Bulletin of the American Meteorological Society*, *65*(2), 114-125.

Lau, N.-C. (1988), Variability of the Observed Midlatitude Storm Tracks in Relation to

Low-Frequency Changes in the Circulation Pattern, *Journal of the Atmospheric Sciences*, *45*(19), 2718-2743.

Lau, N.-C., and K.-M. Lau (1984), The Structure and Energetics of Midlatitude Disturbances Accompanying Cold-Air Outbreaks over East Asia, *Monthly Weather Review*, *112*(7), 1309-1327.

Lau, N.-C., and E. O. Holopainen (1984), Transient Eddy Forcing of the Time-Mean Flow as Identified by Geopotential Tendencies, *Journal of the Atmospheric Sciences*, *41*(3), 313-328.

Lau, N.-C., and M. J. Nath (1999), Observed and GCM-Simulated Westward-Propagating, Planetary-Scale Fluctuations with Approximately Three-Week Periods, *Monthly Weather Review*, *127*(10), 2324-2345.

Lavers, D. A., G. Villarini, R. P. Allan, E. F. Wood, and A. J. Wade (2012), The detection of atmospheric rivers in atmospheric reanalyses and their links to British winter floods and the large-scale climatic circulation, *Journal of Geophysical Research: Atmospheres*, *117*(D20), D20106.

Lavers, D. A., R. P. Allan, E. F. Wood, G. Villarini, D. J. Brayshaw, and A. J. Wade (2011), Winter floods in Britain are connected to atmospheric rivers, *Geophys. Res. Lett.*, *38*(23), L23803.

Li, F., W. D. Collins, M. F. Wehner, D. L. Williamson, J. G. Olson, and C. Algieri (2011), Impact of horizontal resolution on simulation of precipitation extremes in an aqua-planet version of Community Atmospheric Model (CAM3), *Tellus A*, *63*(5), 884-892.

Liebmann, B., and C. A. Smith (1996), Description of a complete (interpolated) outgoing longwave radiation dataset, *Bull. Amer. Met. Soc.*, *77*, 1275-1277.

Liu, J., B. Wang, H. Lu, and S. Ma (2008), A graph-based image annotation framework, *Pattern Recognition Letters*, *29*(4), 407-415.

Lorenz, E. N. (1955), Available Potential Energy and the Maintenance of the General Circulation, *Tellus*, *7*(2), 157-167.

Madden, R. A., and P. R. Julian (1972), Description of Global-Scale Circulation Cells in the Tropics with a 40–50 Day Period, *Journal of the Atmospheric Sciences*, *29*(6),

1109-1123.

Madden, R. A., and P. R. Julian (1994), Observations of the 40–50-Day Tropical Oscillation—A Review, *Monthly Weather Review*, *122*(5), 814-837.

Mak, M. (1991), Dynamics of an atmospheric blocking as deduced from its local energetics, *Quarterly Journal of the Royal Meteorological Society*, *117*(499), 477-493.

Mak, M., and M. Cai (1989), Local Barotropic Instability, *Journal of the Atmospheric Sciences*, *46*(21), 3289-3311.

Mass, C., and B. Dotson (2010), Major Extratropical Cyclones of the Northwest United States: Historical Review, Climatology, and Synoptic Environment, *Monthly Weather Review*, *138*(7), 2499-2527.

Matthews, A. J., and G. N. Kiladis (1999), The Tropical–Extratropical Interaction between High-Frequency Transients and the Madden–Julian Oscillation, *Monthly Weather Review*, *127*(5), 661-677.

Matthews, A. J., B. J. Hoskins, and M. Masutani (2004), The global response to tropical heating in the Madden–Julian oscillation during the northern winter, *Quarterly Journal of the Royal Meteorological Society*, *130*(601), 1991-2011.

Mo, K. C. (1999), Alternating Wet and Dry Episodes over California and Intraseasonal Oscillations, *Monthly Weather Review*, *127*(12), 2759-2776.

Mo, K. C., and R. E. Livezey (1986), Tropical-Extratropical Geopotential Height Teleconnections during the Northern Hemisphere Winter, *Monthly Weather Review*, *114*(12), 2488-2515.

Mo, K. C., and R. W. Higgins (1998), Tropical Influences on California Precipitation, *Journal of Climate*, *11*(3), 412-430.

Mo, K. C., and R. W. Higgins (1998), Tropical Convection and Precipitation Regimes in the Western United States, *Journal of Climate*, *11*(9), 2404-2423.

Myoung, B., and Y. Deng (2009), Interannual Variability of the Cyclonic Activity along the U.S. Pacific Coast: Influences on the Characteristics of Winter Precipitation in the Western United States, *Journal of Climate*, *22*(21), 5732-5747.

Nakamura, H. (1992), Midwinter Suppression of Baroclinic Wave Activity in the Pacific, *Journal of the Atmospheric Sciences*, *49*(17), 1629-1642.

Nakamura, H., and J. M. Wallace (1990), Observed Changes in Baroclinic Wave Activity during the Life Cycles of Low-Frequency Circulation Anomalies, *Journal of the Atmospheric Sciences*, *47*(9), 1100-1116.

Nakamura, H., and J. M. Wallace (1993), Synoptic Behavior of Baroclinic Eddies during the Blocking Onset, *Monthly Weather Review*, *121*(7), 1892-1903.

Nakamura, H., and T. Sampe (2002), Trapping of synoptic-scale disturbances into the North-Pacific subtropical jet core in midwinter, *Geophysical Research Letters*, *29*(16), 8-1-8-4.

Nakamura, H., M. Nakamura, and J. L. Anderson (1997), The Role of High- and Low-Frequency Dynamics in Blocking Formation, *Monthly Weather Review*, *125*(9), 2074-2093.

Nakamura, H., T. Izumi, and T. Sampe (2002), Interannual and Decadal Modulations Recently Observed in the Pacific Storm Track Activity and East Asian Winter Monsoon, *Journal of Climate*, *15*(14), 1855-1874.

Namias, J., and P. F. Clapp (1949), CONFLUENCE THEORY OF THE HIGH TROPOSPHERIC JET STREAM, *Journal of Meteorology*, *6*(5), 330-336.

Neiman, P. J., F. M. Ralph, G. A. Wick, J. D. Lundquist, and M. D. Dettinger (2008a), Meteorological Characteristics and Overland Precipitation Impacts of Atmospheric Rivers Affecting the West Coast of North America Based on Eight Years of SSM/I Satellite Observations, *Journal of Hydrometeorology*, *9*(1), 22-47.

Neiman, P. J., F. M. Ralph, G. A. Wick, Y.-H. Kuo, T.-K. Wee, Z. Ma, G. H. Taylor, and M. D. Dettinger (2008b), Diagnosis of an Intense Atmospheric River Impacting the Pacific Northwest: Storm Summary and Offshore Vertical Structure Observed with COSMIC Satellite Retrievals, *Monthly Weather Review*, *136*(11), 4398-4420.

Newman, M., G. N. Kiladis, K. M. Weickmann, F. M. Ralph, and P. D. Sardeshmukh (2012), Relative contributions of synoptic and low-frequency eddies to time-mean atmospheric moisture transport, including the role of atmospheric rivers, *Journal of Climate*.

Oort, A. H. (1964), ON ESTIMATES OF THE ATMOSPHERIC ENERGY CYCLE, *Monthly Weather Review*, *92*(11), 483-493.

Orlanski, I., and J. Katzfey (1991), The Life Cycle of a Cyclone Wave in the Southern Hemisphere. Part I: Eddy Energy Budget, *Journal of the Atmospheric Sciences*, *48*(17), 1972-1998.

Pan, L.-L., and T. Li (2008), Interactions between the tropical ISO and midlatitude low-frequency flow, *Climate Dynamics*, *31*(4), 375-388.

Park, T.-W., C.-H. Ho, and S. Yang (2011), Relationship between the Arctic Oscillation and Cold Surges over East Asia, *Journal of Climate*, *24*(1), 68-83.

Penny, S., G. H. Roe, and D. S. Battisti (2010), The Source of the Midwinter Suppression in Storminess over the North Pacific, *Journal of Climate*, *23*(3), 634-648.

Penny, S. M., G. H. Roe, and D. S. Battisti (2011), Reply, *Journal of Climate*, *24*(19), 5192-5194.

Plumb, R. A. (1983), A New Look at the Energy Cycle, *Journal of the Atmospheric Sciences*, *40*(7), 1669-1688.

Pratt, R. W., and J. M. Wallace (1976), Zonal Propagation Characteristics of Large–Scale Fluctuations in the Mid–Latitude Troposphere, *Journal of the Atmospheric Sciences*, *33*(7), 1184-1194.

Ralph, and Dettinger (2011), *Storms, floods, and the science of atmospheric rivers*, 265-266 pp.

Ralph, F. M., and M. D. Dettinger (2011), Historical and National Perspectives on Extreme West Coast Precipitation Associated with Atmospheric Rivers during December 2010, *Bulletin of the American Meteorological Society*, *93*(6), 783-790.

Ralph, F. M., P. J. Neiman, and G. A. Wick (2004), Satellite and CALJET Aircraft Observations of Atmospheric Rivers over the Eastern North Pacific Ocean during the Winter of 1997/98, *Monthly Weather Review*, *132*(7), 1721-1745.

Ralph, F. M., P. J. Neiman, and R. Rotunno (2005), Dropsonde Observations in Low-Level Jets over the Northeastern Pacific Ocean from CALJET-1998 and

PACJET-2001: Mean Vertical-Profile and Atmospheric-River Characteristics, *Monthly Weather Review*, *133*(4), 889-910.

Ralph, F. M., P. J. Neiman, G. N. Kiladis, K. Weickmann, and D. W. Reynolds (2010), A Multiscale Observational Case Study of a Pacific Atmospheric River Exhibiting Tropical–Extratropical Connections and a Mesoscale Frontal Wave, *Monthly Weather Review*, *139*(4), 1169-1189.

Ralph, F. M., P. J. Neiman, G. A. Wick, S. I. Gutman, M. D. Dettinger, D. R. Cayan, and A. B. White (2006), Flooding on California's Russian River: Role of atmospheric rivers, *Geophysical Research Letters*, *33*(13), n/a-n/a.

Raphael, M., and G. Mills (1996), The Role of Mid-Latitude Pacific Cyclones in the Winter Precipitation of California*, *The Professional Geographer*, *48*(3), 251-262.

Raphael, M. N., and I. K. Cheung (1998), North Pacific midlatitude cyclone characteristics and their effect upon winter precipitation during selected El Niño/Southern Oscillation events, *Geophysical Research Letters*, *25*(4), 527-530.

Rayner, N. A., P. Brohan, D. E. Parker, C. K. Folland, J. J. Kennedy, M. Vanicek, T. J. Ansell, and S. F. B. Tett (2006), Improved Analyses of Changes and Uncertainties in Sea Surface Temperature Measured In Situ since the Mid-Nineteenth Century: The HadSST2 Dataset, *Journal of Climate*, *19*(3), 446-469.

Rienecker, M. M., et al. (2011), MERRA: NASA's Modern-Era Retrospective Analysis for Research and Applications, *Journal of Climate*, *24*(14), 3624-3648.

Robinson, D. P., R. X. Black, and B. A. McDaniel (2006), A Siberian precursor to midwinter intraseasonal variability in the North Pacific storm track, *Geophysical Research Letters*, *33*(15), L15811.

Saltsman, B. (1957), EQUATIONS GOVERNING THE ENERGETICS OF THE LARGER SCALES OF ATMOSPHERIC TURBULENCE IN THE DOMAIN OF WAVE NUMBER, *Journal of Meteorology*, *14*(6), 513-523.

Sawyer, J. S. (1970), Observational characteristics of atmospheric fluctuations with a time scale of a month, *Quarterly Journal of the Royal Meteorological Society*, *96*(410), 610-625.

Schubert, S. D. (1986), The Structure, Energetics and Evolution of the Dominant Frequency-Dependent Three-Dimensional Atmospheric Modes, *Journal of the Atmospheric Sciences*, *43*(12), 1210-1237.

Schubert, S. D., M. J. Suarez, P. J. Pegion, R. D. Koster, and J. T. Bacmeister (2004a), Causes of Long-Term Drought in the U.S. Great Plains, *Journal of Climate*, *17*(3), 485-503.

Schubert, S. D., M. J. Suarez, P. J. Pegion, R. D. Koster, and J. T. Bacmeister (2004b), On the Cause of the 1930s Dust Bowl, *Science*, *303*(5665), 1855-1859.

Seager, R., Y. Kushnir, C. Herweijer, N. Naik, and J. Velez (2005), Modeling of Tropical Forcing of Persistent Droughts and Pluvials over Western North America: 1856–2000*, *Journal of Climate*, *18*(19), 4065-4088.

Serreze, M. C., M. P. Clark, R. L. Armstrong, D. A. McGinnis, and R. S. Pulwarty (1999), Characteristics of the western United States snowpack from snowpack telemetry (SNOTEL) data, *Water Resources Research*, *35*(7), 2145-2160.

Sheng, J., and Y. Hayashi (1990a), Observed and Simulated Energy Cycles in the Frequency Domain, *Journal of the Atmospheric Sciences*, *47*(10), 1243-1254.

Sheng, J., and Y. Hayashi (1990b), Estimation of Atmospheric Energetics in the Frequency Domain during the FGGE Year, *Journal of the Atmospheric Sciences*, *47*(10), 1255-1268.

Sheng, J., and J. Derome (1991), An observational study of the energy transfer between the seasonal mean flow and transient eddies, *Tellus A*, *43*(2), 128-144.

Shutts, G. J. (1983), The propagation of eddies in diffluent jetstreams: Eddy vorticity forcing of 'blocking' flow fields, *Quarterly Journal of the Royal Meteorological Society*, *109*(462), 737-761.

Shutts, G. J. (1986), A Case Study of Eddy Forcing During an Atlantic Blocking Episode, *Advances in Geophysics*, *Volume 29*, 135-162.

Stohl, A., and P. James (2005), A Lagrangian Analysis of the Atmospheric Branch of the Global Water Cycle. Part II: Moisture Transports between Earth's Ocean Basins and River Catchments, *Journal of Hydrometeorology*, *6*(6), 961-984.

Straus, D. M., and J. Shukla (1997), Variations of Midlatitude Transient Dynamics Associated with ENSO, *Journal of the Atmospheric Sciences*, *54*(7), 777-790.

Straus, D. M., and J. Shukla (2002), Does ENSO Force the PNA?, *Journal of Climate*, *15*(17), 2340-2358.

Tanaka, H., E. C. Kung, and W. E. Baker (1986), Energetics analysis of the observed and simulated general circulation using three-dimensional normal mode expansions, *Tellus A*, *38A*(5), 412-428.

Trenberth, K. E. (1986), An Assessment of the Impact of Transient Eddies on the Zonal Flow during a Blocking Episode Using Localized Eliassen-Palm Flux Diagnostics, *Journal of the Atmospheric Sciences*, *43*(19), 2070-2087.

Trenberth, K. E., and J. W. Hurrell (1994), Decadal atmosphere-ocean variations in the Pacific, *Climate Dynamics*, *9*(6), 303-319.

Trenberth, K. E., G. W. Branstator, D. Karoly, A. Kumar, N.-C. Lau, and C. Ropelewski (1998), Progress during TOGA in understanding and modeling global teleconnections associated with tropical sea surface temperatures, *J. Geophys. Res.*, *103*(C7), 14291-14324.

Wallace, J. M., and D. S. Gutzler (1981), Teleconnections in the Geopotential Height Field during the Northern Hemisphere Winter, *Monthly Weather Review*, *109*(4), 784-812.

Wallace, J. M., and N. C. Lau (1985), On the Role of Barotropic Energy Conversions in the General Circulation, *Advances in Geophysics*, *Volume 28, Part A*, 33-74.

Wang, B. (2005), *The Asian monsoon*, 1st ed., Springer, New York, NY.

Wehner, M., R. Smith, G. Bala, and P. Duffy (2010), The effect of horizontal resolution on simulation of very extreme US precipitation events in a global atmosphere model, *Clim Dyn*, *34*(2-3), 241-247.

Wehner, M. F., G. Bala, P. Duffy, A. A. Mirin, and R. Romano (2010), Towards Direct Simulation of Future Tropical Cyclone Statistics in a High-Resolution Global Atmospheric Model, *Advances in Meteorology*, *2010*.

Weickmann, K. M. (1983), Intraseasonal Circulation and Outgoing Longwave Radiation Modes During Northern Hemisphere Winter, *Monthly Weather Review*, *111*(9), 1838-1858.

Weickmann, K. M., G. R. Lussky, and J. E. Kutzbach (1985), Intraseasonal (30–60 Day) Fluctuations of Outgoing Longwave Radiation and 250 mb Streamfunction during Northern Winter, *Monthly Weather Review*, *113*(6), 941-961.

Weickmann, K. M., S. J. S. Khalsa, and J. Eischeid (1992), The Atmospheric Angular-Momentum Cycle during the Tropical Madden–Julian Oscillation, *Monthly Weather Review*, *120*(10), 2252-2263.

Weickmann, K. M., G. N. Kiladis, and P. D. Sardeshmukh (1997), The Dynamics of Intraseasonal Atmospheric Angular Momentum Oscillations, *Journal of the Atmospheric Sciences*, *54*(11), 1445-1461.

Welch, B. L. (1947), The Generalization of `Student's' Problem when Several Different Population Variances are Involved, *Biometrika*, *34*(1/2), 28-35.

Wheeler, M. C., and H. H. Hendon (2004), An All-Season Real-Time Multivariate MJO Index: Development of an Index for Monitoring and Prediction, *Monthly Weather Review*, *132*(8), 1917-1932.

Wick, G. A., P. J. Neiman, and F. M. Ralph (2012), Description and Validation of an Automated Objective Technique for Identification and Characterization of the Integrated Water Vapor Signature of Atmospheric Rivers, *Geoscience and Remote Sensing, IEEE Transactions on*, *PP*(99), 1-11.

Wiin-Nielsen, A. (1962), ON TRANSFORMATION OF KINETIC ENERGY BETWEEN THE VERTICAL SHEAR FLOW AND THE VERTICAL MEAN FLOW IN THE ATMOSPHERE, *Monthly Weather Review*, *90*(8), 311-323.

Yang, G.-Y., and B. J. Hoskins (1996), Propagation of Rossby Waves of Nonzero Frequency, *Journal of the Atmospheric Sciences*, *53*(16), 2365-2378.

Zhang, C., and S. M. Hagos (2009), Bi-modal Structure and Variability of Large-Scale Diabatic Heating in the Tropics, *Journal of the Atmospheric Sciences*, *66*(12), 3621-3640.

Zhang, Y., K. R. Sperber, and J. S. Boyle (1997), Climatology and Interannual Variation

of the East Asian Winter Monsoon: Results from the 1979–95 NCEP/NCAR Reanalysis, *Monthly Weather Review*, *125*(10), 2605-2619.

Zhu, Y., and R. E. Newell (1998), A Proposed Algorithm for Moisture Fluxes from Atmospheric Rivers, *Monthly Weather Review*, *126*(3), 725-735.